Astronomy Reports, Vol. 44, No. 12, 2000, pp. 781–789. Translated from Astronomicheskiĭ Zhurnal, Vol. 77, No. 12, 2000, pp. 883–892.

The Probable Role of Cloudy Wind Structure in the X-ray Emission of the Binary HD 193793

O. V. Aleksandrova and K. V. Bychkov

Sternberg Astronomical Institute, Universitetskiĭ pr. 13, Moscow, 119899 Russia

Received November 18, 1999

Abstract—A model with interacting two-phase winds, each consisting of rarified gas and dense, compact clouds, is proposed to explain the weakness of the variability of the X-ray emission of the binary system HD 193793. The flowing together of the rarified components, collisions of clouds, and the motion of the clouds in the rarified component of the other wind are considered. Computations of the interactions of the rarified components were carried out using the method of Chernyĭ for standard, two-dimensional, gas–dynamical problems, taking into account differences in the ion and electron temperatures. Due to the adiabatic expansion of the rarified gas behind the shock front, the X-ray luminosity decreases at $1/r$, where r is the distance between the stars in the system. The gas in the dense clouds radiates, leading, on the contrary, to a gradual growth in their luminosity in the transition from periastron to apoastron, approximately proportional to $r^{1/3}$. The joint action of these two factors could give rise to the observed nearly constant luminosity of the system at 2–5 and 2–6 keV. The contribution of the clouds exceeds that of the rarified component by a substantial factor. © *2000 MAIK "Nauka/Interperiodica".*

1. INTRODUCTION

In this work, we develop more fully a model for a two-phase stellar wind in connection with X-ray observations of the wide binary system HD 193793 [1–3]. We will use the term "two-phase" or "two-component" for gas flow consisting of dense, compact clouds embedded in a rarified medium. Theoretical studies have usually concentrated on the rarified wind component.

In 1967, to explain the excess emission observed in the HeII lines of the star V444 Cyg, Cherepashchuk [4] proposed the existence of additional UV radiation in close binary systems due to dissipation in a supersonic stream of gas from the Wolf–Rayet (WR) component flowing around the O-star component. The concept of interaction between stellar wind and a surrounding medium was introduced in 1968 by Pikel'ner [5], based on his measurements of the Doppler velocities of nebulosities around hot stars made with Shcheglov [6]. Prilutskiĭ and Usov [7] showed that a WR+O binary could be a source of appreciable X-ray emission. Further, the theory of uniform flows was investigated taking into account many physical processes, such as the gradual acceleration of the wind, radiation pressure [8], the electron thermal conductivity [9], radiation in the continuum and in lines of resonance transitions of the most abundant elements [10, 11], absorption of X-rays by cool gas in the wind [12, 13], and flow instabilities [14]. Computations were performed using both two-dimensional numerical methods [15, 16] and analytical methods in the framework of the approximation of Chernyĭ [17] for steady-state, two-dimensional problems [18, 19].

Currently, the theory of stellar winds with a rarified phase has been developed rather fully, and is, on the whole, in agreement with observations. However, there remain difficulties, some of which have provided the basis for inferring the presence of clouds in the wind. For example, the X-ray luminosities yielded by theoretical computations are too high. In nine binary systems studied by Cherepashchuk [20], the theoretical X-ray luminosities substantially exceeded those observed by *Einstein*.

In 1979, Bychkov [21] proposed a model with a two-phase wind from a pre-supernova with the parameters of a Wolf–Rayet star to explain the thin-filament structure of supernova remnants. In 1990, Cherepashchuk [22] applied this idea to try to decrease the difference between the theoretical and observed X-ray luminosities indicated above. Other evidence supporting the presence of clouds follows from a comparison of the mass-loss rate of the component WN5 of the binary V444 Cyg determined in two independent ways: radio observations yield a value an order of magnitude larger than optical estimates [23]. Cloudy structure in the wind of the WR star could also explain the rapid spectral and photometric variability of the system [24, 25].

In one close binary—SS 433—the presence of clouds is detected in the peaks of the hydrogen emission lines [26]. These exit the region surrounding the relativistic object—neutron star or black hole—and further interact with the accretion disk; they could be responsible for some of the X-ray and radio emission of the system. The interaction of clouds with a rarified medium is manifested most clearly in SS 433, and interpretation of the corresponding observations could serve as a reference point for applying this type of model to other binaries.

1063-7729/00/4412-0781$20.00 © 2000 MAIK "Nauka/Interperiodica"

From the point of view of clouds, the wide binary system HD 193793 is of special interest. Its orbital period is about eight years, and the orbital semi-major axis exceeds 14 AU [1]. Due to the large distance between the components, the gas densities for both winds in their collision region is so small that both absorption and radiative cooling are appreciably weakened. In addition, it is clear that we can take the gas flow in the collision region to be steady-state. (In close binaries, the wind acceleration, which is difficult to take into account, plays an important role.) These circumstances make it possible to substantially specialize computations and carry out a detailed comparison between the theoretical results and observations of the X-ray light curve. We will see that these observations can be explained using a two-phase wind model.

Section 2 discusses the model as a whole. In Section 3, we present computed spectra for the X-ray emission arising due to the collision of the rarified wind components, and take the presence of clouds into account in Section 4. Section 5 considers observational and theoretical aspects of the X-ray light curve of the system.

2. INTERACTION OF TWO-PHASE WINDS

Let us describe a general picture of our interacting two-phase wind model. In Fig. 1, the Wolf–Rayet star is located to the left and the OB star to the right. Since the winds from Wolf–Rayet (WR) stars are typically one and a half or two orders of magnitude stronger than winds from OB stars, the interface boundary C bulges toward the WR star. In addition, due to the difference in the wind powers, any point O is roughly a factor of 5–10 closer to the OB star. This shift away from the WR star is not shown in the figure due to space limitations. In fact, all three curves—S_{WR}, C, and S_{OB}—should be somewhat closer to the right-hand star. The unperturbed wind gas is heated when it passes through the S_{WR} or S_{OB} shock fronts. The X-ray emission originates in regions I and II, which contain the heated gas. Sometimes, the wind from the OB star becomes strongly compressed against the opposing wind. In this case, the hot region II may be absent, and the X-ray emission may be determined by the wind from the Wolf–Rayet star.

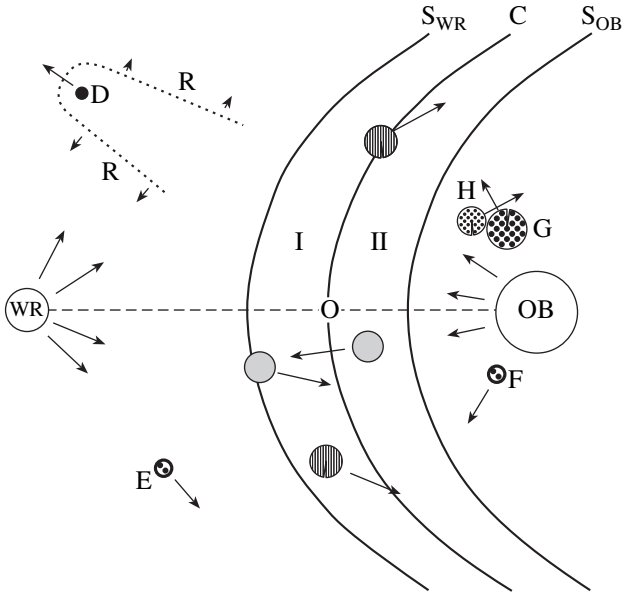

Fig. 1. Interaction of two-phase stellar winds.

The schematic picture in Fig. 1 is idealized in the sense that it does not take into account instabilities of the flow of plasma along the interface boundary. Several types of perturbations can arise here: instability of the tangential discontinuity [27], for example, as well as Rayleigh–Taylor instability and exchange instability, in the case of radiative cooling [28]. Using detailed two-dimensional computations, Myasnikov *et al.* [14] have described the development of initially small perturbations that lead to an appreciable distortion of the interface boundary. This is very important in the theory of colliding rarified winds without a cloudy component. However, for the problem under consideration here, such initially small perturbations are much less important. The reason is that the interaction of the clouds of one wind with the rarified phase of the other wind lead to perturbations that can in no way be considered small.

Let us assume that each cloud moves with speed V, equal to the local speed of expansion of the rarified phase of the wind. The direction of motion for each cloud is indicated by an arrow. When clouds ejected from the OB star are to the right of the front S_{OB} and clouds ejected from the Wolf–Rayet star are to the left of S_{WR}, they influence their own rarified component only weakly. This is true of cloud E in the wind from the Wolf–Rayet star, and also of clouds F and G ejected by the OB star. The rapid rising of clouds in various directions is hindered by the pressure of the surrounding rarified gas. The size of a cloud can increase as the external pressure decreases, but this will occur only in the absence of dissipative processes within the cloud. If such processes, such as radiative cooling, take place, a decrease in the external pressure may not always be accompanied by expansion of the cloud.

A fundamental difference in the behavior of clouds and of the rarified component becomes apparent when they intersect boundary C. A dense cloud passes through the boundary virtually unimpeded and moves into the region occupied by the rarified wind from the other star. The cloud decelerates, gradually gathering up the rarified gas ahead of its path. Like a supersonic airplane, it generates a strong shock in the oncoming flow. In Fig. 1, this situation is shown by cloud D. The dotted curve around this cloud denotes shock wave R in the rarified gas of the Wolf–Rayet wind. In the same way, cloud H perturbs the rarified gas from the OB star; however, we have not drawn the associated shock wave in order to avoid making the diagram cluttered. The

unmarked clouds perturb the gas in regions I and II, imparting the flow with a partially chaotic character. Clouds G and H collide, and shocks propagate inside each of them, which we will also include in our analysis.

As we can see even from this general and quite crude schematic, a two-phase wind should appreciably complicate the flow pattern and give birth to numerous and varied shocks. Let us now consider qualitatively the flight of a single cloud and the collision of a single pair of clouds.

Figure 2 depicts the interaction of a dense, compact cloud with rarified gas. The cloud moves from right to left in the direction of the long, horizontal arrow. The speed of the cloud (2000–3000 km/s) is much higher than the sound speed of the unperturbed wind gas (10–20 km/s). Therefore, its Mach angle will be very small, and, to first approximation, we can assume that shock wave R in the rarified gas is nearly cylindrical in shape. The gas heated at the front R expands perpendicular to the cloud motion.

To first approximation, the evolution of the channels of hot gas can be described using a self-similar flow model of the sort usually applied to supernova remnants [29]. Namely, three stages in the expansion are considered in succession: first free expansion, followed by adiabatic and radiative deceleration. The difference of the problem at hand from the supernova-remnant case lies in the higher gas density involved and the presence of cylindrical rather than spherical symmetry. The evolution of hot cylinders of gas has been discussed for the case of the interstellar medium in [21]. In the adiabatic stage, the expansion of the cylinder is accompanied by a decrease in the density inside it. When the stage of radiative cooling is initiated, the cavity is surrounded by a dense envelope of cool gas.

A schematic plot of the density distribution for the two cases indicated above is presented in Fig. 3. The left plot corresponds to radiative cooling and the right to adiabatic expansion; in both cases, the direction of the cylinder axis is from right to left (denoted by an arrow). During the adiabatic expansion, the density behind the shock front R falls off monotonically. After the onset of radiative cooling, the isobarically radiating gas forms a region of enhanced density around the hot, rarified plasma. Thus, in the rarified phase, each wind can form numerous cavities with complex density distributions.

The head of hot, rarified gas behind R generates a shock wave in the cloud. The part of the cloud that is perturbed by the shock is shaded in Fig. 2. Arrows show the motion of the front into the cloud. The speed of the front relative to the cloud is appreciably lower than both the speed of the cloud itself and the speed of the expansion of the cylinder. Due to the cloud's high density, the shock rapidly radiatively cools, emitting radiation at ultraviolet and X-ray wavelengths.

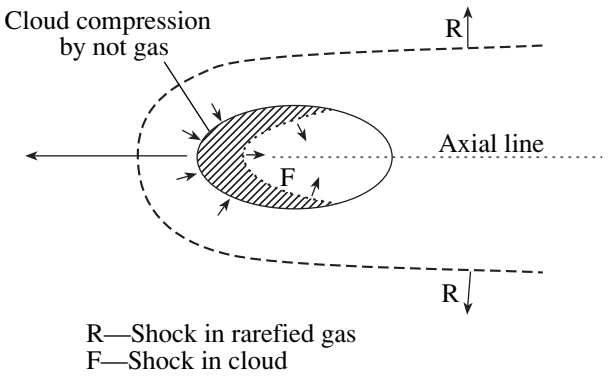

Fig. 2. Motion of a cloud in a rarified medium.

Let us turn to the last element in our picture: the collisions of clouds. During a collision, a shock wave propagates in each cloud. These are denoted F_1 and F_2 in Fig. 4, with the shocks denoted by dotted curves and the perturbed gas shaded. The collisional speed, or the relative speed of the clouds, depends on the spatial location where the clouds collide. Near a frontal point, the collisional speed will be the sum of the cloud speeds. If one cloud strikes another from behind, their speeds subtract. For a specified relative speed, the speed of the shock front inside each cloud depends on the ratio of the cloud densities, i.e., on the density contrast: the front in the less dense cloud moves faster.

Often, the densities of both clouds are so high that the gas in them is able to radiatively cool. In this case, the flow pattern is nearly steady-state, since the cooling time is less than all other time scales in the problem. However, other cases are also possible. For example, if the density contrast is too great, the less dense cloud may not be able to radiatively cool, and it will expand adiabatically. In this case, a radiative shock propagates only in the denser cloud. Note that, at high densities, the radiation will be weak due to the low speed of the shock.

Thus, even in this one element of the picture—collisions between clouds—there is a rather wide range of possibilities. On the whole, the presence of clouds makes the gas flow appreciably more varied than the case when only a single rarified gas component is taken into account.

3. THE X-RAY LIGHT CURVE OF THE RARIFIED COMPONENT

The X-ray emission brought about by the interaction of the rarified phases of the stellar winds has been calculated in many studies, as indicated in the Introduction. Our goal is to take into account the particular properties of the wide binary HD 193793. These are primarily associated with the large distance between the two components and, as a result, the relatively low density of the gas in the system. Therefore, we can

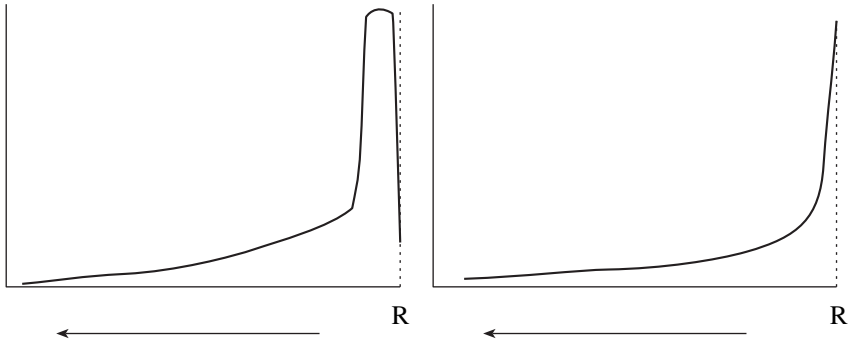

Fig. 3. Density distribution inside an expanding cylinder.

neglect radiative cooling by the rarified gas. Simultaneously, we must take into account the non-uniformity of the wind temperature; i.e., the difference in the ion and electron temperatures of the plasma behind the shock front.

Our computations were performed using the method of Chernyĭ [17], which is valid for steady-state, two-dimensional problems. We mainly followed the work of Usov [18], allowing in addition for possible temperature non-uniformity of the plasma. We used Eqs. (21)–(24) from [18], omitting in the energy Eq. (24) the Q_f term describing radiative cooling. We allowed for temperature non-uniformity as follows. In our two-temperature approximation, the pressure p is expressed in terms of the so-called "total" temperature Σ and the number density n of the ions:

$$p = nk\Sigma. \quad (1)$$

Here, k is the Boltzmann constant and the total temperature can be written in terms of the ion and electron temperatures T_i and T_e

$$\Sigma = T_i + z_e T_e. \quad (2)$$

In the case of a single-temperature plasma, $T_i = T_e$. The number of electrons per ion is determined by the chemical composition of the plasma. In the problem at hand, we can take the main electron donors to be fully ionized hydrogen and helium. Of course, the wind from the WR component can contain appreciable amounts of carbon. However, in the absence of radiative cooling, this has virtually no influence on the final results.

If we denote Y_{He} to be the relative number density of helium (the relative number density of hydrogen is $1 - Y_{\mathrm{He}}$), then

$$z_e = 1 + Y_{\mathrm{He}}.$$

In the absence of radiative cooling, the ion and electron temperatures enter only in the combination Σ, making it possible to solve the problem in two steps. We first compute the density, pressure, velocity vector, and total temperature as functions of position; further, we find T_i and T_e by solving for the energy exchange between the ions and electrons given the already determined values for the other quantities.

A differential equation for the electron entropy S_e flows from the first law of thermodynamics:

$$T_e \frac{dS_e}{dt} = A\frac{n}{T_e^{3/2}}\left(\frac{\Sigma}{1+z_e} - T_e\right). \quad (3)$$

The rate of energy exchange is taken from formula (5.31) of [30] with the coefficient A equal to

$$A = \frac{8\sqrt{2\pi}}{3}\frac{e^4 L\sqrt{m_e}}{m_p k^{3/2}}(1+z_e),$$

where e is the elementary charge, L the Coulomb logarithm, and m_e and m_p the masses of the electron and proton. We used the following expression for S_e:

$$S_e = \ln(T_e/n^{2/3}). \quad (4)$$

This differs from $\ln(p_e/\rho^{5/3})$ only by a constant, which drops out during differentiation of the left-hand side of (3). In precisely the same way, with accuracy to within a constant, the total entropy of the gas is equal to

$$S = \ln\left(\frac{\Sigma}{(1+z_e)n^{2/3}}\right).$$

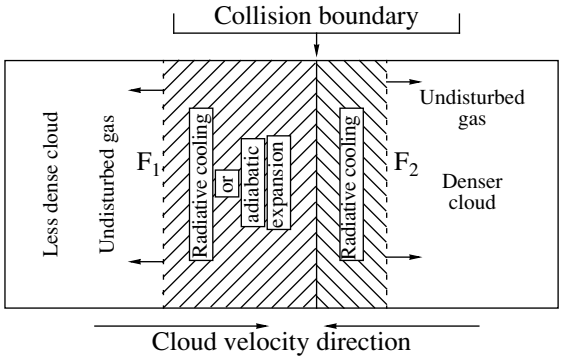

Fig. 4. A collision of clouds.

We introduce the desired function

$$\psi = T_e/n^{3/2}. \quad (5)$$

Using (4), Eq. (3) can be rewritten

$$\frac{d\psi}{dt} = A\frac{e^S - \psi}{\psi^{3/2}}. \quad (6)$$

In the absence of radiative cooling, S is constant along stream lines, along with the total entropy of the gas. Therefore, for each stream line, we can obtain the solution of (3) in quadrature. The corresponding indeterminate integral is taken over elementary functions, which enables us to algebraically express t in terms of ψ. Here, t is a Lagrangian coordinate measured along the stream line and equal to the time that has passed since the intersection of the shock front by a particle of the fluid. Using the known values of ψ and n, we use (5) to calculate T_e. In this way, we obtain a solution in a two-temperature approximation. Further, we follow [18], with the refinement that we compute the spectrum using a Newtonian approximation with a Buzeman correction, whose contribution is 30–40%.

We computed the X-ray luminosity for various phases in the period of HD 193793, adopting the following parameters for the system [1] and its components:

period	P = 2893 days	
eccentricity	$\varepsilon = 0.84$	
semi-major axis	a = 14.7 AU	
spectral types	O4–5V	WC7
luminosities $\log(L/L_\odot)$	5.65	5.2
masses M, $M_\odot$	38	13
wind speeds V_∞, km/s	3200	2860
mass loss rates M, $M_\odot$/year	1.8×10^{-6}	5.7×10^{-5}

Figure 5 presents the theoretical light curve for 2–6 keV, which corresponds to the hard part of the spectra in observations with the GINGA and ASCA satellites [2, 3]. The vertical axis plots the logarithm of the luminosity L_X, and the horizontal axis plots the time since periastron in years. The strong dependence of the theoretical luminosity on phase is clearly visible, and corresponds, to first approximation, to the law $L_X \propto 1/r$. This is quite understandable from a physical point of view, with a large role played by a geometrical factor—the elongation of the orbit. In the absence of radiative cooling, the X-ray emission is determined by the volume emission measure ME = $n^2\nu$, where ν is the volume of the radiating gas. When the distance r between the components is increased, the wind density falls off as r^{-2}, while the volume of the radiating region increases as r^3, so that ME $\propto 1/r$. The distances between the components at periastron and apoastron differ by a factor of $\frac{1+\varepsilon}{1-\varepsilon} \approx 10$, which largely determines the theoretical dependence of the X-ray luminosity on orbital phase.

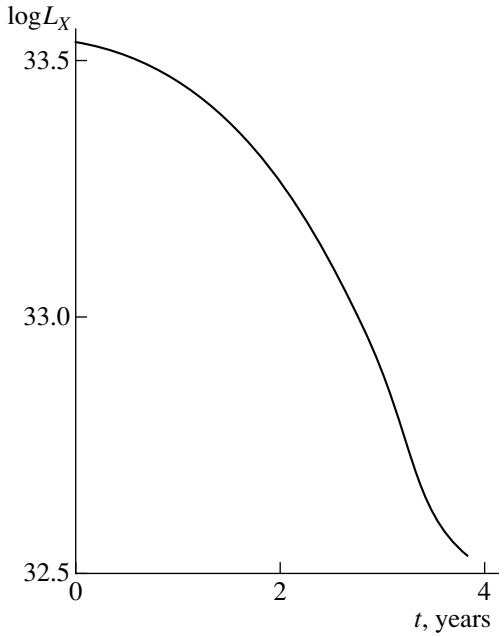

Fig. 5. Theoretical light curve for HD 193793 in the 2–6 keV band.

In addition to this geometrical factor, the physical aspects of the interaction also contribute, first and foremost the temperature non-uniformity of the gas. Our computations show that energy exchange plays an important role in the WR-star wind, additionally decreasing the bremsstrahlung at apoastron, where the electron temperature is lower due to the lower energy-exchange rate. The final rate of energy exchange between the ions and electrons also shifts the phase of the theoretical X-ray light curve, as can clearly be seen in Fig. 5. At large speeds, the contribution of another physical factor can also become important—the electron heat capacity. The corresponding computations taking into account the temperature non-uniformity and radiative cooling [32] showed that the influence of this factor on the continuous spectrum becomes appreciable only if the speed of the front relative to the unperturbed gas exceeds 5000 km/s. For the gas speeds under consideration here, of the order of 3000 km/s, the effect of the electron heat capacity can be neglected.

Let us compare our results with observations by the EXOSAT, GINGA, and ASCA satellites. Koyama *et al.* [3] reported that the dependence of the X-ray emission of HD 193793 on orbital phase was very weak. In the 2–6 keV band, there was a good agreement between the fluxes measured by GINGA at epoch 1987.59 (2.3 years after periastron) and by ASCA at epoch 1993.44 (three months after periastron). On the contrary, the theoretical dependence varies strongly with phase. As we can

see from Fig. 5, two years after periastron, the observed flux should decrease by approximately a factor of three. This discrepancy between the observations and theory is confirmed by three EXOSAT observations of HD 193793 in 1984–1985: variations of the 2–5-keV luminosity did not exceed 20% [1]. Koyama *et al.* [3] conclude that there is no convincing evidence that the observed flux above 2 keV appreciably changes as the distance between the two stars in the binary system increases or decreases.

Thus, a model with collisions of only rarified stellar-wind components cannot explain the weakness of the variability of the X-ray emission of HD 193793 [2, 3]. In our opinion, this suggests that a large role is played by a cloudy wind component. In contrast to the rarified gas, dense, compact clouds can radiate away a substantial part of their kinetic energy during collisions, leading to a different time dependence for the theoretical luminosity. We will now turn to an analysis of the dynamics and radiative cooling of colliding clouds.

4. CLOUD COLLISIONS

In contrast to the rarified component, clouds do not from a well-defined interface boundary. Each dense cloud moves essentially freely through the circumstellar gas of the binary system, experiencing only gradual deceleration in the rarified gas of the wind of the other star. Therefore, clouds can interact virtually over the entire volume of the system. During rare cloud collisions, shock waves will be initiated in each cloud. The speed of the shock u relative to the unperturbed gas depends on the density of the cloud ρ. The conservation of momentum flux at the front yields the well known relation, valid for a strong radiative shock:

$$u_1/u_2 \approx \sqrt{\rho_2/\rho_1}. \quad (7)$$

If the cloud densities are equal, u is approximately equal to the speed of the cloud relative to the center of mass. When there is a large difference in the two cloud densities, another picture develops. A strong shock propagates in the less dense cloud with a speed that is close to the algebraic sum of the two cloud speeds $V_1 + V_2$, while the shock speed in the denser cloud is appreciably lower.

Let us consider cloud parameters for which suppression of the observed X-ray emission is possible. We must first elucidate under what conditions the gas will radiatively cool. For this, we compare the dynamical time scale

$$t_D = d/u \quad (8)$$

with the radiative-cooling time in the front

$$t_c = kT_{sh}/4n\varphi. \quad (9)$$

Here, k is the Bolztmann constant,

$$kT_{sh} = \frac{3}{16} m_{aem} \mu u^2$$

the temperature in the front, determined by a Hugoniot adiabat; n the number density of particles in the unperturbed part of the cloud; and φ the radiative-cooling function. The factor of four takes into account the compression of gas in the front. Under these conditions, the main mechanism for radiative cooling is bremsstrahlung [31]:

$$\varphi \approx 1.43 \times 10^{-27} \langle g \rangle \sqrt{T} \sigma. \quad (10)$$

In accordance with [31], we take the Gaunt factor $\langle g \rangle$ to be 1.2. The quantity σ is obtained by summing over the most abundant elements:

$$\sigma = \sum_i Z_i^2 Y_i, \quad (11)$$

where Z_i is the nuclear charge and Y_i is the relative abundance of an element in terms of particle number; we adopt $\sum_i Y_i = 1$. We assume that all elements taken into account are fully ionized. In the case of the OB star, it is sufficient to include only hydrogen and helium, so that σ_{OB} becomes numerically equal to the molecular weight of the gas μ without taking into account electrons:

$$\sigma_{OB} = \mu \approx 1.3.$$

To estimate σ_{OB}, we took the helium content to be $Y_{He} = 0.1$. The Wolf–Rayet wind has a different composition, with little hydrogen, a high helium content, and an appreciable amount of carbon Y_C. We adopt $Y_{He} = 0.9$ and $Y_C = 0.05$ [1]. Given the low hydrogen content, its precise value influences the final result little, and we set $Y_H = Y_C$. In this case, $\sigma_{WR} = 5.45$.

For the same density ρ, the number of particles n is inversely proportional to the molecular weight. Therefore, the influence of chemical composition on φ is determined by the ratio σ/μ. This is equal to unity for the O star and is approximately 1.3 for the WR star. Thus, the efficiency of bremsstrahlung cooling is approximately 30% higher in the WR-star clouds.

The condition for radiative cooling of a cloud

$$t_D \geq t_c \quad (12)$$

taking into account the Hugoniot adiabat

$$kT_{sh} = \frac{3}{16} m_{aem} \mu u^2$$

leads to the inequality

$$\Omega_{22} > \frac{7}{\sqrt{\mu}} w_{3000}^2 \quad (13)$$

for the surface number density of particles in a cloud in units of 10^{22} cm^2. The quantity w_{3000} on the right is equal to $u/3000$ km/s. Our further computations assume that this radiative-cooling condition is satisfied unless stated otherwise.

Let us determine the cloud parameters that could give rise to the observed X-ray emission. We denote the size of a cloud d. Obviously, there is a whole range of possible values of d. We will be interested in clouds with sizes of the order of 10^{10} cm, and will introduce the dimensionless parameter $d_{10} = d/10^{10}$ cm. When $d_{10} = 1$, the particle number density for the radiating cloud, in accordance with (13), should not be less than 7×10^{12} cm^{-3}. We can derive a rough estimate of the number of interacting clouds in the binary system as follows. Imagine a sphere of radius R surrounding one of the stars. The mass of clouds inside this sphere will be

$$M(R) = \frac{\dot{M}}{V}R. \quad (14)$$

Using (13), we estimate the mass of a single cloud such that the radiative-cooling condition is satisfied to be

$$m_1 = \frac{\pi}{6}\mu m_{aem}\Omega d^2 \geq 6.08 \times 10^{18}\sqrt{\mu}w_{3000}^2 d_{10}^2 \text{ g}.$$

It follows that an upper limit to the number of clouds inside the sphere of radius R is

$$N(R) \leq \frac{M(R)}{m_1} = 3.67 \times 10^7 \frac{\dot{M}_5 R_{14}}{d_{10}^2\sqrt{\mu}w_{3000}^2}. \quad (15)$$

Here, $\dot{M}_5$ denotes the mass-loss rate in units of $10^{-5}\,M_\odot$/year and $R_{14} = R/10^{14}$ cm. Let us estimate the probability p for the collision of the cloud with a cloud from the other star. We will assume that the ratio of the total cross-section of all clouds $\frac{\pi}{4}Nd^2$ to the cross-section of the sphere πR^2 is small. In this case, we can neglect overlap of the clouds, from which it follows that

$$p \approx Nd^2/4R^2. \quad (16)$$

Substituting (15) in this expression, we obtain an upper limit for the desired probability

$$p \approx 9.2 \times 10^{-2}\frac{\dot{M}_5}{\sqrt{\mu}R_{14}w_{3000}^3}. \quad (17)$$

Numerical values of p are presented below for each wind at two points in the orbit: the probabilities through the WR wind are 7.8 and 88% and through the OB wind are 0.3 and 3.4%, respectively, for apoastron and periastron. Of course, the large value of p for motion through the WR wind at periastron does not reflect the true probability, since an appreciable role is played by overlap of clouds along the line of sight. This value could come about in approximately half of cases, so that we expect the true probability for a cloud collision to be of the order of 40%.

Let us estimate the rate of cloud collisions inside a sphere of radius R, where R is, in this case, equal to the distance between the stars. The mean free path l is determined by the number density of clouds for the other star's wind and their cross-section. As a first approximation, we can take

$$l = \frac{2}{3}\frac{R^3}{N(R)d^2}, \quad (18)$$

if we take the cloud to be a sphere with diameter d. The cloud collision rate is then

$$\nu = \frac{V_i}{l_j}N_i. \quad (19)$$

Here, it stands to reason that clouds of one (the ith) star fly through the wind of the other (jth) star. Of course, the same result is obtained from the opposite point of view. Substituting the expressions for N_i and l_j obtained above into this equation, we arrive at the formula

$$\nu\ (\text{s}^{-1}) = 60.5\frac{\dot{M}_5^{\text{WR}}\dot{M}_5^{\text{OB}}}{\sqrt{\mu_{\text{WR}}\mu_{\text{OB}}}R_{14}(w_{3000}^{\text{WR}}w_{3000}^{\text{OB}})^2 d_{10}^2}. \quad (20)$$

It follows that, for clouds with $d_{10} = 1$, μ can be up to 8 s^{-1} at apoastron and 90 s^{-1} at periastron, if the flux is made up primarily of clouds of this size.

We will now estimate the luminosity of one pair of clouds assuming that at least one of them radiates. In this case, the total radiation flux summed over all frequencies is equal to the flux of the matter passing through the front. Therefore, the luminosity of a single cloud L_1 is expressed in terms of its surface area S_1, the density of unperturbed gas in the cloud ρ, and the speed of the shock [31]:

$$L_1 = \frac{1}{2}S_1\rho u^3.$$

Substituting (13) into this expression, we arrive at a lower limit for the luminosity of the radiating cloud

$$L_1 = 1.23 \times 10^{34}\sqrt{\mu}d_{10}w_{3000}^5 \text{ erg/s}. \quad (21)$$

It follows that a collision of a single pair of clouds could give rise to fairly powerful emission. The duration of the collision is described by the dynamical time scale, which, according to (8), is equal to

$$t_D \approx 30\frac{d_{10}}{w_{3000}} \approx 30 \text{ s}.$$

To provide the observed X-ray luminosity of HD 193793, it is sufficient to have $\nu \approx 0.1$ s. This is roughly a factor of 100 lower than the above values of 8 and 90 s^{-1}, and could be provided by a relative modest fraction of stellar-wind clouds.

5. THE X-RAY LIGHT CURVE

The X-ray light curve for HD 193793 is primarily determined by variation in the distance r between the two stars. Due to the large separation of the components, neither eclipses of the stars nor the exit of the wind into a steady-state velocity regime are important here. An appreciable role is played by radiative cooling of the gas. We will distinguish two limiting cases: adiabatic expansion of the gas after passage of the front, and fully radiative cooling of the gas. In Section 3, we considered the emission of the rarified wind component; we will now discuss the behavior of the clouds.

We will assume that the radiative-cooling condition (17) is satisfied, and elucidate the dependence of the luminosity on distance between the components for such clouds. We assume that, in each collision, at least one of the clouds completely radiates away its energy. Therefore, the X-ray light curve is determined by the probability p for the collision of a cloud with a cloud of the other star's wind. We substitute into (16) the number of clouds in a sphere of radius R, expressed as the ratio of the total enclosed cloud mass (14) to the mass of a single cloud, which is equal to the product of the cloud density ρ and the volume of a single cloud $\pi d^3/6$. We obtain in this way

$$p = \frac{3}{2\pi}\frac{\dot{M}}{V}\frac{1}{\rho R d}. \quad (22)$$

When the separation of the stars is large, a cloud travels through a large distance and appreciably expands before its passage into the "foreign" wind. By virtue of pressure balance with "its own" rarified gas component, the density of the cloud ρ is proportional to the density of the rarified gas; i.e., R^{-2}. We will assume that $d \propto \rho^{-1/3}$. Consequently, the product $\rho R d$ in the denominator of (22) falls off as $R^{-1/3}$, and the probability p grows as $R^{1/3}$.

Thus, in our colliding cloud model, the X-ray luminosity grows weakly with increase in the component separation, rather than falling off. This result can easily be brought into agreement with the observations of HD 193793. We propose a model for the X-ray emission of this system in which a large fraction—about 80%—of the observed flux is contributed by cloud collisions, while 20% is provided by the rarified wind component. When the distance between the stars changes in time due to the orbital motion of the system, the contributions of the clouds and rarified medium change in opposite senses. For the sake of concreteness, let us consider the orbital phase associated with recession of the components. During this interval, the modest increase in the cloud luminosity is compensated by the appreciable weakening of the contribution of the rarified wind component, and the X-ray luminosity of the system as a whole remains approximately constant. Analogous changes, but with opposite signs, occur during mutual approach of the stars.

One distinguishing property of cloud collisions is their discrete nature, which may be reflected in the behavior of the X-ray fluctuations. The role of fluctuations is determined by the dimensionless parameter

$$q = \nu t_D.$$

When $q \gg 1$, many clouds are interacting at any moment in time, and flares associated with individual collisions are averaged together. On the contrary, if $q \leq 1$, the role of each flare grows, and fluctuations in the luminosity on time scales t_D and $1/\nu$ could be observed. The actual value of q depends on the mass spectrum of the clouds. If a sufficiently large wind mass is contained in clouds with sizes $d_{10} \approx 1$, then, according to the estimates presented above, ν lies in the range from 240 (apoastron) to 2700 (periastron). In this case, the X-ray luminosity has a quasi-continuous character. However, if the mass spectrum is shifted toward denser and more compact clouds, emission in the form of brief, bright flares separated by time intervals of the order of $1/\nu$ could be observed.

Of course, a realistic picture for interactions between clouds is much more complicated than that presented here. For example, we have not discussed the quite possible scenario in which clouds in one of the stellar winds cease to radiate as the distance between the components increases. This factor would make the cloud light curve depend on the distance between the components even more weakly than $r^{1/3}$. In addition, some role could be played by the X-ray emission of the rarified component perturbed by clouds of the "foreign" wind. This effect will be strongest for clouds that pass relatively close to the other star. We hope to consider these and other aspects of interactions of two-phase winds in more detail in future papers.

6. CONCLUSION

The strong elongation and large size of the binary system HD 193793 make it possible to see clearly the probable role of cloud collisions in the generation of its X-ray emission. The presence of clouds in the stellar winds can easily provide scenarios in which the luminosity of the system depends only weakly on the distance between the stars, as is observed. Of course, some role must be played by the interaction of the rarified wind components, which has been more often considered in the literature; however, it appears that this is not the deciding factor in this system. Our results are in agreement with the analysis of Cherepashchuk [22] mentioned in the Introduction. An answer to the question of how typical it is for cloudy wind structure to appreciably influence the observed X-ray emission of binary systems must wait for more detailed investigations of other objects.

REFERENCES

1. P. M. Williams, K. A. van der Hucht, and A. M. Pollock, Mon. Not. R. Astron. Soc. **243**, 662 (1990).
2. K. Koyama, M. Kawada, and Sh. Takano, Publ. Astron. Soc. Jpn. **42**, L1 (1990).
3. K. Koyama, Y. Maeda, and T. Tsuru, Publ. Astron. Soc. Jpn. **46**, L93 (1994).
4. A. M. Cherepashchuk, Perem. Zvezdy **16** (2), 226 (1967).
5. S. B. Pikelner, Astrophys. J. **2**, 97 (1968).
6. S. B. Pikel'ner and P. V. Shcheglov, Astron. Zh. **45**, 953 (1968) [Sov. Astron. **12**, 757 (1968)].
7. O. F. Prilutskiĭ and V. V. Usov, Astron. Zh. **53**, 6 (1976) [Sov. Astron. **20**, 2 (1976)].
8. S. P. Owocki and K. G. Gayley, Astrophys. J. Lett. **454**, L145 (1995).
9. S. A. Zhekov and A. V. Myasnikov, New Astron. **3** (2), 57 (1998).
10. K. V. Bychkov, S. E. Egorova, and N. A. Katysheva, Astron. Zh. **70**, 1146 (1993) [Astron. Rep. **37**, 579 (1993)].
11. K. V. Bychkov, S. E. Egorova, and N. A. Katysheva, Astron. Zh. **71**, 78 (1994) [Astron. Rep. **38**, 66 (1994)].
12. A. M. Pollock, Astrophys. J. **320**, 283 (1987).
13. I. R. Stevens, J. M. Blondin, and A. M. Pollock, Astrophys. J. **386**, 265 (1992).
14. A. V. Myasnikov, S. A. Zhekov, and N. A. Belov, Mon. Not. R. Astron. Soc. **298**, 1021 (1998).
15. M. G. Lebedev and A. V. Myasnikov, *Numerical Methods in Aerodynamics* [in Russian], Ed. by V. M. Paskonov and G. S. Roslyakov (Mosk. Gos. Univ., Moscow, 1988), p. 3.
16. M. G. Lebedev and A. V. Myasnikov, Fluid Dyn. (USSR) **25**, 629 (1990).
17. G. G. Chernyĭ, *Flows of Gas with Large Supersonic Speeds* [in Russian] (Fizmatgiz, Moscow, 1959).
18. V. V. Usov, Astrophys. J. **389**, 635 (1992).
19. Z. T. Baĭramov, N. N. Pilyugin, and V. V. Usov, Astron. Zh. **67**, 998 (1990) [Sov. Astron. **34**, 502 (1990)].
20. K. V. Bychkov and A. M. Cherepashchuk, Astron. Zh. **70**, 512 (1993) [Astron. Rep. **37**, 260 (1993)].
21. K. V. Bychkov, Astron. Zh. **56**, 781 (1979) [Sov. Astron. **23**, 438 (1979)].
22. A. M. Cherepashchuk, Astron. Zh. **67**, 955 (1990) [Sov. Astron. **34**, 481 (1990)].
23. A. M. Cherepashchuk, *Wolf–Rayet Stars: Binaries, Colliding Winds, Evolution (IAU Symp. 163)*, Ed. by K. A. van der Hucht and P. M. Williams (Kluwer, Dordrecht, 1994), p. 262.
24. A. F. Moffat, L. Drissen, R. Lamontagne, and C. Robert, Astrophys. J. **334**, 1038 (1988).
25. I. I. Antokhin, T. Nugis, and A. M. Cherepashchuk, Astron. Zh. **69**, 516 (1992) [Sov. Astron. **36**, 260 (1992)].
26. A. M. Cherepashchuk, Itogi Nauki Tekh., Ser. Astron. **38**, 60 (1988).
27. L. D. Landau and E. M. Lifshitz, *Course of Theoretical Physics, Vol. 6: Fluid Mechanics* (Nauka, Moscow, 1986; Pergamon, New York, 1987).
28. S. B. Pikel'ner, *Fundamentals of Cosmic Electrodynamics* (Fizmatgiz, Moscow, 1966; NASA, Washington, DC, 1964).
29. I. S. Shklovsky, *Supernovae* (Nauka, Moscow, 1976; Wiley, London, 1968).
30. L. Spitzer, *Physics of Fully Ionized Gases* (Interscience, New York, 1962, 2nd ed.; Mir, Moscow, 1957).
31. S. A. Kaplan and S. B. Pikel'ner, *The Interstellar Medium* [in Russian] (Fizmatgiz, Moscow, 1963).
32. O. V. Aleksandrova and K. V. Bychkov, Astron. Zh. **32**, 532 (1998) [Astron. Rep. **42**, 469 (1998)].

Translated by D. Gabuzda

Astronomy Reports, Vol. 44, No. 12, 2000, pp. 790–803. Translated from Astronomicheskiĭ Zhurnal, Vol. 77, No. 12, 2000, pp. 893–908.

Non-LTE Effects in Na I Spectral Lines in Stellar Atmospheres

L. I. Mashonkina, V. V. Shimanskiĭ, and N. A. Sakhibullin

Kazan State University, Kazan, Russia

Received August 20, 1999

Abstract—The paper examines the statistical equilibrium of Na I in stellar atmospheres with a wide range of parameters: $T_{\rm eff}$ = 4000–12500 K, $\log g$ = 0.0–4.5, and heavy element content [A] from 0.5 to –4.0. The effect of the "overrecombination" of Na I (i.e., excess relative to the equilibrium number density of Na I) is present over the entire range of parameters considered, and increases with $T_{\rm eff}$ and luminosity. Na I lines are stronger than in the LTE case, so that non-LTE corrections to the sodium abundance, Δ_{NLTE}, are negative. Eight Na I lines commonly employed in abundance analyses are used to construct the dependences of the non-LTE corrections on $T_{\rm eff}$, $\log g$, and metallicity. The non-LTE corrections are small only for the Na I λλ615.4, 616.0 nm lines in main-sequence stars: $|\Delta_{NLTE}| \le 0.08$ dex. In all other cases, Δ_{NLTE} depends strongly on $T_{\rm eff}$ and $\log g$, and a non-LTE treatment must be applied if the sodium abundance is to be determined with an accuracy no worse than 0.1 dex. The profiles of solar Na I lines are analyzed in order to empirically refine two types of atomic parameters required for the subsequent analysis of the stellar spectra. In the solar atmosphere, inelastic collisions with hydrogen atoms influence the statistical equilibrium of Na I only weakly, and the classical Unsold formula underestimates the van der Waals constant C_6. The empirical correction $\Delta \log C_6$ is from 0.6 to 2 for various Na I lines. The sodium abundance in the solar atmosphere is determined based on line-profile analyses, yielding different results depending on whether the model atmospheres of Kurucz ($\log \varepsilon_{\rm Na} = 6.20 \pm 0.02$) or Holweger and Muller ($\log \varepsilon_{\rm Na} = 6.28 \pm 0.03$) are applied. © *2000 MAIK "Nauka/Interperiodica".*

1. INTRODUCTION

The element sodium manifests itself in stellar spectra predominantly via the lines of its neutral state. The lines of Na II—a Ne-like atom—originating from the ground state are in the far ultraviolet (λ < 40 nm), and the subordinate lines are too weak to detect due to the high potentials of the excited levels between which they form. Na III is present only in very hot stars. Lines of Na I are observed in stars with a wide range of spectral types (from M to middle B) and metallicities (to –3.5), providing the opportunity to study two astrophysical problems.

The first is the variation of the sodium abundance in the atmospheres of stars during their evolution. Denisenkov [1] and Prantzos *et al.* [2] explain the excess sodium observed in the atmospheres of F, G, and K supergiants as a result of enrichment in sodium via the ^{22}Ne^{23}Na cycle and the transport of the enriched material to the surface. The refinement of our understanding of this process (thermonuclear reaction rates, neon isotope ratios) requires the determination of the observed sodium excess as accurately as possible. A sodium excess has also been detected in A supergiants [3]. The mechanism behind this is not yet clear, but is most probably also associated with the evolution of these stars.

The second problem that can be attacked using observations of Na I lines is the evolution of the sodium abundance over the lifetime of the Galaxy. In this case, the objects of interest are low-mass stars that were born in early epochs in the lifetime of the Galaxy, but have not yet left the main sequence; i.e., they belong to a variety of populations. The analysis of sodium abundances in stars with such a wide range of parameters requires the use of all observable Na I lines, including the strongest resonance doublet λλ589.0, 589.6 nm and the λλ818.3, 819.5 nm doublet.

Therefore, the most physically plausible approach must be employed when deriving theoretical profiles and equivalent widths of spectral lines, without assuming local thermodynamic equilibrium. Like hydrogen, the Na I atom has a single valence electron and a simple energy-level structure. This has two advantages in Na I statistical-equilibrium analyses: the simpler model for the atom and simpler cross-sections for atomic processes.

For this reason, non-LTE analyses of the formation of Na I lines have been carried out in a number of studies. We will make note of the most important of these. Bruls *et al.* [4] carefully investigated mechanisms for deviation from LTE for Na I in the solar atmosphere. In our earlier paper [5], we showed that, even in the dense

and cool atmospheres of F and G dwarfs, both resonance and subordinate lines of Na I are subject to deviations from LTE. Takeda [6] first described line profiles for the strongest subordinate doublet, Na I λλ818.3, 819.4 nm, in the solar spectrum and empirically refined the associated van der Waals broadening constant and the role of collisions with hydrogen atoms in the statistical equilibrium of Na I. Boyarchuk *et al.* [7], Drake [8], and Takeda and Takeda-Hidai [3] considered the influence of deviations from LTE on Na abundance estimates for F and K supergiants. Baumuller *et al.* [9] analyzed the profiles of 15 Na I lines in the solar spectrum, and used the resulting refined atomic line parameters to determine the non-LTE Na abundances for a sample of G and K Galactic disk and halo stars for the first time; the results indicated a large deficit of sodium in halo stars, which grows as the heavy-element content decreases.

Understanding the importance of studying Na abundances for stars of various types, we set out to investigate the formation of Na I lines using a non-LTE approach for a wide range of stellar effective temperatures ($T_{\rm eff}$ = 4000–12000 K), surface gravities ($\log g$ = 0.0–4.5), and heavy-element contents ([A] = 0.5 to –4.0), in order to provide a theoretical basis for studies of sodium abundances. It is important to note that our work was carried out using the new models of Kurucz [10], while previous studies have used either their own model atmospheres [9] or the earlier models of Kurucz [6]. Here, we show that our results depend appreciably on the choice of model atmosphere. For example, it is especially important to take into account non-LTE effects in studies of Na I lines in stellar spectra based on the models [10].

We have built upon our previous work, but our method for performing the non-LTE computations has been appreciably improved. We describe this method in Section 2. In Section 3, the method is applied to an analysis of solar Na I lines. Agreement between the observed and theoretical non-LTE profiles for 11 Na I lines in the visible and infrared is achieved; we derive empirical corrections to the Unsold damping constant C_6 for each line, and estimate the efficiency of inelastic collisions with H atoms in the statistical equilibrium of Na I. These atomic parameters are important for future analyses of stellar Na I lines. In Section 4, we discuss deviations from LTE in spectral lines as functions of $T_{\rm eff}$, $\log g$, and [A].

2. METHOD FOR THE NON-LTE CALCULATIONS

Let us note certain changes in the method used for the non-LTE computations for Na I compared to our previous work [5]. The Na I model includes 21 levels: all levels from $l \le 3$ and $n \le 7$. We take into account the fine structure of the 3*p* state, which proved to be important, as we will show below. Our model atom is not as complete as those in [3, 9], which had 93 and 80 levels, primarily because they included highly-excited levels with $n > 7$. However, test computations (see below) indicate that leaving out these levels does not lead to errors in estimates of non-LTE effects. The atomic parameters are the same as those in [5] except for photoionization and photorecombination; for the ground state, we used a photoionization cross section calculated using the Hartree–Direc–Slater method [11].

For the remaining levels, we adopted cross sections computed using the quantum-defect method of [12]. We compared these cross sections, as well as the oscillator strengths f_{ij} from [13–15], with data computed as part of the OPACITY project, accessible in the TOPbase database of atomic data. For all important transitions, the difference f_{ij} was no more than 3%, and could reach 10% for weak transitions between highly-excited levels. Differences at this level should not appreciably influence the results of the non-LTE computations.

The photoionization used in our study and in the TOPbase database differ only slightly for the *ns*, *np*, and *nd* levels; Fig. 1 presents a comparison for the most important levels, 3*s*, 3*p*, and 3*d*. The difference is greater for the *nf* levels—the TOPbase cross sections near the threshold are a factor of 1.5 lower than the data from [12] (Fig. 1d). We performed test computations introducing the TOPbase photoionization cross sections for the *nf* levels. The non-LTE effects changed by only a negligibly small amount: for three model atmospheres with various $T_{\rm eff}/\log g$ /[A] (namely, 5000/0.0/–2, 6500/4.0/0, and 9000/4.0/0) and for various lines, the variations in the non-LTE corrections to the Na abundance did not exceed 0.014 dex. This indicates the small infuence of the photoionization and photorecombination for the *nf* levels in mechanisms for deviations from LTE for Na I.

We carried out the computations using the NONLTE3 code [16], which is based on a full linearization method in the form adopted by Auer and Heasley [17]. The usual sources of opacity considered in such studies include H, He, H^-, H_2^+, atoms and singly charged ions of the most abundance elements, scattering on electrons, and Rayleigh scattering. In addition to these, we took into account the contribution of numerous spectral lines when computing the continuum absorption coefficient, via direct summation of their absorption coefficients at each frequency. Our line list was based on that of Kurucz [10], and contained about 150 thousand lines with wavelengths greater than 91.2 nm. For the model atmospheres with $T_{\rm eff} < 6000$ K, we took into account molecular absorption using data kindly presented by Ya. Pavlenko.

When computing the line profiles and equivalent widths W_λ, which are usually used when determining Na abundances, we allowed for natural damping using the relation $\gamma_R(ij) = \sum_l A_{il} + \sum_l A_{jl}$, Stark broaden-

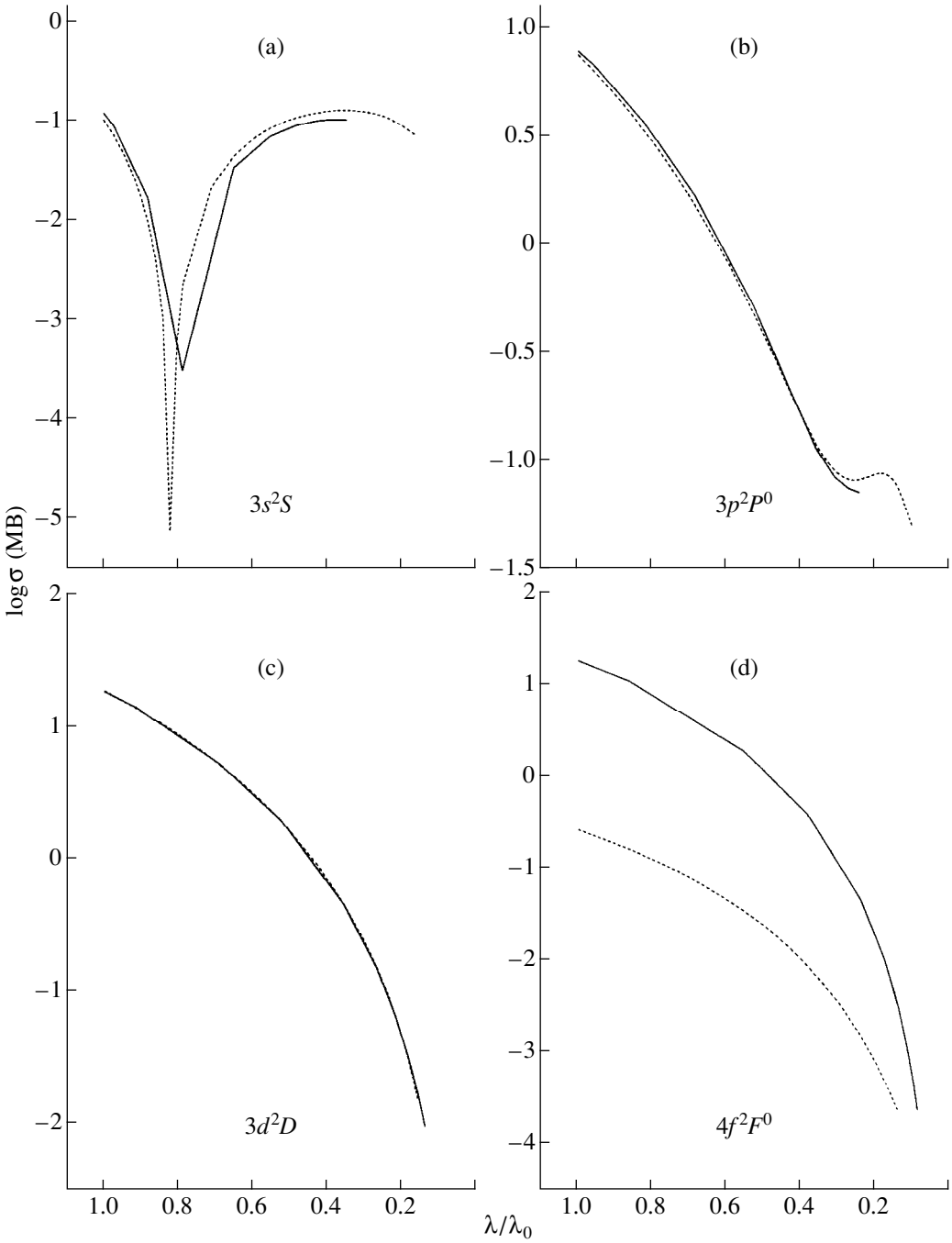

Fig. 1. Comparison of photoionization cross sections from TOPbase (dashed curves) and computed using the quantum-defect method of [12] (solid curves) for individual Na I levels.

ing using C_4 taken from [18], and van der Waals broadening using C_6 determined from a comparison of theoretical and observed solar line profiles (see Section 3). We calculated the source function assuming total redistribution over frequency. The basis for this was the results of Curtis and Jefferies [19], whose empirical studies of the Na I D lines in the solar spectrum indicated that the source function within line profiles does not depend on frequency. We allowed for fine structure only for resonance lines, using data from [20]. All computations were based on the model atmospheres of Kurucz [10].

To verify that the adopted model for the Na I atom was sufficiently complete to yield sound estimates of non-LTE effects in the Na I lines, we compared our results with those of [3], in which a 93-level model atom was used. For four model atmospheres with parameters corresponding to the Sun (5770/4.44/0, V_{mic} =

1 km/s), αPer (6500/1.0/0, V_{mic} = 4.5 km/s), Procyon (6500/4.0/0, V_{mic} = 2 km/s), and Sirius (10000/4.0/0, V_{mic} = 2 km/s), we carried out non-LTE computations and derived non-LTE corrections to the sodium abundances $\Delta_{NLTE} = \log\varepsilon_{NLTE} - \log\varepsilon_{LTE}$ for each line measured in the spectra of these stars. Like the authors cited above, we used the model atmospheres of [21], and used the formula of Steenbock and Holweger [22] without a scaling coefficient when calculating the rates of collisional excitation and ionization by atomic hydrogen. For all lines for the Sun, Procyon, and Sirius, our Δ_{NLTE} coincide with the results of [3] to within 0.01 dex. Non-LTE effects are more substantial in the supergiant αPer than in dwarfs; however, in this case, too, for two lines of three, the difference Δ_{NLTE} did not exceed 0.01 dex, and was equal to 0.05 dex for the λ819.5 nm line. However, we were able to eliminate this difference after unifying the fine structure sublevels $3p^2P^0_{1/2}$ and $3p^2P^0_{3/2}$ into a single $3p$ level, as was done in [3].

Let us try to explain why the results for our 20-level model atom were no worse than those for the 93-level model atom. On the one hand, indeed, highly-excited states play an important role in determining deviations from LTE in Na I. As discussed in [3–5, 8], lower levels of Na I are overpopulated relative to the equilibrium populations due to recombination to highly-excited levels and subsequent cascade transitions to lower-lying levels. On the other hand, recombination occurs most efficiently to those levels whose threshold ionization energies E_{thr} are of the same order as the mean kinetic energy of the electrons kT_e. For stars with $T_{\rm eff}$ = 10000 K, $kT_e \simeq 0.9$ eV, while it is half of this in stars with $T_{\rm eff}$ = 5000 K. Our model atom includes all levels with $E_{thr} \geq 0.28$ eV, and the comparison of our results with those of [3] shows that this was sufficient to ensure a correct treatment of the statistical equilibrium of Na I. These computations allow us to draw two more important methodical conclusions.

(1) The fine-structure sublevels of the $3p^2P^0$ term should be included in the model of the Na I atom as separate levels, as we have done. This can be explained as follows. The two strongest Na I transitions $3s$–$3p$ and $3p$–$3d$ are associated with the $3p$ level. Deviations from LTE begin in layers where photons begin to appear in the line wings; i.e., where the corresponding optical depth becomes less than unity. The depth of the formation of individual lines of a multiplet is larger than for the line as a whole; therefore, when taking into account the fine splitting of the $3p$ level, the detailed balance in the $3s$–$3p$ and $3p$–$3d$ transitions begins to be disrupted in deeper layers than when the $3p^2P^0$ term is considered as a single level. Therefore, non-LTE effects in the level populations and line intensities are different in these two cases.

(2) We conducted non-LTE computations using the new models of Kurucz [10] for these same four stars, and compared the resulting Δ_{NLTE} and $\log\varepsilon_{\rm Na}$ values derived with models from the different model-atmosphere grids. The non-LTE corrections to the sodium abundance Δ_{NLTE} were virtually identical for the new and old model atmospheres of Kurucz: the difference was 0.02–0.03 dex for resonance lines and 0.00–0.02 dex for subordinate lines. At the same time, the sodium abundances obtained using the models of [10] were systematically higher than those for the models of [21]. For resonance lines, this difference was maximum for the Sun (0.12 dex), and decreased to 0.06 dex for Sirius. For subordinate lines, this difference was 0.03–0.07 dex for various lines.

3. ANALYSIS OF NA I LINES IN THE SOLAR SPECTRUM

The Sun was chosen as a star with reliably measured fundamental parameters for which high quality spectral observations were available. For the Sun, it is possible to analyze profiles of lines that contain more information about the physical conditions in the atmosphere than do equivalent widths. In this section, we present the results of fitting the observed profiles of 11 Na I lines with theoretical non-LTE profiles. Analysis of these line profiles can be used to accurately determine the solar Na abundance, and also empirically refine two types of atomic parameters: the van der Waals broadening constant and the rates of collisional excitation and ionization by atomic hydrogen.

We used the spectral atlas of the Sun as a star [23] derived for wavelengths from 296 to 1300 nm with spectral resolution $\lambda/\Delta\lambda$ = 522000 and signal-to-noise ratio S/N = 2000–9000. Of the 40 Na I lines in this interval, only 15 proved to be unblended or only weakly blended. We analyzed the profiles of 11 of these, and three weaker lines were included in our subsequent analysis of the line equivalent widths. The continuum level was corrected only for a single line (λ1267.9 nm), by dividing the atlas data by 0.9335. The effect of the instrumental profile was taken into account by folding a theoretical profile with a Gaussian with the FWHM 0.0012 estimated from the spectral resolution. The influence of the instrumental profile was small: for example, for one of the weak lines (λ615.4 nm), the relative intensities changed by no more than 0.006 after convolution. Table 1 presents a list of the lines considered, their parameters, and the observed equivalent widths $W_\odot$. The errors σ reflect the dispersion in W_λ when the equivalent widths are measured in different ways: integration over the profile or the half-profile, and approximation of the profile as Gaussian or Lorentzian.

We conducted calculations for two solar model atmospheres with the same parameters, $T_{\rm eff}$ = 5770 K and $\log g$ = 4.44: we will refer to the model of [10] as newKur and that of [24] as HolMul. We used a combined model with a chromospheric rise to calculate the profiles of resonance lines, obtained by matching the

Table 1. Sodium line parameters

λ, nm	Transition	f_{ij}	$\log C_6$(U)	$\Delta\log C_6$	$W_\odot \pm \sigma$, mÅ
588.997	$3s^2S$–$3p^2P^0_{3/2}$	0.647	−31.88	0.71	830 ± 15
589.584	$3s^2S$–$3p^2P^0_{1/2}$	0.322	−31.88	0.71	640 ± 15
615.423	$3p^2P^0_{1/2}$ –$5s^2S$	0.014	−30.58		41 ± 4
616.075	$3p^2P^0_{3/2}$ –$5s^2S$	0.014	−30.58		63 ± 5
568.821	$3p^2P^0_{3/2}$ –$4d^2D$	0.0967	−30.53	0.73	144 ± 3
568.264	$3p^2P^0_{1/2}$ –$4d^2D$	0.097	−30.53	1.02	121 ± 8
818.326	$3p^2P^0_{1/2}$ –$3d^2D$	0.830	−31.26	0.83	254 ± 5
819.482	$3p^2P^0_{3/2}$ –$3d^2D$	0.833	−31.26	0.84	328 ± 10
498.281	$3p^2P^0_{3/2}$ –$5d^2D$	0.031	−30.08	1.92	97 ± 8
449.766	$3p^2P^0_{3/2}$ –$7d^2D$	0.0075	−29.45		33 ± 5
514.884	$3p^2P^0_{1/2}$ –$6s^2S$	0.0044	−30.13		12.5 ± 2
1074.644	$4s^2S$–$5p^2P^0_{3/2}$	0.0385	−30.44		19 ± 3
1083.487	$3d^2D$–$6f^2F^0$	0.0556	−29.80		51.5 ± 4
1267.917	$3d^2D$–$5f^2F^0$	0.159	−30.19	1.99	142 ± 3

Note: C_6(U) are the Unsold constants [28]. $\Delta\log C_6$ is determined by comparing the observed and theoretical profiles. $W_\odot$ are the observed equivalent widths in the solar spectrum.

model of Kurucz [10] and part of the VAL-C' model [25] above the temperature minimum. Taking the chromosphere into account decreases the theoretical central depths of the resonance lines by 2.4%, providing a better agreement with observations. All the theoretical profiles were broadened by rotation with $V\sin i$ = 2 km/s.

The effect of solar granulation on line profiles usually imitates radial–tangential macroturbulence. We estimated the macroturbulence parameter V_{RT} empirically via analysis of Na I lines profiles [6, 9], and found it to be from 2 to 4 km/s. Our analysis indicates that the profiles of the strongest Na I resonance lines are insensitive to this parameter, and a good agreement between the observed and theoretical profiles can be achieved both in the absence of macroturbulence and taking macroturbulence into account using the same sodium abundances and van der Waals broadening constants (Figs. 2a, 2b). For the strong λλ818.3, 819.4 nm subordinate doublet, our estimates indicate that V_{RT} cannot exceed 2.1 km/s, and the most probable value is V_{RT} = 1.9 km/s. Note that similar values have been derived for this doublet in other studies: Takeda [6] gives V_{RT} = 2.0 and 2.7 km/s, and Baumuller *et al.* [9] give V_{RT} = 2.8 and 2.2 km/s for λ818.3 and λ819.4 nm, respectively.

For the weakest lines, including the λλ615.4, 616.0 nm doublet, it was not possible to establish a single best value of V_{RT}, since variation of V_{RT} from 0 to 3.5 km/s could be compensated by changing the constant C_6. For such weak lines, variation of C_6 essentially does not affect the equivalent widths, so that it is possible, by increasing the classical Unsold constant $C_6(U)$ by a factor of 100 and not taking into account macroturbulence, to achieve an equally good fit of the λλ615.4, 616.0 nm line profile as is obtained using $C_6(U)$ and V_{RT} = 3.5 km/s. Therefore, we preferred to use weak Na I lines only when determining the sodium abundance. When analyzing the profiles of all lines, we used the single value V_{RT} = 1.9 km/s found using the λλ818.3, 819.4 nm lines.

The theoretical line profiles depend on many parameters. These include atomic parameters such as f_{ij}, the damping constants γ_R, C_4, and C_6, the rates of collisional and radiative processes influencing the statistical equilibrium of the Na I atom, and physical parameters such as $T_{\rm eff}$, $\log g$, the heavy-element content, and the microturbulence velocity. When analyzing solar Na I lines, $T_{\rm eff}$ and $\log g$ can be fixed, f_{ij} and γ_R for Na I lines are known with fair certainty (see Section 2), and Stark broadening under the conditions of the solar atmosphere is negligible compared to van der Waals broadening, so that accurate knowledge of C_4 is not very crucial. As test computations by both us and other authors

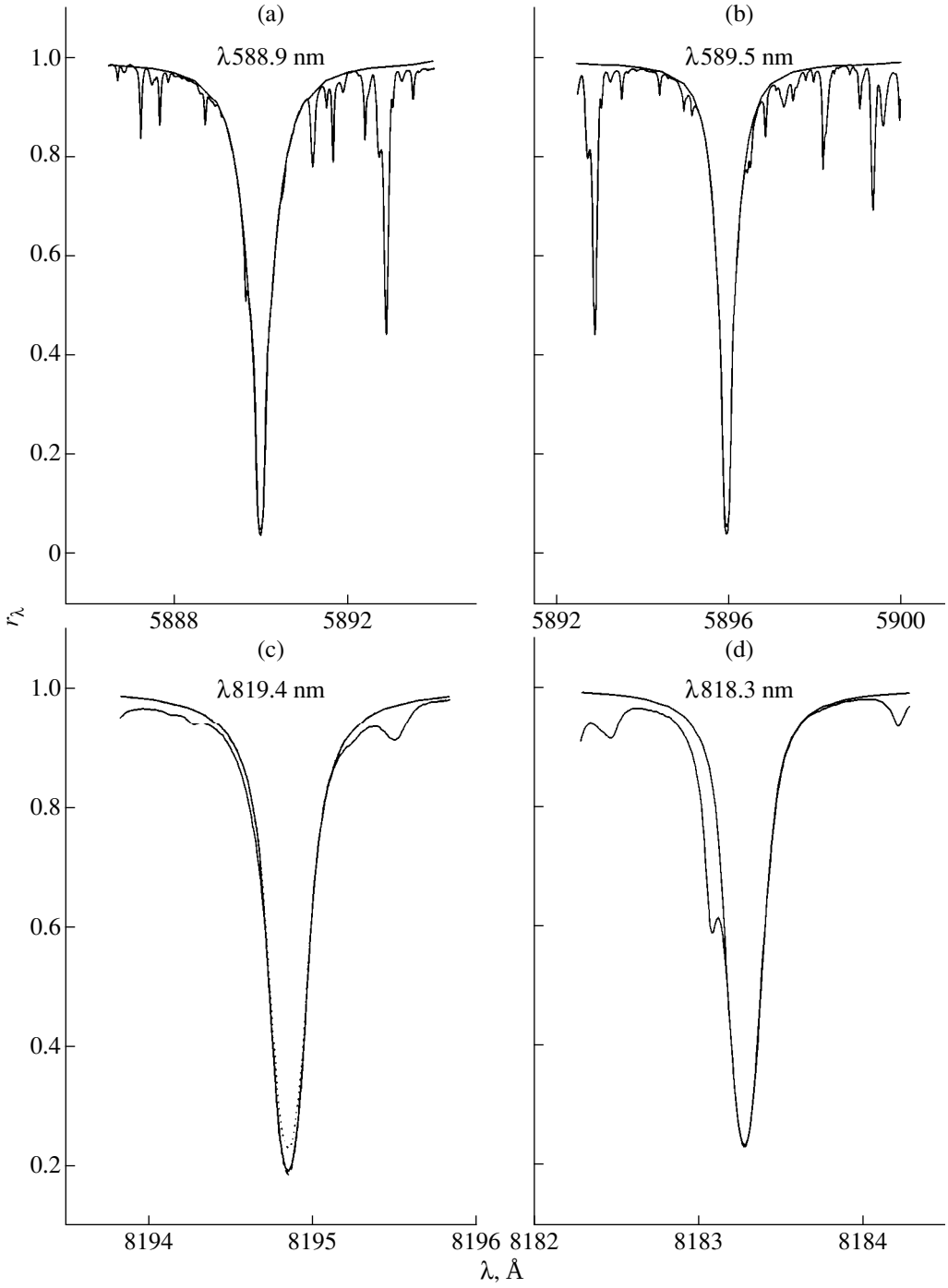

Fig. 2. Profiles of the strongest Na I lines observed in the solar spectrum and theoretical non-LTE profiles computed for the newKur model with $k_H = 0.1$. The line parameters and sodium abundances corresponding to the theoretical profiles are presented in Tables 1 and 2; $V_{mac} = 1.9$ km/s. The dotted curve in Fig. 2c corresponds to $k_H = 1$, and the dashed curve to $k_H = 0$.

[4, 9] have shown, the statistical equilibrium of Na I is stable to variations in the photoionization cross sections and rates of collisional excitation and ionization by electrons that are within the errors in these quantities.

In the atmospheres of solar-type stars, where electron number densities are low, the collisional excitation and ionization of atoms can also come about via collisions with hydrogen atoms. Some authors, such as Bruls *et al.* [4], consider the role of these processes to be negligibly small. However several other sets of test computations for various atoms and ions [3, 6, 9] have demonstrated that taking into account only collisions

with electrons underestimates the role of collisional processes compared to that of radiative processes.

We used the formula of Steenbock and Holweger [22] when computing the rates of collisions with H atoms, which is accurate only to an order of magnitude. Introducing the scaling coefficient k_H into this formula, we can vary the role of collisions with H atoms in the statistical equilibrium of Na I. Thus, one of our free parameters when fitting the theoretical profiles to observations was k_H. We carried out non-LTE computations for k_H = 0, 0.1, 0.2, 0.33, and 1.0. Other free parameters were the sodium abundance $\log\varepsilon_{Na}$, the van der Waals broadening constants C_6 for each line, and the microturbulence velocity V_{mic}.

It rapidly became clear that it was not possible to make a definite choice of V_{mic} based on analysis of the Na I lines, due to the very weak sensitivity to variations in this parameter. For the Sun, estimates from various studies yield V_{mic} values from 0.8 to 1.2 km/s, while the thermal velocity of sodium atoms everywhere in the solar atmosphere exceed 2 km/s. We were able to achieve the best agreement between the observed and theoretical profiles for various Na I lines using V_{mic} values from 1 to 1.2 km/s. Varying V_{mic} by 0.2 km/s had essentially no effect on our estimation of the other free parameters.

We first estimated k_H. The most suitable lines for this were the λλ819.4, 818.3 nm doublet, which were most sensitive to deviations from LTE, and thereby to variations in k_H. The cores of these lines are saturated, so that their central intensities are insensitive to variations in the sodium abundance. Figure 2c presents theoretical profiles for the λ819.4 nm line for k_H = 0, 0.1, and 1 and $\log\varepsilon_{Na}$ = 6.18. We can see that varying k_H only affects the intensity in the line core, and we can estimate k_H once we have fixed the Na abundance and the constant C_6 using the line wings. The best agreement with the observed profiles in the line core is achieved for k_H = 0.1. We should note, however, that the profiles for k_H = 0 and k_H = 0.1 virtually coincide, so that we can only take k_H to be somewhere in the range from 0 to 0.1. We obtained the same result for the HolMul model. If we assume that there is no macroturbulence broadening the lines, we achieve a satisfactory description of the Na I line cores with a larger value k_H = 0.33. In [3], the scaling coefficient k_H was also sought based on analysis of solar profiles for this same doublet, but using the model atmosphere of [21], yielding k_H = 0.1. Using the same approach with their own model atmosphere, Baumuller *et al.* [9] estimated that k_H does not exceed 0.5, and that the most probable value was 0.05. Thus, results obtained in various studies are all more or less consistent, and provide evidence that the role of collisions with H atoms in determining the statistical equilibrium of Na I is modest.

Further, with k_H fixed, we determined C_6 and $\log\varepsilon_{Na}$ simultaneously for each Na I line. This method was based on the idea that the cores of all subordinate lines except for λλ819.4, 818.3 nm are sensitive to variation of the abundance, while the wings are sensitive to variation of C_6. For each line, we went through several iterations to find the final best pair of values for C_6 and $\log\varepsilon_{Na}$. Agreement between the observed and theoretical profiles was achieved for the newKur model with V_{RT} = 1.9 km/s and k_H = 0.1. Figures 2 and 3 present the results for the newKur model. The resulting corrections to the Unsold constants $\Delta\log C_6$ are given in Table 1. Let us analyze the resulting $\Delta\log C_6$ values.

First, the corrections $\Delta\log C_6$ were found separately for each line. For resonance lines, our $\Delta\log C_6$ coincides with that obtained by Fullerton and Cowley [27] based on a refined particle-interaction theory, and similar values were obtained for the λλ568.2, 568.8 and λλ819.4, 818.3 nm doublets. The formula of Unsold [28] strongly underestimates C_6 for lines formed between highly-excited levels: for the λ1267.9, λ1083.4, and λ498.2 nm lines, we obtained $\Delta\log C_6 \geq 1.9$. Second, the $\Delta\log C_6$ values depend only weakly on the model atmosphere used. The values presented above were those for the newKur model. We also derived corrections $\Delta\log C_6$ for nine Na I lines using the HolMul model. These differed from the newKur values by no more than 0.08 dex. On the other hand, based on a profile analysis for the same lines but using their own solar model atmosphere, Baumuller *et al.* [9] conclude that essentially no corrections to the Unsold constants are required. Only for strong lines can $\Delta\log C_6$ reach 0.2 dex.

We attempted to apply the alternative pressure line-broadening theory developed by Deridder and van Rensbergen [26], based on a Smirnov–Roof potential. For infrared lines, such as λ1267.9 nm, using the data of [26] is equivalent to introducing corrections to the Unsold constant $\Delta\log C_6 \simeq 0.06$. Figure 3d compares theoretical profiles computed using the classical Unsold constant and the data of Deridder and van Rensbergen [26]. We can see that the alternative theory also underestimates the effects of pressure in the line wings, though to a lesser degree than the Unsold theory.

The non-LTE sodium abundances derived from our profile analysis are presented in Table 2 in the "From Profiles" columns for the newKur and HolMul models, in the form of corrections $\Delta\log\varepsilon$ to the initial abundance $\log\varepsilon_0$ = 6.25. Here, we have employed the widely used abundance scale in which $\log\varepsilon_H$ = 12 for hydrogen. The table also gives values averaged over all lines and their rms errors σ. In all cases, the scatter in

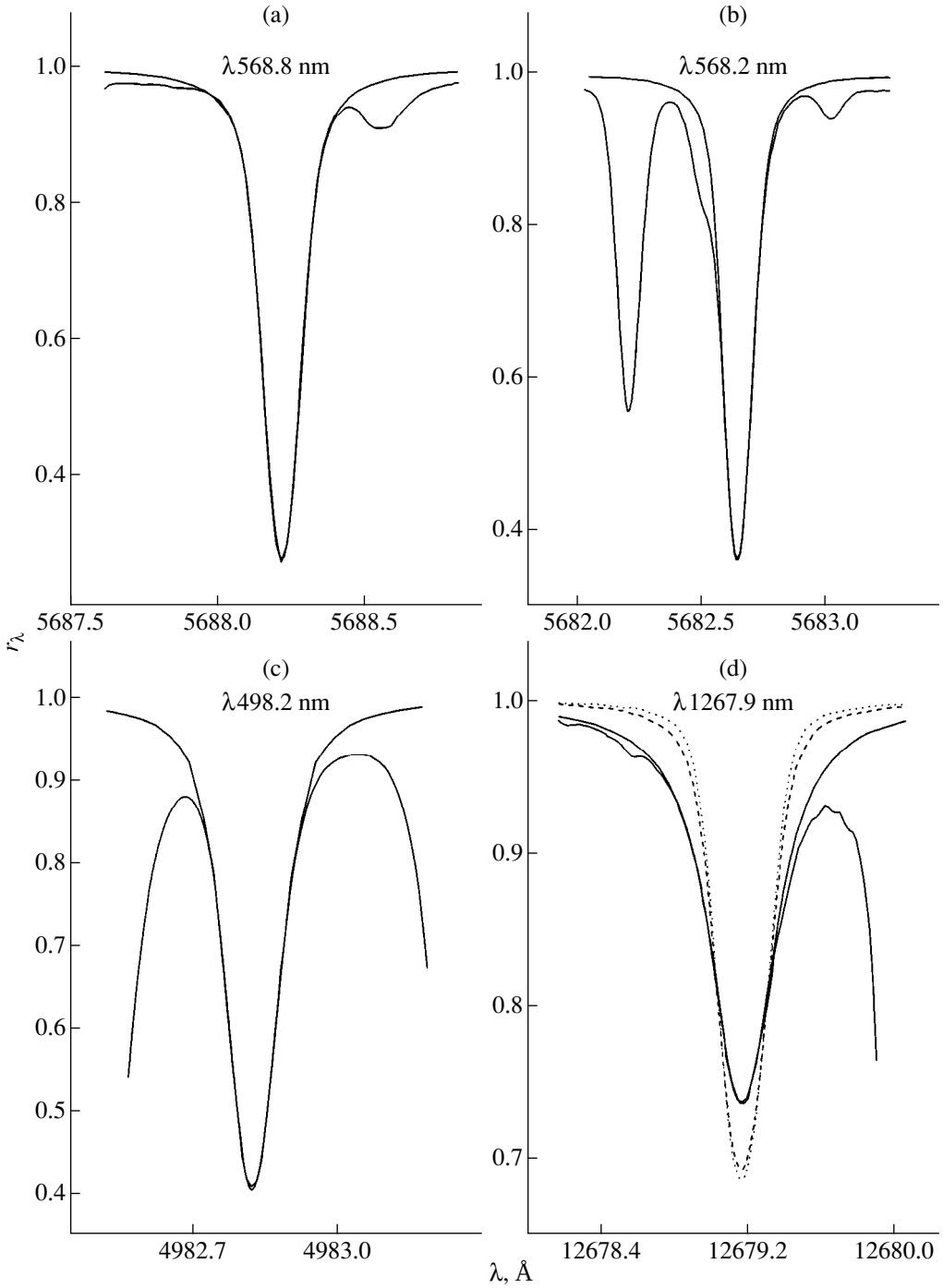

Fig. 3. Same as Fig. 2 for other Na I lines. Theoretical profiles for various means of taking into account van der Waals broadening are shown in Fig. 3d: using the classical theory of Unsold (dotted) and using the theory of Diridder and van Rensbergen [26] (dashed).

the non-LTE abundances derived for different lines is small, and σ does not exceed 0.03 dex.

However, the abundance does depend on the model atmosphere used: $\log\varepsilon_{Na} = 6.20$ for the newKur model and 6.28 for the HolMul model. The sodium abundance for the HolMul model coincides with the meteoritic abundance $\log\varepsilon_{Na} = 6.32$ [29] to within the errors. The newKur model yields a sodium abundance that is 0.12 dex lower than the meteoritic value and 0.08 dex lower than the HolMul value. This leads us to assert that the models of Kurucz [10] should not be employed for absolute sodium-abundance determinations. However, if differential determinations [Na/H] are obtained for specific

Table 2. Corrections (in 0.01 dex) to the sodium abundance $\log\varepsilon_0 = 6.25$ for solar Na I lines

λ, nm	newKur			HolMul		
	from profiles	from W_λ		from profiles	from W_λ	
	non-LTE	non-LTE	LTE	non-LTE	non-LTE	LTE
588.997	−5.1	−5.5	2.4	4.3	4.3	9.6
589.584	−4.6	−1.5	6.7	4.8	7.8	14.1
615.423		−0.8	3.0		4.0	8.5
616.075		−4.4	0.5		1.4	6.6
568.821	−3.8	−10.9	−3.7	3.9	−4.7	3.4
568.264	−5.5	−1.3	4.8	2.1	4.0	11.1
818.326	−1.1	−4.0	14.6	3.1	0.6	23.1
819.482	−7.4	−6.2	11.3	1.4	−1.3	20.1
498.281	−3.5	−6.9	−3.5	2.5	−1.3	2.6
449.766		−6.2	−3.8		−1.7	1.1
514.884		−5.8	−2.8		−1.0	1.8
1074.644		−6.8	−5.5		−2.3	−0.5
1083.487	−6.6	−7.2	−6.1	−2.5	−3.1	−1.5
1267.917	−5.0	−5.1	−3.9	1.0	−0.9	0.8
Mean	−4.7	−5.2	1.0	2.9	0.4	7.2
σ	1.8	2.7	6.4	3.0	3.5	7.7

stars using the models of [10], the appropriate value to use for the solar abundance is $\log\varepsilon_{Na} = 6.20$.

As a rule, line equivalent widths are used when determining the chemical composition of stars. Therefore, we decided to check whether we could achieve an equally good accuracy when estimating $\log\varepsilon_{Na}$ from the equivalent widths as we had from the line-profile analysis. For nine lines for which profiles were analyzed, we used the C_6 constants found above. We added five more weak lines with $W_\lambda \le 50$ mÅ, for which we used the Unsold constants. The results for individual lines, as well as for the mean values, are presented in Table 2 in the "from W_λ" columns. The differences in the abundances derived from the profiles and equivalent widths have different signs for different lines, i.e., they have a random character, and can reach 0.07 dex. It turned out that using the refined values for C_6 made it possible to achieve high accuracy in the sodium abundances derived from equivalent widths as well: the mean non-LTE $\log\varepsilon_{Na}$ differs from the profile-derived value by less than 0.01 dex for the newKur model and less than 0.03 dex for the HolMul model. The errors are also essentially the same: 0.03–0.04 dex.

If we adopt the Unsold constants for all lines without correction, this increases the sodium abundance (by 0.11 dex for the newKur model), and increases the dispersion by more than a factor of three: σ becomes 0.11 dex instead of 0.03 dex. We believe that, in the case of the Sun, it is precisely failure to take into account individual corrections to the Unsold constants that has led in most studies to a large scatter in the abundances derived using different lines, and to comparatively large errors, in spite of the high accuracy of the W_λ measurements used. For example, in [3], the scatter in the Na abundances found using 16 lines reaches 0.34 dex, and σ = 0.10 dex. The error in $\log\varepsilon_{Na}$ also grows due to failure to take into account deviations from LTE. Table 2 also presents results for the LTE case. The mean $\log\varepsilon_{Na}$ is larger than the non-LTE values (by 0.06 dex for the newKur model), and the dispersion more than doubles. Failure to take into account individual corrections to the Unsold constants and deviations from LTE are probably the main reasons for the large scatter (0.5 dex) in the sodium abundances derived using different lines and the large rms error σ = 0.13 dex obtained by Lambert and Warner [30].

Thus, analysis of Na I lines in the solar spectrum leads us to important conclusions for our subsequent abundance determinations.

(1) When performing differential abundance determinations, the model atmosphere for the comparison star (often the Sun) should be constructed in the same way as the stellar model atmospheres. Let us present an example. Using the solar Na I equivalent widths, k_H = 0.33, and the C_6 values derived from the newKur model [21], we obtained the non-LTE sodium abundances

$\log\varepsilon_{Na}$ = 6.18, 6.24, and 6.12 for the newKur model, HolMul model, and the model of [21], respectively. Consequently, if we were to use the HolMul model for the Sun but the model from [21] for the star, for example, [Na/H] for the star would be underestimated by 0.12 dex.

(2) When the model atmospheres of [10] are used, the well known formula of Unsold [28] underestimates the wings of lines experiencing van der Waals broadening, and it is necessary to introduce corrections $\Delta\log C_6$ that are different for different lines.

4. NON-LTE EFFECTS AS A FUNCTION OF STELLAR PARAMETERS

Here, we present for the first time the results of computations for the model-atmosphere grid [10] over a wide range of parameters: $T_{\rm eff}$ = 4000–12500 K with step 250 K, $\log g$ = 0.0–4.5 with step 0.5, and [A] = 0.5 to –4.0 with step 0.5. We took the sodium abundance $\log\varepsilon_0$ = 6.25 as the standard value. For models with non-standard heavy-element abundances, we changed the sodium abundance proportionally.

The computations showed that the phenomenon of "overrecombination" of Na I (i.e., excess compared to the equilibrium number of neutral sodium atoms), which was detected earlier for the Sun and solar-type stars, is characteristic of stellar atmospheres with the whole range of parameters considered. Overrecombination increases with growth in $T_{\rm eff}$, and with growth in $\log g$ at a fixed $T_{\rm eff}$. Figure 4 presents b factors for the Na I levels for three model atmospheres with different $T_{\rm eff}$. The b factors ($b_i = n_i/n_i^*$) characterize deviations of the level populations from their equilibrium populations n_i^*, given by the Boltzmann–Saha equation. When analyzing non-LTE effects observed in stellar lines, it is most important to consider the b factors for the 3s and 3p levels, since they are the lower levels for these transitions. We can see from Fig. 4 that, in all three cases, the 3s and 3p levels are overpopulated in the line formation region. The mechanism for this overpopulation is the predominance of recombination over ionization for highly-excited levels with ionization thresholds in the infrared, where the mean intensity J_ν determining the photoionization rate is lower than the local $B_\nu(T_e)$, on which the photorecombination rate depends, followed by subsequent cascade transitions to lower-lying levels. At $T_{\rm eff}$ = 6000 K, b(3s) and b(3p) differ from unity more strongly than at 4000 K, due to the increasing strength of radiative processes with temperature. Upon further increase in $T_{\rm eff}$, however, the Na I lines weaken, and their formation depth shifts toward deeper layers, where the role of collisions is great even at high temperatures; as a result, non-LTE effects in the level populations are even slightly smaller at $T_{\rm eff}$ = 10000 K than at 6000 K.

Figure 4 shows that, for each of the transitions giving rise to an observed Na I line, two relations are satisfied in the line-formation region:

(1) $b_i > 1$,

(2) $b_j/b_i < 1$.

Due to the first relation, the line absorption coefficient is higher than its LTE value. Due to the second relation, the source function in the line S_ν is smaller than the Planck function, since

$$S_\nu \simeq \frac{b_j}{b_i} B_\nu(T_e),$$

when $h\nu/kT_e > 1$. Both factors lead to an increase in the Na I lines compared to the LTE case, and to a decrease in the abundances derived using these lines.

Thus, non-LTE corrections to the abundances are always negative for Na I lines. We computed the non-LTE corrections to the abundance Δ_{NLTE} for eight Na I lines as the logarithmic shift between the non-LTE and LTE curves of growth for a specified W_λ corresponding to the normal sodium abundance for the given model atmosphere. Some of our results are presented in Figs. 5 and 6. In the plots, the upper boundary in $T_{\rm eff}$ is different for different lines, since the non-LTE corrections are given only for cases when the equivalent width was measured: $W_\lambda > 5$ mÅ. In Figs. 5a, 5d, 6a, 6b, and 6d, we can see jump-like variations in Δ_{NLTE} that occur at $T_{\rm eff}$ values that are the smaller, the smaller is $\log g$. The jumps arise only for weak lines, which form in the deepest layers, and are not a consequence of the method used for the non-LTE computations. They probably reflect sharp variations in the temperature distribution for specified values of $T_{\rm eff}$ and $\log g$, due to the peculiarities of accounting for convection in the models [20].

Let us consider Δ_{NLTE} for various Na I lines. When analyzing sodium abundances, preference is usually given to the Na I λλ615.4, 616.0 and λλ568.2, 568.8 nm doublets. Our computations indicate that only for the first of these doublets are deviations from LTE small over the entire range of parameters considered: $|\Delta_{NLTE}| \leq$ 0.08 dex for main-sequence stars and $|\Delta_{NLTE}| \leq 0.15$ dex for supergiants (Figs. 6a, 6b). For λλ568.2, 568.8 nm, $|\Delta_{NLTE}|$ is small for main-sequence stars (<0.11 dex), but can reach 0.32 dex in supergiants (Figs. 6c, 6d). In the supergiants, Δ_{NLTE} depends strongly on $T_{\rm eff}$, which could lead to a dispersion in the sodium abundances of the order of 0.2 dex if deviations from LTE are not taken into account, even in samples of stars with comparatively uniform values of effective temperature and luminosity.

The non-LTE corrections for the λλ568.2, 568.8, λλ588.9, 589.5, and λλ818.3, 819.5 nm Na I lines have a common property: the corrections grow with $T_{\rm eff}$, reach a maximum at some $T_{\rm max}$ that is higher the stronger the line, then decrease, and grow again at large $T_{\rm eff}$.

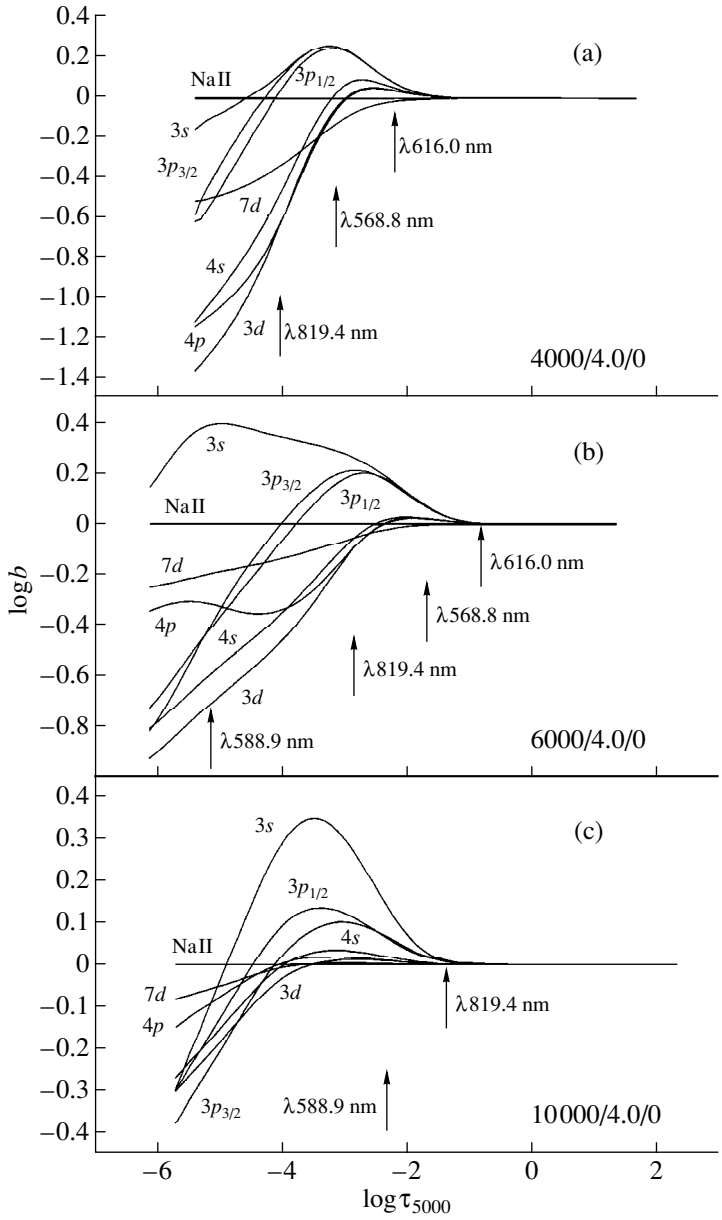

Fig. 4. Behavior of the *b* factors for individual Na I levels with depth for model atmospheres with various effective temperatures. The parameters of the model atmospheres $T_{\rm eff}/\log g$ /[A] are shown on the plots. The arrows mark the depths of formation of the radiation in the cores of important lines.

This behavior results from the simultaneous action of several factors:

(1) deviations in the populations of energy levels grow with $T_{\rm eff}$ due to the strengthening of radiative processes;

(2) in the interval from 4000 K to its $T_{\rm max}$, each of the lines is located on the curve of growth in sections of saturation or damping, and makes a transition to a linear section at higher temperatures;

(3) the Na I lines weaken with increase in $T_{\rm eff}$ and the depth of their formation shifts to deeper layers.

When $T_{\rm eff} < T_{\rm max}$, the first two of these factors lead to a rapid growth in the non-LTE corrections, but further, the transition of the lines to the linear section of the curve of growth and the action of the third factor decrease the corrections. Finally, at high $T_{\rm eff}$, when the lines are very weak, the first factor begins to dominate over the third, and the non-LTE corrections again grow.

The λλ588.9, 589.5 nm resonance lines are primarily used to determine the abundances of metal-deficient stars. In spite of the appreciable weakening of the lines in this case, deviations from LTE are as large as in stars with normal metallicity (Figs. 5a, 5b). At $T_{\rm eff} \geq$

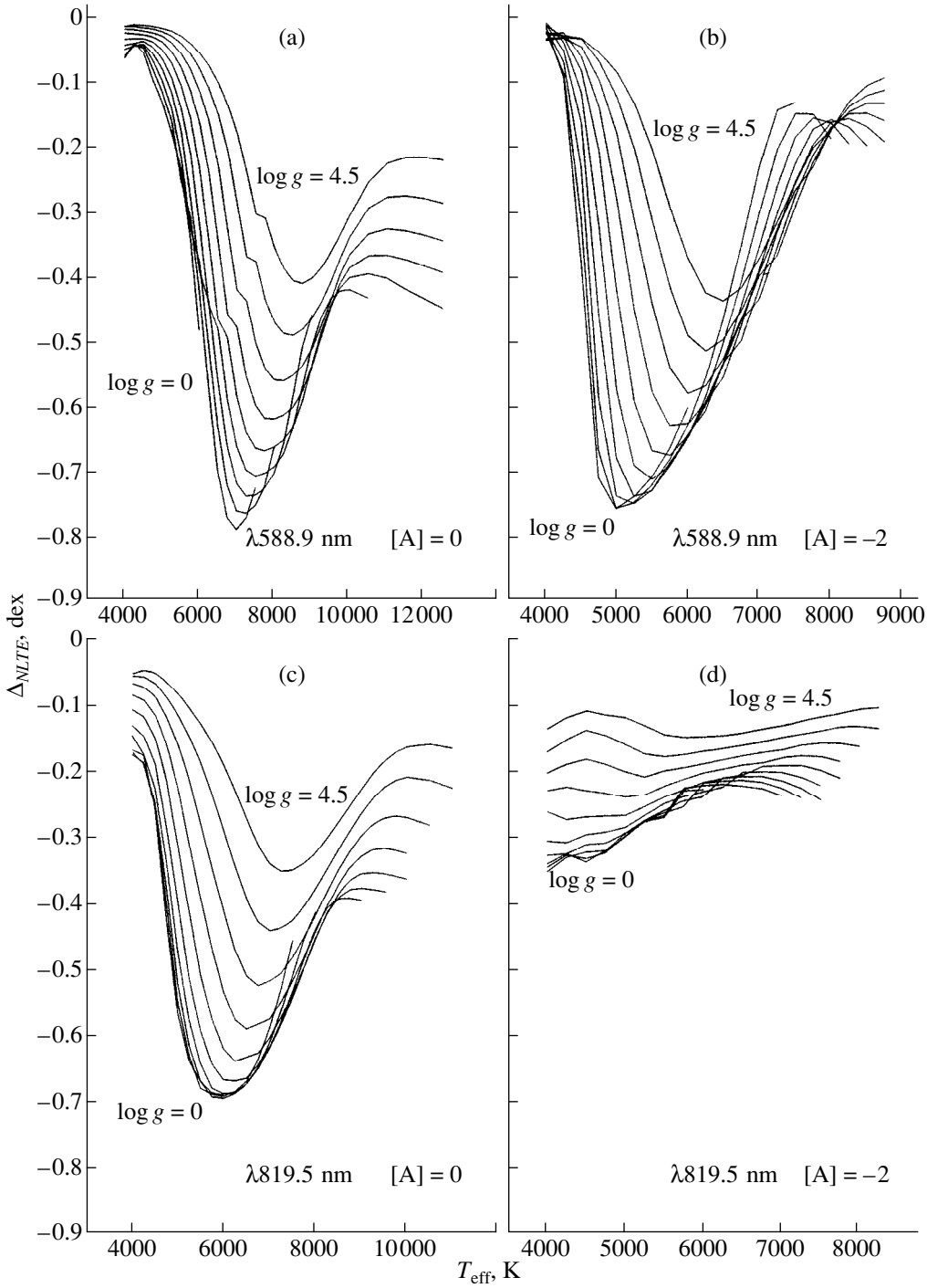

Fig. 5. Non-LTE corrections to the sodium abundance for the strongest Na I lines as functions of effective temperature, surface gravity, and heavy-element content.

5000 K, even the non-LTE corrections for main-sequence stars exceed 0.1 dex, and can reach 0.5 dex when $T_{\rm eff}$ = 6000–6500 K. The resonance lines are not used for stars with normal metallicity, due to the problems of taking into account the interstellar component, deviations from LTE, and pressure broadening. Our experience analyzing the solar spectrum (Section 3) shows that the theoretical description of the resonance lines is currently fully satisfactory, and they can be used in sodium abundance determinations, if the problem of the interstellar component of these lines is solved.

In connection with the development of infrared detectors, the possibility arises of using the λλ818.3, 819.5 nm Na I doublet, which can be measured right up

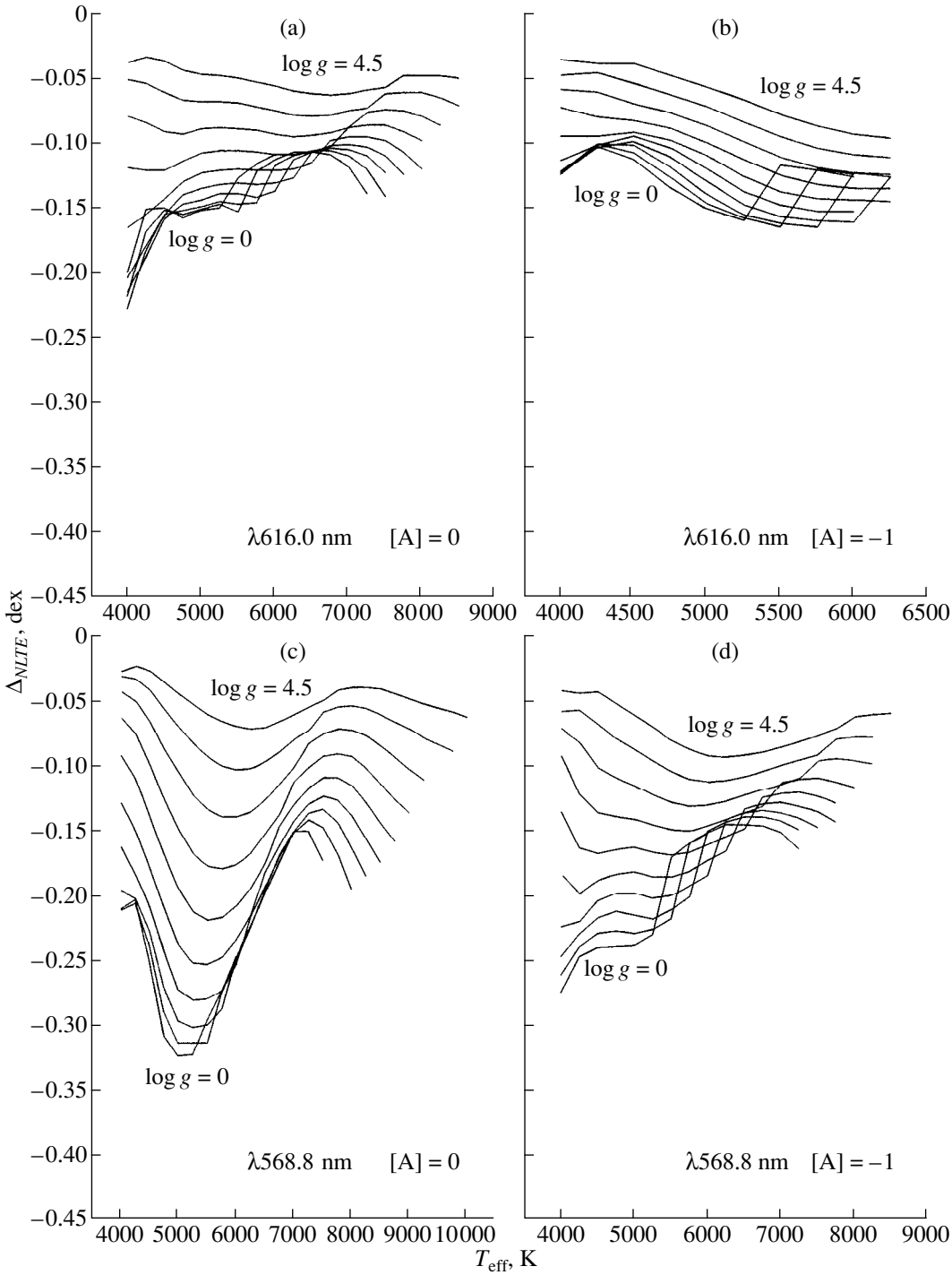

Fig. 6. Same as Fig. 5 for other Na I lines.

to $T_{\rm eff}$ = 10000 K (Figs. 5c, 5d), in sodium abundance analyses. However, when [A] ≥ –1, deviations from LTE for these lines are large—of the same order of magnitude as the resonance lines. Deviations from LTE are smaller for stars with larger deficits of heavy elements, but $|\Delta_{NLTE}| > 0.1$ dex over the whole range of parameters considered.

5. CONCLUSIONS

Our non-LTE computations for Na I carried out for a wide range of stellar parameters and our analysis of Na I lines in the solar spectrum lead us to draw the following conclusions.

(1) Fitting the line profiles observed in the solar spectrum with theoretical profiles enables the empirical

refinement of the van der Waals broadening constants C_6 and of the efficiency of inelastic collisions with H atoms in the statistical equilibrium of Na I.

(2) If individual corrections to the Unsold constant C_6 for each line and deviations from LTE are taken into account, it is possible to determine the solar sodium abundance with an accuracy better than 0.03 dex. Using the profiles of nine Na I lines, we obtained $\log\varepsilon_{Na} = 6.20 \pm 0.02$ using the solar model atmosphere of [10] and $\log\varepsilon_{Na} = 6.28 \pm 0.03$ using the HolMul model. This underlines the importance of using models calculated using a single method for both the comparison star and the stars under study in differential abundance determinations.

(3) The effect of "overrecombination" of Na I, found earlier for solar-type stars, occurs over the entire range of stellar parameters considered, and becomes stronger with growth of T_{eff} and luminosity. Na I lines are stronger than in the LTE case, and non-LTE corrections to the abundances are negative. Deviations from LTE can be neglected only for the λλ615.4, 616.0 nm doublet and only for main-sequence stars. In all other cases, the LTE sodium abundances are overestimated by 0.15–0.75 dex. Even in differential LTE abundance determinations, the achievement of high accuracy is hindered by the strong dependences of the non-LTE corrections on T_{eff}, $\log g$, and [A]. Therefore, it is desirable to conduct non-LTE calculations for individual stars with their specific parameters when deriving sodium abundances. This no longer entails a large amount of time. In our work, we have shown that a 20-level model of the Na I atom that includes the sublevels of the fine splitting of the 3*p* state is fully adequate to treat the statistical equilibrium of Na I over a wide range of stellar parameters. We will make available the results of our non-LTE computations for Na I to any interested persons. If computations for other values of T_{eff}, $\log g$, and [A] are required, please address your request to the authors.

ACKNOWLEDGMENTS

The authors thank R. Kurucz for presenting us with compact disks with tables of spectral lines and model atmospheres, and D. Ivanova for help in reducing the solar spectra. This work was partially supported by the Russian Foundation for Basic Research (project code 99-02-17488). L.I.M. thanks the International Soros Science Education Program (grant d97-24).

REFERENCES

1. P. A. Denisenkov, Astrofizika **31**, 588 (1989).
2. N. Prantzos, A. Coc, and J. P. Thibaud, Astrophys. J. **379**, 729 (1991).
3. Y. Takeda and M. Takada-Hidai, Publ. Astron. Soc. Jpn. **46**, 395 (TT-H) (1994).
4. J. H. Bruls, R. J. Rutten, and N. Shchukina, Astron. Astrophys. **265**, 237 (1992).
5. L. I. Mashonkina, N. A. Sakhibullin, and V. V. Shimanskiĭ, Astron. Zh. **70**, 372 (1993) [Astron. Rep. **37**, 192 (1993)].
6. Y. Takeda, Publ. Astron. Soc. Jpn. **47**, 463 (1995).
7. A. A. Boyarchuk, I. Hubeny, J. Kubät, *et al.*, Astrofizika **28**, 202 (1988).
8. J. Drake, Mon. Not. R. Astron. Soc. **251**, 369 (1991).
9. D. Baumuller, K. Butler, and T. Gehren, Astron. Astrophys. **338**, 637 (1998).
10. R. L. Kurucz, CD-Roms 1994.
11. D. G. Yakovlev, I. M. Band, M. B. Trzhaskovskaya, and D. A. Verner, Astron. Astrophys. **237**, 267 (1990).
12. D. Hofsaess, At. Data Nucl. Data Tables **24**, 285 (1979).
13. W. L. Wiese, M. W. Smith, and B. M. Miles, *Atomic Transition Probabilities*, Vol. II, NSRDS-NBS 22, 1969.
14. E. Biemont, Astron. Astrophys., Suppl. Ser. **31**, 285 (1978).
15. D. Norcross, J. Phys. B. Molecul. Phys. **4**, 1458 (1971).
16. N. A. Sakhibullin, Tr. Kazan. Gor. Astron. Obs. **48**, 9 (1983).
17. L. H. Auer and J. Heasley, Astrophys. J. **205**, 165 (1976).
18. Th. Gehren, Astron. Astrophys. **237**, 267 (1975).
19. G. W. Curtis and J. T. Jefferies, Astrophys. J. **150**, 1061 (1967).
20. A. McWilliam, G. W. Preston, Ch. Sneden, and L. Searle, Astron. J. **109**, 2757 (1995).
21. R. L. Kurucz, Astrophys. J., Suppl. Ser. **40**, 1 (1979).
22. W. Steenbock and H. Holweger, Astron. Astrophys. **130**, 319 (1984).
23. R. L. Kurucz, I. Furenlid, J. Brault, and L. Testerman, *Solar Flux Atlas from 296 to 1300 nm* (Natl. Solar Obs., Sunspot, 1984).
24. H. Holweger and E. Muller, Sol. Phys. **39**, 19 (1974).
25. P. Maltby, E. H. Avrett, M. Carlsson, *et al.*, Astrophys. J. **306**, 284 (1986).
26. G. Deridder and W. van Rensbergen, Astron. Astrophys., Suppl. Ser. **23**, 147 (1976).
27. W. Fullerton and Ch. R. Cowley, Astrophys. J. **165**, 643 (1971).
28. A. Unsold, in *Physik der Sternatmospheren* (Springer, Berlin, 1955, 2nd ed.).
29. N. Grevesse, A. Noels, and A. J. Sauval, Astron. Soc. Pac. Conf. Ser. **99**, 117 (1996).
30. D. L. Lambert and B. Warner, Mon. Not. R. Astron. Soc. **138**, 181 (1968).

Translated by D. Gabuzda

Astronomy Reports, Vol. 44, No. 12, 2000, pp. 804–814. Translated from Astronomicheskiĭ Zhurnal, Vol. 77, No. 12, 2000, pp. 909–921.

The Quiescent X-ray Emission of X-ray Novae and the Coronal Emission of Late-Type Stars

M. M. Katsova and A. M. Cherepashchuk

Sternberg Astronomical Institute, Universitetskiĭ pr. 13, Moscow, 119899 Russia

Received December 10, 1999

Abstract—The X-ray luminosities and spectra of F–M stars of luminosity classes IV–V are analyzed. In dwarfs with rotational velocities of about 100 km/s, such as the optical components of low-mass X-ray novae with black holes, hot plasma can be confined in coronal loops even in the presence of fairly weak magnetic fields. Thus, the soft X-ray emission of such systems in their quiescent state (to 10^{31} erg/s) could be associated with the coronal emission of the optical component/dwarf. Two systems studied with subgiants (V1033 Sco and V404 Cyg) have X-ray luminosities 2×10^{32}–2×10^{33} erg/s. The X-ray emission of a solar-type corona cannot provide such luminosities. However, a transition to a non-solar corona is possible in rapidly rotating subgiants—a dynamical corona whose X-ray emission can be one to two orders of magnitude higher than observed for more slowly rotating late-type subgiants in the solar neighborhood. This suggests that the quiescent X-ray emission of these two systems is provided by emission from the corona of the subgiant optical component. © *2000 MAIK "Nauka/Interperiodica".*

1. INTRODUCTION

X-ray novae are well-studied transient sources of X-ray emission and members of a wide class of low-mass X-ray binaries (see, for example, [1, 2] and references therein). An X-ray nova consists of a low-mass optical star ($\leq 2\ M_\odot$) of spectral type A–M and luminosity class IV–V that fills its Roche lobe, and a relativistic object (neutron star or black hole) surrounded by a disk of material flowing from its companion. Most X-ray novae are transient sources of soft X-ray emission (their X-ray spectrum in the active stage has a bremsstrahlung temperature $kT_{brem} \leq 15$ keV), although a number (such as GRS 1716–249, GS 2023+33, and GRO J0422+32) with purely power-law spectra (without any excess at soft X-rays) were recently discovered (see, for example [3]).

The most important distinguishing property of X-ray novae is that, once every several years, the X-ray luminosity of these close binary systems increases by many orders of magnitude (by a factor of 10^2 to 10^6) for several days and then, in the most cases, drops exponentially over several tens of days. The corresponding X-ray burst is followed by an optical burst, due to heating of the optical star and accretion disk by the powerful X-ray radiation. The X-ray luminosity at the burst maximum can be as large as 10^{37}–10^{38} erg/s.

On the other hand, the X-ray luminosity of X-ray novae in their quiescent state is very low, $\approx 10^{30}$–10^{33} erg/s. In such periods, the optical spectrum of the system exhibits the absorption lines of the A–M star, as well as intense, broad hydrogen and helium lines produced by the accretion disk. The undoubted presence of an accretion disk around the relativistic object and evidence for flows from the optical A–M star through the inner Lagrange point in the presence of very low X-ray luminosities in the quiescent state represent a fundamental enigma about X-ray novae (see, for example, the reviews [4, 5] and references therein).

To explain the anomalously low X-ray luminosity of X-ray novae in the quiescent state, a model with an advection-dominated, quasi-spherical accretion flow onto the black hole was put forward [6–8]. In this model, a two-temperature plasma with low optical depth is formed in the inner regions of the accretion disk. Due to the action of viscosity during accretion, the thermal energy released by dissipation is primarily accumulated in hot protons and ions, whose temperature is several billion Kelvin. Since the characteristic time for the transfer of energy from hot protons and ions to electrons via Coulomb interactions is comparatively large, most of the thermal energy is transferred to the black hole by the advection flows; this means that the thermal energy released in the process of accretion cannot escape into space. This mechanism could explain the anomalously low luminosity of X-ray binaries in their quiescent state.

However, advection-dominated accretion models have recently come under severe criticism. As was shown in [9, 10], allowance for Ohmic dissipation considerably increases the efficiency of the transformation of thermal energy into radiation compared to the case of advection-dominated accretion (where the energy of hot ions is transferred to electrons only via Coulomb interactions). The possibility of evaporation of inner parts of an advection-dominated disk in the form of a wind was considered in [11]. This leads to a substantial decrease in the rate of accreting matter onto the relativ-

1063-7729/00/4412-0804$20.00

Table 1. Some properties of X-ray novae

No.	Source	Star	P_{orb}, days	m_x, $M_\odot$	m_v, $M_\odot$	A, $R_\odot$	$v \sin i$, km/s
1	J0422+32	V518 Per	0.2	10	0.4	3.15	90^{+22}_{-27}
2	A0620–003	V616 Mon	0.3	10	0.6	4.15	83 ± 5
3	1009–45	MM Vel	0.3	3.6–4.7	0.5–0.7	3.17	
4	1124–684	GU Mus	0.4	6	0.8	4.33	106 ± 13
5	J1655–40	V1033 Sco	2.6	7	2.5	16.87	82.9–94.9
6	1705–250	V2107 Oph	0.5	6	0.4	4.93	
7	2000+251	QZ Vul	0.3	10	0.5	4.13	
8	2023+338	V404 Cyg	6.5	12	0.7	34.24	39.1 ± 1.2
9	1543–475	HL Lup	1.1	5	2.5	8.79	

istic object and, accordingly, to an appreciable decrease in the energy released by accretion. A similar idea was put forward by Bisnovatyĭ-Kogan [10], who suggested that the reason for the anomalously low luminosities of quiescent X-ray novae, and also of many galactic nuclei, is precisely a low accretion rate onto the central relativistic object due to the fact that most of the accreting matter is carried away in the form of relativistic jets and a spherically-symmetric wind.

To understand the nature of quiescent X-ray novae, we must know their X-ray luminosity and spectra. Because of the extremely low expected X-ray luminosity, this difficult and important observational problem began to be resolved only recently, using the new generation of X-ray satellites. In particular, new 0.5–10 keV X-ray observations by *ASCA* [12] have enabled studies of the X-ray luminosities and spectra of 13 X-ray novae in their quiescent states. These include four X-ray novae with neutron stars, six with black holes, and three that probably have black holes. All available data on the X-ray luminosities of quiescent X-ray novae have been compiled, for example, in the reviews [5, 13]. The launch of new, highly-efficient X-ray satellites such as *CHANDRA*, *XMM*, etc. will make it possible to study many of these objects in detail.

To correctly interpret the X-ray luminosities and spectra of quiescent X-ray novae, the contribution of the X-ray coronal emission of the optical component in the close binary system (i.e., A–M stars) must be taken into account. Measurements of the masses of black holes in nine X-ray novae and of neutron stars in two X-ray novae are currently available. Since the optical component fills its Roche lobe, its radius can be easily calculated if the masses of the relativistic object and the optical component are both known. Further, we can calculate the bolometric luminosity if the spectral type is known. Finally, using the extensive X-ray observational material for late-type stars (see, for example, [14–16]), we can estimate the characteristics of the X-ray emission of the optical star in each of the close binaries studied and take into account this emission when analyzing the data for X-ray novae.

The aim of this paper is to classify and analyze X-ray data for the coronas of late-type (F–M) stars, for subsequent use in estimates of the luminosities and spectra of quiescent X-ray novae.

2. PARAMETERS OF KNOWN X-RAY NOVAE WITH BLACK HOLES

The properties of the optical components of X-ray novae (i.e., A–M stars) are best studied for the quiescent state of low-mass binary systems with black holes. Characteristics of such systems adopted from [5] and their axial-rotation velocities are presented in Table 1. Since the optical components of these binary systems fill their Roche lobes, and estimates of the masses for both components are available, we can calculate the optical stars' radii using Kepler's third law and an approximation for the average radius of the Roche lobe of an optical star for $q = \frac{m_x}{m_v} \geq 1$ (see, for example, [17]):

$$\frac{r_v}{A} = \frac{0.49q^{-2/3}}{0.6q^{-2/3} + \ln(1 + q^{-1/3})},$$

where A is determined by the relation

$$\frac{A^3}{P^2} = \frac{G}{4\pi^2}(m_x + m_v).$$

Here, A is the semimajor axis of the orbit in centimeters, P is the orbital period in seconds, and m is the component mass in grams.

Effective temperatures were estimated from the spectral and luminosity classes of the stars (see, for example, [18]). Table 2 presents the average radii R_* for a given spectral type, effective temperatures, and Roche-lobe sizes r_{Roche} for the optical components, together with their bolometric luminosities calculated from the formula $L_{\text{bol}} = 4\pi r_{\text{Roche}}^2 \sigma T_{\text{eff}}^4$. The calculated K–M-star radii and the bolometric luminosities are in agreement with the data for flare stars and related

Table 2. Some properties of the optical components of X-ray novae

No.	Star	Spectrum	$T_{\rm eff}$, K	$R^*, R_\odot$	$r_{\rm Roche}, R_\odot$	$L_{\rm bol}$, erg/s
1	V518 Per	M2V	3500	0.5	0.50	1.29×10^{32}
2	V616 Mon	K4V	4600	0.8	0.74	8.41×10^{32}
3	MM Vel	(K6–M0)V	4000	0.7	0.73	4.71×10^{32}
4	GU Mus	K5V	4300	0.7	0.97	1.12×10^{33}
5	V1033 Sco	F5IV	6500	2.0	4.96	1.52×10^{34}
6	V2107 Oph	K(3–7)V	4300	0.75	0.90	9.65×10^{32}
7	QZ Vul	K5V	4300	0.7	0.70	5.63×10^{32}
8	V404 Cyg	K0IV	4900	3.0	6.04	7.25×10^{34}
9	HL Lup	A2V	9150	2.0	2.82	1.92×10^{35}

objects in the solar neighborhood of Gershberg *et al.* [19]. Figure 1 shows the position of these stars in the Hertzsprung–Russell diagram. We can see that, in most cases, the positions for the optical companions in low-mass X-ray novae deviate from those for main-sequence stars. The optical components of X-ray novae with black holes have radii and luminosities that are high for their masses. This implies that they have undergone longer evolution compared to normal main-sequence stars, in agreement with the results of [20].

The high axial-rotation velocities ($v \sin i$ = 40–100 km/s) that are typical of the late-type components of these binaries indicate conditions suitable for the development of solar-type surface activity. The basic indicators of stellar activity are emission in the Balmer lines and the H and K lines of CaII, EUV emission from the transition region between the chromosphere and corona of the optical component, and absorption lines of lithium. However, since quiescent X-ray novae are very weak in the optical, data on most of these spectral features are unavailable. There is only some evidence for narrow (half-width ≈146 km/s) weak H_α emission for the F5IV component of the X-ray nova GRO J1655–40. This narrow H_α emission (equivalent width $\approx 10 \pm 0.5$ Å) was detected in May 1998 [21], when the system was in its most quiescent state; normally, the hydrogen absorption lines in the spectrum of the optical star in a quiescent X-ray nova are swamped by the powerful, broad (≈2000 km/s), two-peaked emission produced in the accretion disk around the black hole.

We should also note the presence of enhanced lithium absorption in the spectra of the optical components (see, for example, [5]). The enhanced lithium abundance is usually interpreted as evidence that lithium is ejected from the inner parts of the accretion disk, where nucleosynthesis reactions are assumed to take place during flaring of X-ray novae [22]. On the other hand, this lithium line could also be associated with active processes in late-type stars. This requires that some accelerated particles with moderate energies (for example, α particles with $E > 30$ MeV) enter the lower chromosphere or upper photosphere of the cold star. In principle, such particles can be accelerated both in the course of prolonged flares in the late-type star and in the relativistic object. The problem of lithium generation in reactions initiated by the penetration of accelerated particles has recently been considered afresh, in connection with the detection of γ emission and the first observation of an enhancement of the lithium line during a flare in a red dwarf [23, 24]. Therefore, we can reasonably assume that the lithium absorption in some of the systems under consideration could be associated with processes in the late-type star, especially in systems where this component is a subgiant.

Thus, the optical components of low-mass X-ray novae have the same properties as ordinary isolated A–M stars (though they experience longer evolutions than main-sequence stars), although they are rapidly rotating and, despite their appreciable ages, probably possess an increased level of chromospheric and coronal activity.

3. X-RAY EMISSION OF LATE-TYPE STARS

3.1. X-ray Luminosity of Active Late-Type Stars

The properties of the X-ray emission of low-mass, late-type stars similar to the optical components of X-ray novae are quite well established. The amplitude of the X-ray flux emitted by the hot corona of an active late-type star is determined primarily by the velocity of its axial rotation. In binary systems, where the axial rotation of the stars is supported by the interaction between their own and the orbital momenta, the stage of activity persists considerably longer than in isolated stars. Let us consider the X-ray data for late-type main-sequence stars and subgiants.

The *ROSAT* satellite in its full-sky survey mode has conducted extensive X-ray observations at 0.1–2.4 keV of approximately 1500 late-type stars located at distances of up to several hundred parsecs from the Sun [14–16]. Figure 2 presents the X-ray luminosities of approximately 1000 of the nearest late-type stars. Most of these stars are on the main sequence, and only a few subgiants are included in the catalog [14]. Note that the

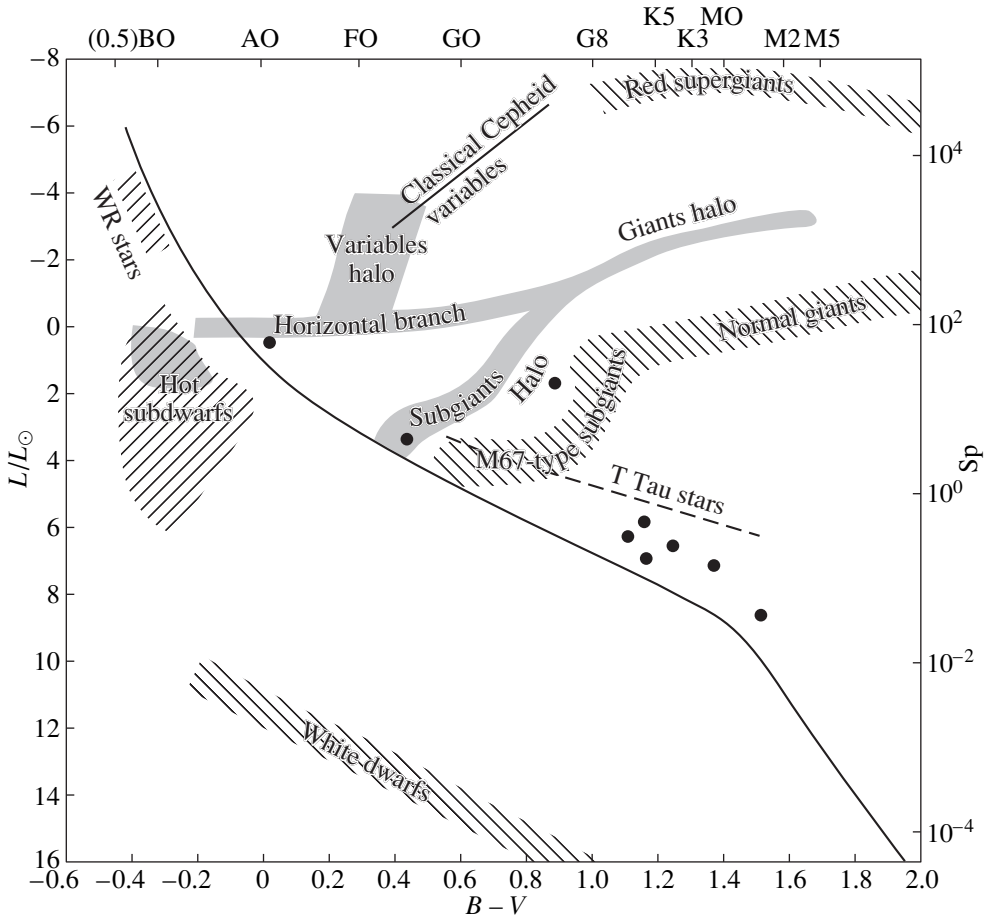

Fig. 1. Positions (dots) of the optical components of low-mass X-ray novae with black holes in the Hertzsprung–Russel diagram.

X-ray luminosities of subgiants are somewhat greater than 10^{30} erg/s, whereas, as a rule, the X-ray luminosities of even the most active late-type, quiescent main-sequence stars are below this level.

The dependence of the X-ray emission of stellar coronas on axial-rotation velocity can be traced for active late-type stars of various spectral types and luminosity classes. For example, the Sun (G(2–4)V) rotates with velocity 2 km/s at the equator, and the soft X-ray emission of its corona at the maximum of its cycle reaches 3×10^{27} erg/s. A dependence of the form $L_x \propto v_{\mathrm{rot}}^2$ was found for lower main-sequence stars, whereas the dependence becomes weaker for stars of higher luminosity classes.

The general variation of X-ray luminosity with spectral type for F5–M stars is in agreement with current theoretical concepts about the formation of stellar coronas via the interaction between convection and axial rotation. The strong depression of X-ray emission for most red dwarfs (with color index $B - V \geq 1.5$) is associated with the transition to completely convective stars. We should emphasize that the main source of X-ray emission from lower-branch stars is emission by

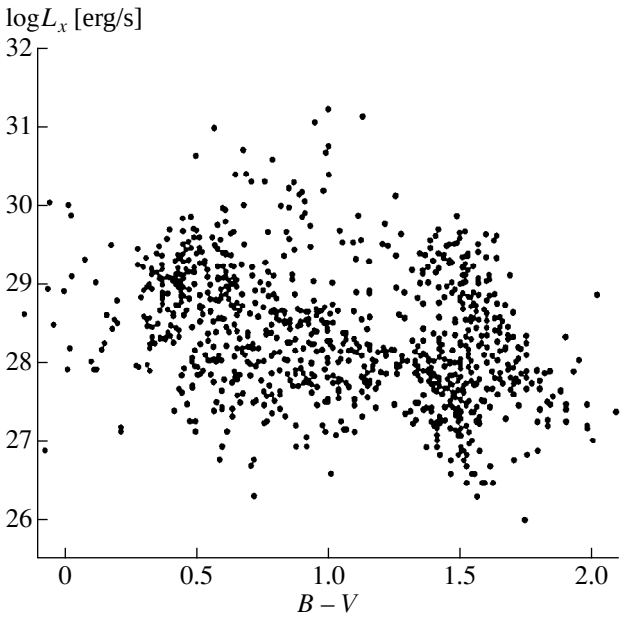

Fig. 2. X-ray luminosities of the nearest late-type stars observed by *ROSAT* in full-sky survey mode at 0.1–2.4 keV [14].

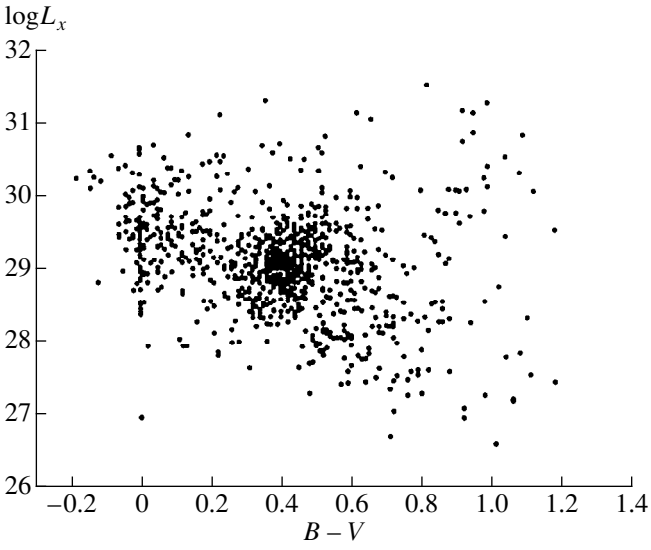

Fig. 3. X-ray luminosities of bright main-sequence stars and subgiants observed by *ROSAT* in full-sky survey mode at 0.1–2.4 keV [15].

hot plasma trapped in coronal loops (i.e., magnetic-field tubes). These loops are concentrated primarily in active regions and cover a considerable fraction of the volume of the lower coronal layers. Such loops represent equilibrium MHD configurations, where the gravitational force is balanced by magnetic forces, and the slow heating of the plasma is equal to its radiative cooling.

A second branch of stars with increased X-ray emission, active red dwarfs with $B-V \geq 1.3$, can be traced in Fig. 2. Most of these stars are flare variables, and are included in the catalog of UV Cet stars and related objects [19]. Additional heating of the coronas of these stars and, consequently, enhanced X-ray emission could be the result of multiple weak flares.

In this context, it is important that the X-ray luminosity of the coronas of all late-type dwarfs in the quiescent state cannot exceed $10^{-3}L_{\rm bol}$. This follows from the saturation of X-ray fluxes found by Vilhu and Walter [25], which occurs when the entire coronal volume is filled by the loops. Therefore, since we do not know the level of activity for the late-type stars in low-mass X-ray binaries but their rapid rotation is evident, we shall use this maximum value to estimate their X-ray luminosity.

ROSAT X-ray data for late-type F, G, and K subgiants [15] are presented in Fig. 3. We can see that the maximum X-ray luminosities of the subgiants are below 10^{31} erg/s. Note that the ratio $L_x/L_{\rm bol}$ is lower for late-type stars with increased luminosity than the corresponding value for dwarfs, 10^{-3}. This is evident in Fig. 4, which presents ratios of the X-ray to bolometric fluxes $F_x/F_{\rm bol}$ for late-type giants and supergiants for the *ROSAT* data [16], which do not exceed 10^{-4}.

Let us discuss the situation when a late-type main-sequence star is in a close binary system of the type considered. Since such stars possess rather large velocities of axial rotation (up to 40–100 km/s), this should inevitably manifest a whole range of solar-type activity. At the same time, the star fills its Roche lobe. As a result, its photosphere flows out with velocity 50–100 km/s at the equator, and the influence of the gravitational force in the outer atmosphere is decreased. However, since the feet of the magnetic tubes forming the corona are anchored in subphotospheric layers, the hot plasma remains trapped in the loops. On the other hand, the matter located between loops (the so-called background corona) will flow outwards.

The theory of the coronas of active late-type stars is based on analogies with the structure of the solar

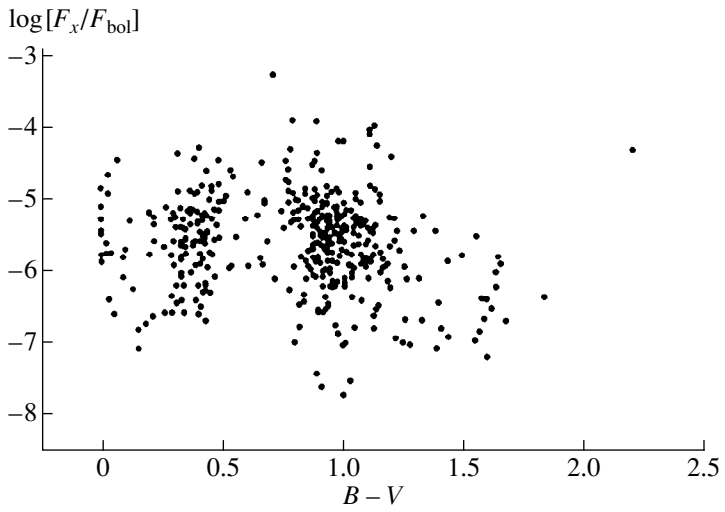

Fig. 4. Ratios of X-ray to bolometric fluxes for late-type stars with enhanced luminosity (giants and supergiants) from *ROSAT* data [16].

corona. The transition from dwarfs to subgiants and giants is accompanied by increases in the scales of coronal structures and the characteristic times for nonstationary processes. However, coronas with very small gravitational forces have not yet been investigated theoretically, and we can express only some general ideas here.

First, if a late-type main-sequence star with a convective zone rotates rapidly, activity phenomena should efficiently develop in its outer atmosphere. If such a star is a component of an X-ray nova, decreasing the gravitational force in the star's coronal layers (due to the gravitational action of the relativistic object) will strengthen the dynamic processes accompanying the evaporation of a considerable mass of gas from the chromosphere to the coronal parts of the tubes. Precisely this process is responsible for the formation of the corona; i.e., loops filled with hot plasma.

One serious problem for ordinary active late-type stars associated with a relativistic object is trapping the coronal gas. If there is a substantial decrease in the gravitational force above the photosphere, particles will be separated from the star not only by the gas pressure gradient in the hot corona, but also by the rapid rotation of these layers. Since the feet of thin magnetic tubes are anchored beneath the photosphere, coronal plasma will be trapped in the upper parts of these loops. The structure and intensity of the magnetic field must support this process.

The magnetic-field intensity required to trap the plasma in the corona of a rapidly rotating star can be estimated from the equilibrium condition for the plasma configuration. Since the magnetic-field structure in stellar coronal loops is unknown, let us consider some plasma cloud in the corona, in which the magnetic force is balanced by the gravitational and centrifugal forces. The equilibrium condition for this MHD configuration can be written using the equation of motion. For example, based on Eq. (23.5) from [26], when radial motions are absent, we have for the projection in the radial direction

$$-\frac{1}{4\pi}[\mathrm{curl}\mathbf{H}\cdot\mathbf{H}]\Big|_r = -\frac{dp}{dr} - \rho\frac{GM_*}{r^2} + \rho\frac{v_\varphi^2}{r}, \qquad (1)$$

where H is the magnetic-field intensity in the corona, p the gas pressure, which slowly decreases outwards, ρ the plasma density, $g(r) = GM_*/r^2$ the free-fall acceleration, and $v = v_\varphi$ the rotational velocity of the star at a distance r from its center (we consider here only the equatorial regions).

The physical conditions in the coronas of late-type stars are approximately hydrostatic, so that the first two terms nearly balance each other. If we assume that the density in an isothermal corona changes in accordance with a hydrostatic law, i.e.,

$$\rho = \rho_0\exp\left(-\frac{r-r_*}{h_0}\right),$$

where $h_0 = 2kT/m_pg$, we then obtain for the hydrogen plasma

$$-\frac{1}{4\pi\rho}[\mathrm{curl}\mathbf{H}\cdot\mathbf{H}]\Big|_r = \frac{v^2}{r}. \qquad (2)$$

To order of magnitude, $[\mathrm{curl}\mathbf{H}\cdot\mathbf{H}] = H^2/\zeta$. The physical meaning of the quantity ζ will become clear if we consider a semicircular magnetic-field line (in the meridional plane) and calculate $[\mathrm{curl}\mathbf{H}\cdot\mathbf{H}]$ in cylindrical coordinates. We then obtain $\frac{1}{H^2}[\mathrm{curl}\mathbf{H}\cdot\mathbf{H}] = -1/\zeta$, where ζ is the radius of the semicircle. From the physical point of view, this is a case when the magnetic pressure varies quite slowly, and the magnetic force is associated with curvature of the magnetic-field lines ($1/\zeta$), whose ends are anchored in the photosphere.

Finally, we find

$$V_A^2 = \frac{H^2}{4\pi\rho} = \frac{4\pi^2}{P^2}r(r-r_*), \qquad (3)$$

where V_A is the Alfvén velocity, the velocity of axial rotation is expressed in terms of the orbital period P, and $\zeta = r - r_*$. (All quantities refer to the apex of the field line under consideration.)

If we assume that the loop apex is at a height $r - r_* = 0.2r_*$ from the limb, then we will have for the *V*518 Per system, with a period of $P = 0.2$ days, $V_A = 44.1$ km/s. For a plasma density $n_e = 10^9$ cm^{-3} at the coronal point under consideration, the magnetic-field intensity H is 0.64 G. The magnetic-field intensity in the solar corona at height $0.2R_\odot$ over the limb is approximately 1 G [27].

Taking into account the real structure of the magnetic field inside the coronal loops that are sources of soft X-ray emission could change this estimate slightly. In addition, if the magnetic-field intensity is sufficiently close to this value, the influence of MHD instabilities could disrupt the loops and eject plasma outwards. In plasma confinement under laboratory conditions, as well as in solar prominences, the interchange (flute-like) instability often develops; this is a type of Rayleigh–Taylor instability in which the plasma and magnetic field interchange places. Therefore, in the case of axial-rotation velocities for late-type stars of about 100 km/s, the plasma will be trapped inside coronal loops if the magnetic-field intensity is 1–10 G. Such magnetic fields are quite reasonable for the lower coronas of active late-type stars. It is plausible that the X-ray emission of systems with dwarf optical components is emission from their coronas.

Thus, a given binary system with a specified magnetic-field intensity in the corona has a critical axial-rotation velocity, up to which the plasma remains trapped in closed coronal loops. As the plasma reaches or exceeds this critical velocity, some loops will be disrupted, and plasma will be ejected outwards. This process should be more powerful and the ejected plasma

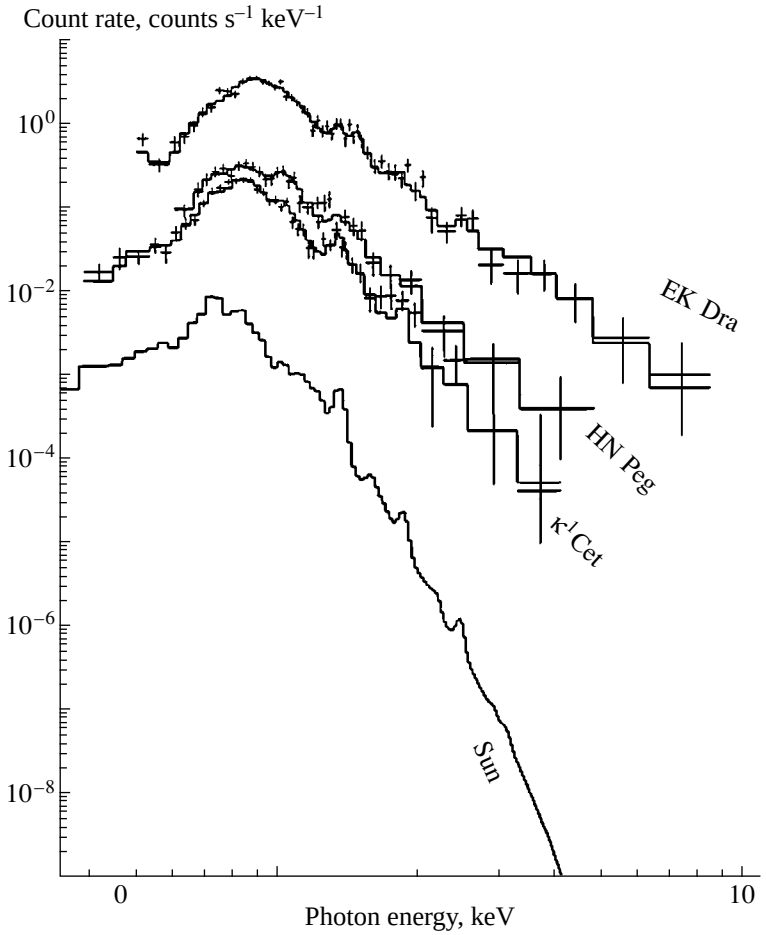

Fig. 5. X-ray spectra for three G stars with various ages detected by SISO on *ASCA*. The average solar spectrum without flares was reconstructed for the spectral characteristics of this device (from the data of [29]).

more dense and hot than in the case of solar coronal mass ejections. This implies that the type of stellar corona will change at stellar axial-rotation velocities exceeding the critical value: a solar-type corona will be replaced by a dynamical one, as described theoretically in [28]. The more powerful and multiple ejections of coronal material will produce a large-scale shock wave over a large fraction of the stellar surface. This could increase the power of the X-ray emission by several orders of magnitude and make its spectrum harder. This provides a way to explain the properties of the X-ray emission of the two analyzed X-ray novae whose optical components are late-type subgiants.

3.2. X-ray Spectra of Active Late-Type Stars

At present, the spectral distribution of the soft X-ray emission of active late-type stars is known quite well.

First, the hardness of this emission depends on the age of the stars. For example, variations in the X-ray spectra of solar-type stars were followed using *ROSAT* and *ASCA* data in [29]. As an example, the *ASCA* X-ray spectra for three G stars with different ages and for the Sun [29] are presented in Fig. 5. All fluxes have been reduced to the same distance, 10 pc. The age of EK Dra is 70 million years, of HN Peg is 300 million years, and of κ^1 Cet is 750 million years. We can see that the X-ray spectrum becomes flatter, the spectral maximum gradually shifts from 0.7 to 0.9 keV, and the X-ray luminosity (reduced to the distance 10 pc) increases when we consider first the Sun and then increasingly active G stars. Physically, this implies a gradual appearance of hotter plasma with temperature $T_2 \approx (5–7) \times 10^6$ K (along with usual coronal gas with temperature $T_1 = (1–2) \times 10^6$ K) in the coronas of young G stars.

Second, it has been established that high-temperature regions appear in the coronas of rapidly rotating stars. More rapid axial rotation of a late-type star is followed by the development of a dense and hot corona. The reasons leading to the increase in the rotational velocity are not important here: they can be associated with the age of the star or with binarity. Note that the stage of activity is longer for late-type stars in binary systems.

Third, red dwarfs with the lowest masses are characterized by high flare activity. Heating of their coronas

Table 3. X-ray luminosities of the optical components of low-mass quiescent X-ray novae: observed *ASCA* L_x at 0.5–10 keV and optimistic estimates of L_x at 0.1–2.4 keV

No.	Star	Spectrum	$B-V$	L_{bol}, erg/s	L_x, erg/s	L_x (*ASCA*), erg/s
1	V518 Per	M2 V	1.51	1.294×10^{32}	$(1–2)\times10^{30}$	–
2	V616 Mon	K4 V	1.11	8.466×10^{32}	$(1–2)\times10^{30}$	2×10^{30}
3	MM Vel	K6–M0 V	1.39	4.709×10^{32}	10^{30}	–
4	GU Mus	K5 V	1.18	1.334×10^{33}	$(1–2)\times10^{30}$	$<(4–7)\times10^{30}$
5	V1033 Sco	F5 IV	0.42	1.485×10^{34}	$(2–4)\times10^{31}$	2×10^{32}
6	V2107 Oph	K3–7 V	1.25	9.768×10^{32}	$(1–2)\times10^{30}$	$<(6–10)\times10^{32}$
7	QZ Vul	K5 V	1.18	5.781×10^{32}	10^{30}	$<(2–3)\times10^{31}$
8	V404 Cyg	K0 IV	0.94	7.25×10^{34}	$(2–4)\times10^{31}$	2×10^{33}
9	HL Lup	A2 V	0.05	1.936×10^{35}	5×10^{30}	$<(4–5)\times10^{30}$

by multiple weak flares increases the level of X-ray emission. This is associated both with increased plasma density in coronal loops and with the formation of small, hot regions with temperature $T_3 = (10–20)\times10^6$ K in these stellar coronas. We should emphasize that these hot regions exist in the coronas of some active late-type components in RS CVn binaries. They could be associated with the development of prolonged flares or nonstationary processes.

To summarize, the shape of the X-ray spectra of the most active late-type stars in their quiescent state (i.e., without flares) changes only slightly in the range 0.1–10 keV. Although a blend of lines at 5.9 keV (of hydrogen- and helium-like iron FeXXV and FeXXVI) has been detected in the spectra of some such stars, their quiescent spectra are still soft, and do not extend beyond 10 keV.

4. X-RAY LUMINOSITIES AND SPECTRA OF QUIESCENT X-RAY BINARIES

Data on the soft X-ray emission of X-ray novae in their quiescent state are presented in Table 3. First and foremost, note that the observed X-ray luminosities of systems whose optical components are located near the main sequence do not exceed the maximum X-ray luminosities for active late-type stars. The X-ray luminosities of low-mass, quiescent X-ray binaries do not exceed about 10^{31} erg/s, and this level of X-ray emission can be produced by the coronas of the most active late-type dwarfs. Late-type stars of the spectral classes typical of the optical components of these systems—from late K to early M—possess the most favorable conditions for the formation of dense, hot coronas. This problem began to be studied using data from the *Einstein* X-ray observatory, with the discovery of maximum electron densities for stellar coronas with temperatures $(2–4)\times10^6$ K in stars of these spectral types [30]. Data from subsequent space instruments enabled identification of a second hot component of the coronal plasma, with $T \le 10^7$ K. Finally, a third component, associated with small coronal plasma structures with temperature $\le10^8$ K has recently been reliably identified. The X-ray spectra of quiescent X-ray novae whose optical components are late-type dwarfs should be similar to those observed for typical active K–M2 stars.

However, this does not apply to systems with higher X-ray luminosities ($L_x \approx 3\times10^{32}$ erg/s) and whose optical components are late-type subgiants. The available data for several dozen subgiants at distances below 100 pc show that their X-ray luminosity does not appreciably exceed 10^{31} erg/s (see, for example, [15]). This is characteristic of both isolated stars and the components of RS CVn binary systems.

The conclusions presented here can be illustrated by comparing the observed X-ray luminosities for the systems under consideration with the values for active stars of the same spectral type as the optical components of the X-ray novae. Table 3 presents the physical characteristics of the optical stars, their expected maximum X-ray luminosities at 0.1–2.4 keV at the corresponding axial-rotation velocities, and the *ASCA* values of L_x at 0.5–10 keV (see also Figs. 2–4). Since the optical components of X-ray novae rotate several times faster than the most active late-type dwarfs of the solar neighborhood, we can assume that their L_x values will be about a factor of two higher. On the other hand, it is evident that the estimated X-ray luminosities cannot appreciably exceed values corresponding to the Vilhu saturation [25]; i.e., they are limited to $L_x/L_{bol} \approx 10^{-3}$ for main-sequence stars and $L_x/L_{bol} \le 10^{-4}$ for subgiants.

Thus, a comparison of the observed and expected X-ray luminosities of X-ray novae in the quiescent state shows that their X-ray emission probably originates in the coronas of the optical components, when they are located near the main sequence. On the other hand, this is not true of the two systems involving subgiants—V1033 Sco and V404 Cyg. The differences of the X-ray luminosities for these two systems are approximately one and two orders of magnitude, respectively. This implies that emission from an ordinary solar-type corona is ≈10% of the observed X-ray luminosity in the first case and ≈1% in the second.

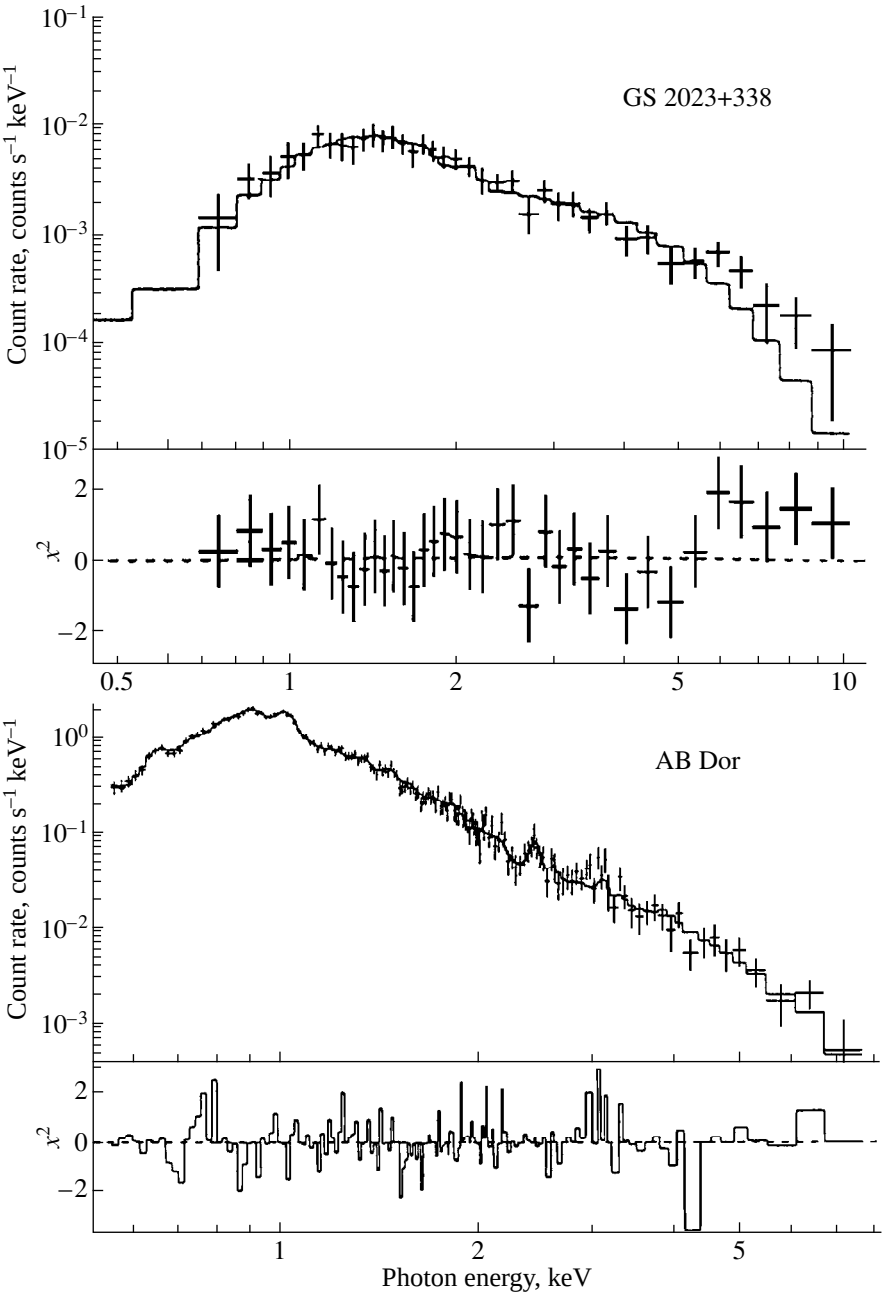

Fig. 6. Comparison of *ASCA* X-ray spectra for GS 2023+338 = V404 Cyg in the quiescent state and of the very active late-type star AB Dor [12, 32]. The spectrum of V404 Cyg is harder than that of AB Dor above 1 keV.

These conclusions are confirmed by analysis of the *ASCA* X-ray spectra of these two systems with subgiants [12]. A common feature in the spectra of low-mass X-ray novae, most RS CVn binaries, and most active, isolated, late-type stars is that the maximum of their emission is at $h\nu \approx 1$ keV (Fig. 6). This maximum is slightly shifted toward higher energy in the case of X-ray novae with subgiants, compared to young stars (Fig. 6), active RS CVn binaries (see, for example, the flareless spectrum of UX Ari obtained by *ASCA* [31]), and the most active isolated stars. The *ASCA* spectra of the V404 Cyg system and one of the most active late-type stars, AB Dor (K0IV–V) (for which data are taken from [32],) are compared in Fig. 6. The spectrum of the other system with a subgiant, V1033 Sco, is even harder in this energy range [12]. Nevertheless, we can assume that the X-ray spectra of low-mass X-ray novae whose optical components are late-type dwarfs will be similar to the spectra of late-type stars with high levels of activity.

The conclusion that low-mass X-ray novae with dwarfs and subgiants have different X-ray emission is also confirmed by a comparison of their spectra.

Namely, there are two maxima in the X-ray spectra of RS CVn binaries, corresponding to photon energies of about 0.2 and 1 keV. A second maximum is also present in the spectra of the two X-ray novae with subgiants, V1033 Sco and V404 Cyg [11]. Comparing the regions of the second maximum (Fig. 6), we can see that the maximum for V404 Cyg is slightly shifted toward harder energies, and the decrease in the X-ray emission is slower. In other words, this system possesses an excess of X-ray emission at 5–15 keV compared to ordinary active subgiants. Note also that a flat spectrum at 1–5 keV and, accordingly, an excess of emission near 5 keV are also present in V1033 Sco. Such excess X-ray emission (i.e., a power-law tail) at hard energies ($h\nu \geq 2$ keV) in systems with subgiants can naturally be explained as the emission of inflowing plasma in the accretion disk around the black hole [4, 5]. Note that the increased quiescent X-ray luminosity for the X-ray novae with subgiants (V1033 Sco and V404 Cyg) could reflect the fact that the subgiant, which fills its Roche lobe, loses mass through the inner Lagrange point at a considerably greater rate than a main-sequence star (in terms of the thermal time scale) [12]. This increases the accretion rate onto the black hole and, consequently, the X-ray luminosity.

The X-ray luminosities of X-ray novae with neutron stars are $\approx 10^{32}$–10^{33} erg/s [12]; i.e., at least an order of magnitude greater then the corresponding quantities for X-ray novae with black holes. Thus, in the case of X-ray novae with neutron stars, the contribution of X-ray emission from the coronas of the optical components at 0.1–2.4 keV will be less than 10%.

5. CONCLUSIONS

Although the A–M optical components of X-ray novae are old (ages of the order of 10^9 years), they rotate rapidly ($v\sin i \approx 40$–100 km/s), and, therefore, should exhibit increased chromospheric and coronal activity. On the other hand, as we have shown, the effects of flows of matter from the optical star to the relativistic object cannot disrupt a stellar corona with a rotational velocity of about 100 km/s if the magnetic-field intensity is at least 1 G. This enables us to estimate the X-ray luminosities of the optical A–M components of quiescent X-ray novae using the maximum values $L_x(0.1\text{–}2.4\ \text{keV}) \approx 10^{-3} L_{\text{bol}}$ for late-type main-sequence stars and $L_x(0.1\text{–}2.4\ \text{keV}) \leq 10^{-4} L_{\text{bol}}$ for subgiants. The expected X-ray luminosities for the coronas of optical A–M stars in X-ray novae are presented in Table 3. In the case of optical A–M main-sequence stars in X-ray novae with black holes, the coronal emission at 0.1–2.4 keV is of the same order of magnitude as the observed X-ray luminosities in the quiescent state.

Thus, the X-ray emission of low-mass X-ray novae in their quiescent state is apparently produced in the coronas of their optical components (active late-type stars). When the optical components are late-type dwarfs, the structure of their coronas is similar to that of the Sun, even in the presence of axial-rotation velocities of about 100 km/s and despite perturbations associated with the proximity of a black hole. The situation for the two other systems under consideration (namely, with late-type subgiants) is different: if the coronas of their optical components are similar to that of the Sun, they can produce only a few percent of the observed quiescent X-ray luminosity of these systems. On the other hand, under these extreme conditions, late-type subgiants can undergo a transition to another type of corona that is radically different from the Sun's. The X-ray emission of such coronas will be one to two orders of magnitude greater than the maximum values observed for subgiants in the solar neighborhood (see, for example, Fig. 3). All these facts must be taken into account when physically interpreting the observational data obtained by the new generation of X-ray observatories, such as *CHANDRA*, *XMM*, *INTEGRAL*, etc.

ACKNOWLEDGMENTS

We thank M.A. Livshits for fruitful discussions. This work was supported by the Program for State Support of Leading Scientific Schools of the Russian Federation (grant 00-15-96533), the "Astronomiya" State Science and Technology Program (grant 1.4.3.4), and NATO grant PST.CLG.976557.

REFERENCES

1. A. M. Cherepashchuk, N. A. Katysheva, T. S. Khruzina, and S. Yu. Shugarov, in *Highly Evolved Close Binary Stars: Catalog* (Gordon and Breach, Amsterdam, 1996).
2. A. M. Cherepashchuk, N. A. Katysheva, T. S. Khruzina, and S. Yu. Shugarov, in *Highly Evolved Close Binary Stars: Finding Charts* (Gordon and Breach, Amsterdam, 1996), p. 1.
3. S. A. Grebenev, R. A. Sunyaev, and M. N. Pavlinsky, Adv. Space Res. **19**, 15 (1997).
4. Y. Tanaka and N. Shibazaki, Ann. Rev. Astron. Astrophys. **34**, 607 (1996).
5. A. M. Cherepashchuk, Space Sci. Rev., 2000 (in press).
6. M. A. Abramowicz, X. Chen, S. Kato, *et al.*, Astrophys. J. Lett. **438**, L37 (1995).
7. R. Narayan, J. E. McClintock, and I. Ji, Astrophys. J. **457**, 821 (1996).
8. R. Narayan, D. Barrett, and J. E. McClintock, Astrophys. J. **482**, 448 (1997).
9. G. S. Bisnovatyĭ-Kogan and R. V. Lovelace, Astrophys. J. Lett. **486**, L43 (1997).
10. G. S. Bisnovatyĭ-Kogan, in *Evidence for Black Holes in the Universe*, Ed. by S. K. Shakrabarti (Kluwer, Dordrecht, 1999), p. L1.
11. R. D. Blandford and M. C. Begelman, Mon. Not. R. Astron. Soc. **303**, 1 (1999).
12. K. Asai, T. Donati, R. Hoshi, *et al.*, Publ. Astron. Soc. Jpn. **50**, 611 (1998).
13. W. Chen, C. R. Shrader, and M. Livio, Astrophys. J. **491**, 312 (1997).

14. M. Hünsch, J. H. Schmitt, M. F. Sterzik, and W. Voges, Astron. Astrophys., Suppl. Ser. **135**, 319 (1999).
15. M. Hünsch, J. H. Schmitt, and W. Voges, Astron. Astrophys., Suppl. Ser. **132**, 155 (1998).
16. M. Hünsch, J. H. Schmitt, and W. Voges, Astron. Astrophys., Suppl. Ser. **127**, 251 (1998).
17. P. P. Eggleton, Astrophys. J. **268**, 368 (1983).
18. V. Straizis and G. Kuriliene, Astrophys. Space Sci. **80**, 353 (1981).
19. R. E. Gershberg, M. M. Katsova, M. N. Lovkaya, *et al.*, Astron. Astrophys., Suppl. Ser. **139**, 555 (1999).
20. D. A. Smith and V. S. Dhillon, Mon. Not. R. Astron. Soc. **301**, 767 (1998).
21. T. Shahbaz, R. M. Bondyopadhyay, P. A. Charles, *et al.*, Mon. Not. R. Astron. Soc., 1999 (in press).
22. E. L. Martin, J. Casares, P. Molano, *et al.*, New Astron. **1**, 197 (1996).
23. M. A. Livshits, Sol. Phys. **173**, 377 (1997).
24. D. Montes and L. W. Ramsey, Astron. Astrophys. **340**, L5 (1998).
25. O. Vilhu and F. M. Walter, Astrophys. J. **321**, 958 (1987).
26. V. B. Baranov and K. V. Krasnobaev, *Hydrodynamic Theory of Cosmic Plasma* [in Russian] (Nauka, Moscow, 1977).
27. O. G. Badalyan, M. A. Livshits, V. N. Obridko, and Yu. Sikora, Izv. Ross. Akad. Nauk, Ser. Fiz. **63** (11), 2196 (1999).
28. A. G. Hearn, Astron. Astrophys. **116**, 296 (1982).
29. M. Güdel, E. F. Guinan, and S. L. Shinner, Astrophys. J. **483**, 947 (1997).
30. M. M. Katsova, O. G. Badalyan, and M. A. Livshits, Astron. Zh. **64**, 1243 (1987) [Sov. Astron. **31**, 652 (1987)].
31. M. Güdel, J. L. Linsky, A. Brown, and F. Nagase, Astrophys. J. **511**, 405 (1999).
32. A. Ortolani, R. Pallavicini, A. Maggio, *et al.*, in *Cool Stars, Stellar Systems, and the Sun*, Ed. by R. A. Donahue and J. A. Bookbinder; Astron. Soc. Pac. Conf. Ser. **154**, CD-1532 (1998).

Translated by Yu. Dumin

Astronomy Reports, Vol. 44, No. 12, 2000, pp. 815–824. Translated from Astronomicheskiĭ Zhurnal, Vol. 77, No. 12, 2000, pp. 922–933.

Scattering of Cyclotron Radiation in a Moving Plasma

A. V. Serber

Institute of Applied Physics of the Russian Academy of Sciences, ul. Ul'yanova 46, Nizhniĭ Novgorod, 603600 Russia

Received December 17, 1999

Abstract—We consider the scattering of cyclotron radiation in a plasma moving along a homogeneous magnetic field. The equation of radiation transfer in a co-moving frame is derived and two limiting cases are pointed out. In the first case of a "small" velocity gradient, the total Doppler frequency shift due to variations in the plasma velocity over the flow is much smaller than the width of the line. The second, opposite, case of a "large" velocity gradient is analogous to the Sobolev approximation in the theory of moving stellar envelopes. The solution of the transfer equation for a wind-type flow illuminated by radiation of a given intensity is obtained in the latter case, when the influence of the plasma motion on cyclotron scattering is most important. It is shown that cyclotron scattering in a moving plasma differs from the known (and qualitatively similar) problems of resonance scattering in moving stellar envelopes and cyclotron scattering in a motionless plasma permeated by an inhomogeneous magnetic field. In particular, a symmetric absorption band with residual intensity proportional to the velocity gradient appears in the spectrum of the outgoing radiation, while in these two other problems, the depth of the corresponding spectral features cannot exceed half the continuum level. Detailed qualitative analysis reveals that this difference is due to the particular form of the frequency redistribution for cyclotron scattering. © *2000 MAIK "Nauka/Interperiodica".*

1. INTRODUCTION

It is well known that cyclotron interaction of radiation with magnetoplasma plays an important role under the conditions present in magnetic degenerate stars. In particular, there are a number of cases where the macroscopic velocity of the plasma is nonzero. These include, for example, the plasma of an accretion column flowing into the magnetosphere of a white dwarf or neutron star from a binary companion [1–3], electron–positron plasma created above the polar hot spot of a neutron star during a gamma-ray burst and accelerated by radiation pressure [4, 5], and steady-state plasma flows from the hot photospheres of magnetic degenerate stars driven by cyclotron radiation [6, 7]. This necessitates an analysis of cyclotron radiation transfer in a moving plasma.

The scattering of radiation in a moving medium is a classical astrophysical problem, and the Sobolev approximation is usually used when analyzing radiation transfer in astrophysical flows [8, 9]. This type of analysis is usually performed for media with an isotropic velocity distribution for the scattering particles, and the known results in this field were obtained precisely for this case. However, the standard theory cannot be directly used to describe the scattering of cyclotron radiation in a moving plasma. In this case, the role of the external degree of freedom associated with the motion of the scattering center as a whole is played by electron motion along the magnetic field, while the transverse motion of an electron (which is, generally speaking, quantized) corresponds to the internal degree of freedom responsible for its interaction with radiation. In other words, in cyclotron scattering, the distribution function of the scattering particles is appreciably anisotropic. The external degree of freedom usually corresponds to a one-dimensional thermal distribution of electrons over longitudinal momenta, and the Landau level populations (the distribution corresponding to the inner degree of freedom) is determined by the intensity of the cyclotron radiation.[1] It will be shown below that this feature makes the transfer of cyclotron radiation peculiar and qualitatively different from the known cases.

In this paper, we consider the transfer of cyclotron radiation in a plasma moving along the field lines of a uniform magnetic field **B** with velocity $v(z) \ll c$ (the z axis is directed along **B**). We assume that the geometric size of the region occupied by the flow is much smaller than the thermalization length of the radiation in the cyclotron line. In this case, one can assume with good accuracy that pure scattering takes place in the cyclotron line (see the corresponding criteria in [13, 14]). The natural width of the cyclotron line in the strong magnetic fields of degenerate stars[2] is much less than the Doppler width of the line. This enables analysis of the transfer of cyclotron radiation in the line core assuming the scattering is coherent in the electron frame[3] and that the frequency redistribution is purely

[1] Electron distribution over the Landau levels taking into account the effect of cyclotron radiation was analyzed in detail in [10–12].

[2] Recall that white dwarfs can have magnetic fields up to 10^8–10^9 G [15]. The existence of magnetic fields $B \sim 10^{11}$–10^{12} G in neutron stars is indicated by the detection of absorption features in the spectra of X-ray pulsars, interpreted as absorption lines at the cyclotron harmonics [16, 17].

[3] This approximation is described by taking a δ-function limit for the electron scattering cross section [4, 9, 18].

1063-7729/00/4412-0815$20.00

Doppler in the comoving frame, in which the plasma is motionless. In this frame, the longitudinal electron momentum[4]

$$p_{\parallel} = mc\frac{\omega' - \omega_B}{\omega'\cos\alpha'} = \text{const}, \quad (1)$$

is conserved during the cyclotron scattering if the recoil effect and the frequency redistribution due to the finite natural line width are neglected. In (1), ω' and $\cos\alpha'$ are the frequency of the radiation and the angle between the direction of its propagation and the magnetic field in the rest frame of the plasma. During cyclotron scattering in a homogeneous magnetic field, these parameters vary such that the radiation interacts only with electrons whose longitudinal momentum in the comoving frame is given by (1):

$$\frac{\omega' - \omega_B}{\omega'\cos\alpha'} = \frac{\tilde{\omega}' - \omega_B}{\tilde{\omega}'\cos\tilde{\alpha}'}. \quad (2)$$

Here and below, a tilde denotes quantities corresponding to the scattered radiation.

To find the scattering coefficient in the comoving frame of a medium, we must average the scattering cross section of an individual particle over the distribution function of the scattering particles, taking into account their thermal motion via the Doppler resonance condition. As a result, a factor describing the frequency profile of the line appears in the scattering coefficient. Since there are no distinct directions in a medium with temperature T and an isotropic Maxwellian particle distribution, the frequency profile of the scattering coefficient does not depend on the ray direction, and is proportional to $\exp\left(-\frac{(\omega' - \omega_0)^2}{2(\omega'\beta_T)^2}\right)$, where $\beta_T = (\kappa T/mc^2)^{1/2}$ (if natural broadening is neglected). Photons with frequency ω' propagating in such a medium occupy a strictly definite position relative to the line center ω_0 that is the same for all ray directions, so that the scattering coefficient for all these photons is the same. Of course, radiation from a frequency interval $d\omega'$ near ω' is scattered in different directions by different groups of particles, but the numbers of particles in such groups in a volume element of the medium is independent of the ray direction. In contrast to this case, which is usually realized in stellar atmospheres, there is a distinct direction in a magnetized plasma, corresponding to the magnetic field. In this case, the cyclotron scattering is due to electrons with a one-dimensional Maxwellian distribution, so that the number of particles in resonance with the radiation at a given frequency ω' depends on the ray direction α'. Thus, the cyclotron line profile $\exp\left(-\frac{(\omega' - \omega_B)^2}{2(\omega'\beta_{T_{\parallel}}\cos\alpha')^2}\right)$, where $T_{\parallel}$ is the longitudinal temperature of the plasma, becomes angle-dependent, and scattering that changes α' also changes the photon positions relative to the line center.

Bulk motion of a medium gives rise to a Doppler frequency shift and aberration. We expect that the influence of the former on radiation in a cyclotron line of width $\beta_{T_{\parallel}} \ll 1$ already becomes pronounced in non-relativistic plasma with $\sim\beta_{T_{\parallel}}\omega_B$ at flow velocities $\beta \sim \beta_{T_{\parallel}}$. On the contrary, aberration affects radiation in a wide angular range $\cos\alpha \sim 1$ only if the flow is relativistic ($\beta \sim 1$). In the case at hand, this effect is important only for radiation with $\cos\alpha \sim \beta \ll 1$, which makes only a small contribution. This means that we can neglect aberration, and only the effects of Doppler variation of the frequency need be taken into account in the transfer equation for cyclotron radiation in a moving plasma, which will be derived in the next section.

If ω' and $\cos\alpha'$ are expressed in terms of the corresponding rest-frame quantities, the cyclotron-resonance condition (1) can be written in the form

$$\gamma\omega\left[1 - \beta\cos\alpha - \frac{p_{\parallel}}{mc}(\cos\alpha - \beta)\right] = \omega_B,$$

where $\beta = v/c$ and $\gamma = (1 - \beta^2/c^2)^{-1/2}$. Note that this relation holds for arbitrary β. In the case of a nonrelativistic flow, we should make a linear expansion over β in this formula and use a frequency-redistribution law in the form

$$\omega\left[1 - \left(\beta + \frac{p_{\parallel}}{mc}\right)\cos\alpha\right] = \omega_B. \quad (3)$$

2. TRANSFER EQUATION FOR CYCLOTRON RADIATION IN A MOVING PLASMA

Our analysis below focuses on the case where the polarization of the mode is determined by a rarefied plasma and the effects of the magnetized vacuum are negligible [19]. Further, we assume that the optical depth of the plasma flow to scattering of the ordinary mode is fairly low. In this case, we can leave out of consideration the transfer of this component, as well as mode switching due to the scattering (this process was analyzed in [20]).

Generally speaking, in the laboratory frame fixed to the magnetic field, the scattering coefficient $\chi_{11}(z, \omega, \alpha)$ for the extraordinary mode at the first harmonic in the moving plasma and the corresponding source function $S_1(z, \omega, \alpha)$ are unknown. These quantities are known only for a motionless plasma; they can be derived in a frame in which the plasma is moving via a Lorentz transformation [9]. If this were done, it would be

[4] This quantity is obtained from the condition that the frequency of radiation with a given ω' and $\cos\alpha'$ is equal to the gyrofrequency ω_B in the frame of an electron with this longitudinal momentum.

impossible to separate the angular and frequency variables in the coefficients $\chi_{11}(z, \omega, \alpha)$ and $S_1(z, \omega, \alpha)$, so that analyzing and solving the transfer equation would be quite complicated. Therefore, following the well-established technique, we write the transfer equation

$$\cos\alpha\frac{\partial I_\omega(z, \omega, \alpha)}{\partial z} = -\chi_{11}(z, \omega, \alpha)[I_\omega(z, \omega, \alpha) + S_1(z, \omega)] \quad (4)$$

for the spectral intensity of the extraordinary radiation $I_\omega(z, \omega, \alpha)$ in the comoving frame, in which such difficulties do not arise. Of course, in so doing, we must take into account the fact that the position of a photon with a fixed frequency ω relative to the profile of the cyclotron line varies with z in a medium with nonconstant velocity $v(z)$.[5]

Let us introduce the dimensionless variable $\xi \equiv p_\parallel/\sqrt{2}\,mc\beta_{T_\parallel}$ in Eq. (4), which describes the position of a photon with respect to the line center in the comoving frame. This is done by multiplying (4) by the delta-function

$$\delta_\omega \equiv \delta[\omega(1 - (\sqrt{2}\beta_{T_\parallel}\xi + \beta(z))\cos\alpha) - \omega_B] \quad (5)$$

and integrating over frequency:

$$\int\cos\alpha\frac{\partial I_\omega(z, \omega, \alpha)}{\partial z}\delta_\omega d\omega = -\chi_{11}(z, \xi, \alpha)[I_{11}(z, \xi, \alpha) - S_1(z, \xi)].$$

In this equation,

$$\chi_{11}(z, \xi, \alpha) = \frac{\sqrt{2}\pi^2 e^2 N(z)}{mc\beta_{T_\parallel}\omega_B}\frac{1 + \cos^2\alpha}{|\cos\alpha|}\phi(\xi)$$

and

$$S_1(z, \xi) = \int\frac{3}{8}(1 + \cos^2\alpha)I_\omega(z, \xi, \alpha)d\cos\alpha,$$

respectively, are the opacity and source function in a motionless rarefied plasma with a Maxwellian distribution for the longitudinal momenta of the electrons [11], the function $\phi(\xi) = \pi^{-1/2}e^{-\xi^2}$ describes the Doppler profile of the cyclotron line, and the spectral intensity (cf. [4, 13])

$$I_{11}(z, \xi, \alpha) \equiv \int I_\omega(z, \omega, \alpha)\delta_\omega d\omega \quad (6)$$

corresponds to the extraordinary mode at the first harmonic, which interacts with electrons with longitudinal momentum $p_\parallel = \sqrt{2}\,mc\beta_{T_\parallel}\xi$ in the comoving frame. Using the rules for taking the derivative of a delta-function, we calculate the integral on the left-hand side (cf. [13]):

$$\int\frac{\partial}{\partial z}I_\omega(z, \omega, \alpha)\delta_\omega d\omega = \frac{\partial I_{11}(z, \xi, \alpha)}{\partial z} - \cos\alpha\frac{\partial\beta}{\partial z}\int\left(I_\omega + \omega\frac{\partial I_\omega}{\partial\omega}\right)\delta_\omega d\omega = \frac{\partial I_{11}(z, \xi, \alpha)}{\partial z} - \cos\alpha\frac{\partial\beta}{\partial z} \times\left(I_{11}(z, \xi, \alpha) + \frac{1}{\sqrt{2}\beta_{T_\parallel}\cos\alpha}\frac{\partial I_{11}(z, \xi, \alpha)}{\partial\xi}\right).$$

Making the order-of-magnitude estimates

$$\frac{1}{\sqrt{2}\beta_{T_\parallel}\cos\alpha}\frac{\partial I_{11}(z, \xi, \alpha)}{\partial\xi} \sim \frac{I_{11}}{\beta_{T_\parallel}\cos\alpha},$$

we find that the second term in the resulting expression can be neglected compared to the third term in a nonrelativistic plasma with $\beta_{T_\parallel} \ll 1$.

As a result, the transfer equation takes the form

$$\cos\alpha\frac{\partial I_{11}(z, \xi, \alpha)}{\partial z} - \frac{\cos\alpha}{\sqrt{2}\beta_{T_\parallel}}\frac{\partial\beta}{\partial z}\frac{\partial I_{11}(z, \xi, \alpha)}{\partial\xi} = -\chi_{11}(z, \xi, \alpha)[I_{11}(z, \xi, \alpha) - S_1(z, \xi)]. \quad (7)$$

This equation describes cyclotron scattering in a plasma layer moving nonuniformly along the field lines of a homogeneous magnetic field. The first term on the left-hand side accounts for spatial radiation transfer, while the second term, proportional to the velocity gradient, describes the frequency drift in the comoving frame (variation in ξ) due to the Doppler shift of the cyclotron line in the moving medium. We emphasize that both these terms are proportional to $\cos\alpha$, and change their signs simultaneously when the sign of $\cos\alpha$ changes. In this case, the transfer operator is a degenerate hyperbolic (i.e., its characteristics are identical for any $\cos\alpha$), while the transfer directions and velocities for radiation at different angles are different.

This feature distinguishes (7) from the well-known equations of cyclotron scattering in an inhomogeneous magnetic field [13, 14] and resonance monochromatic scattering in a two-level gas moving with nonconstant velocity [21, 22]. In both these cases, the terms describing the frequency drift do not include the angular variable, and its sign is independent of the direction of radiation transfer. The corresponding transfer operator is hyperbolic, and the slope of its characteristics is proportional to $\cos\alpha$. Physically, this difference is related to the fact that alternation of the sign of $\cos\alpha$ in the case of cyclotron scattering leads to changes in the photon position relative to the local line center in a moving plasma. In particular, photons from the red wing of the line, where $\omega' < \omega_B$, are scattered into the blue wing

[5] As noted in the Introduction, we assume that aberration can be neglected.

($\omega' < \omega_B$) and vice versa (see the detailed discussion in the next section).

Let us compare the order of magnitude of the first and second terms on the left-hand side of (7). Let H be the size of the flow region and $L_\beta \equiv \beta|\partial\beta/\partial z|^{-1}$ its characteristic spatial scale. Then,

$$\frac{\partial I_{11}(z, \xi, \alpha)}{\partial z} \sim \frac{I_{11}}{\min(H, L_\beta)},$$
$$\frac{1}{\sqrt{2}\beta_{T_\parallel}}\frac{\partial\beta}{\partial z}\frac{\partial I_{11}(z, \xi, \alpha)}{\partial\xi} \sim \frac{\beta}{\beta_{T_\parallel}}\frac{I_{11}}{L_\beta}. \quad (8)$$

These estimates show that we can distinguish two limiting cases: that of "small" flow-velocity gradients $|\partial\beta/\partial z| \ll \beta_{T_\parallel}/H$ and the opposite case of "large" gradients, for which

$$\left|\frac{\partial\beta}{\partial z}\right| \gg \frac{\beta_{T_\parallel}}{H}. \quad (9)$$

In the first case, the velocity variation in the plasma flow is small compared to the thermal velocity of the scattering particles (electrons), so that the corresponding Doppler frequency shift is much smaller than the width of the cyclotron line. The effect of the plasma motion on cyclotron scattering is insignificant in this case, so that the second term on the left-hand side of Eq. (7) can be neglected. As a result, this equation reduces to the equation for a motionless medium

$$\cos\alpha\frac{\partial I_{11}(z, \xi, \alpha)}{\partial z} = -\chi_{11}(z, \xi, \alpha)[I_{11}(z, \xi, \alpha) - S_1(z, \xi)],$$

which was considered in detail in [4, 11, 13]. On the contrary, in case (9), we should omit the first term in the transfer operator:

$$\frac{\cos\alpha}{\sqrt{2}\beta_{T_\parallel}}\frac{\partial\beta}{\partial z}\frac{\partial I_{11}(z, \xi, \alpha)}{\partial\xi} = \chi_{11}(z, \xi, \alpha)[I_{11}(z, \xi, \alpha) - S_1(z, \xi)] \quad (10)$$

since the formation of the radiation field is mainly affected by the frequency drift, resulting in photon escape from the resonance line rather than the spatial transfer of radiation. Below, we focus our analysis on this case, when the influence of the medium's motion on cyclotron scattering is most pronounced.

Let us find the solution of Eq. (10), assuming that criterion (9) is satisfied, and the flow velocity $\beta(z)$ increases monotonically in the region $0 \le z \le H$. This corresponds to a wind-type plasma outflow from a star. Let no radiation be incident on the upper boundary of the flow, $z = H$, and its lower boundary be illuminated by radiation with known specific intensity $I_\omega^{\rm inc}(\omega, \alpha)$ in the extraordinary mode. Then, the boundary conditions in the frame fixed to the magnetic field have the form

$$I_\omega(z = 0, \omega, \cos\alpha > 0) = I_\omega^{\rm inc}(\omega, \alpha)$$
$$I_\omega(z = H, \omega, \cos\alpha < 0) = 0.$$

We multiply these term-by-term by the delta-function (5) and integrate over frequency. As a result, we obtain the corresponding conditions in the comoving frame:

$$I_{11}(z = 0, \xi, \cos\alpha > 0) = I_\omega^{\rm inc}(\omega_B[1 - (\sqrt{2}\beta_{T_\parallel}\xi + \beta(0))\cos\alpha]^{-1}, \alpha), \quad (11)$$

$$I_{11}(z = H, \xi, \cos\alpha < 0) = 0. \quad (12)$$

Assuming that the incident radiation varies slowly over the width of the cyclotron line:

$$\beta_{T_\parallel}\omega_B\left|\frac{\partial I_\omega^{\rm inc}}{\partial\omega}\right| \ll I_\omega^{\rm inc},$$

we write (11) in the form

$$I_{11}(z = 0, \xi, \cos\alpha > 0) = I_\omega^{\rm inc}(\omega_B[1 - \beta(0)\cos\alpha]^{-1}, \alpha). \quad (13)$$

We now transform (10) in terms of the new variable

$$y = \int_{-\infty}^{\xi}\phi(\xi)d\xi \quad (14)$$

so that this equation takes the form

$$\cos\alpha\frac{\partial I_{11}(z, y, \alpha)}{\partial y} = \tau_\beta\frac{1 + \cos^2\alpha}{2|\cos\alpha|}[I_{11}(z, y, \alpha) - S_1(z, y)], \quad (15)$$

where

$$\tau_\beta = \frac{4\pi^2e^2N}{mc\omega_B}\left|\frac{\partial\beta}{\partial z}\right|^{-1} \quad (16)$$

is the optical depth of the flow to cyclotron scattering in the extraordinary mode. This quantity, which is inversely proportional to the flow-velocity gradient, has meaning analogous to the Sobolev optical depth in the theory of moving stellar atmospheres [9, 22]. On the other hand, note that the form of (15) is analogous to the equation of cyclotron scattering in a motionless plasma in a quasi-homogeneous magnetic field [4, 13, 23].

To transform the boundary conditions (12) and (13) in terms of y, we note that, if radiation at some frequency ω propagates upward ($\cos\alpha > 0$) in a wind-type flow ($\partial\beta/\partial z > 0$), ξ decreases monotonically, while this quantity increases monotonically in the case of downward radiation ($\cos\alpha < 0$). Thus, plasma at the lower

boundary $z = 0$ interacts with upward radiation in the frequency range

$$\frac{\omega_B}{1-(\beta(0)-\sqrt{2}\beta_{T_\parallel}\xi_{\max})} \lesssim \omega \lesssim \frac{\omega_B}{1-(\beta(H)+\sqrt{2}\beta_{T_\parallel}\xi_{\max})},$$

where $\xi_{\max} \gg 1$ is chosen such that we can assume $y \approx 0$ at $\xi < -\xi_{\max}$ and $y \approx 1$ at $\xi > \xi_{\max}$. Since criterion (9) is met for the flow, the interval $\beta(H) - \beta(0) \gg \sqrt{2}\beta_{T_\parallel}\xi_{\max}$. In addition, if $H \gg L_\beta$, radiation enters the cyclotron line due to the frequency drift rather that through the flow boundaries $z = 0$ and $z = H$, and this takes place over nearly the entire flow, except in narrow regions near its boundaries. Thus, for nearly the entire range

$$\omega_B/(1-\beta(0)) \lesssim \omega \lesssim \omega_B/(1-\beta(H)), \tag{17}$$

except frequencies in intervals $\lesssim \sqrt{2}\beta_{T_\parallel}\xi_{\max}\omega_B$ near its ends, Eq. (13) can be written in the form

$$\begin{aligned} &I_{11}(z=0, y\simeq 1, \cos\alpha > 0) \\ &\simeq I_\omega^{\rm inc}(\omega_B[1-\beta(0)\cos\alpha]^{-1},\ \alpha) \equiv I^{\rm inc}. \end{aligned} \tag{18}$$

A similar treatment for the downward radiation at the upper boundary of the flow shows that boundary condition (12) is transformed in terms of y as follows:

$$I_{11}(z=H, y\simeq 0, \cos\alpha < 0) = 0. \tag{19}$$

This formula is valid in the frequency range

$$\omega_B/(1+\beta(H)) \lesssim \omega \lesssim \omega_B/(1+\beta(0)). \tag{20}$$

The source function of Eq. (15) can easily be found using the Schwarzschild–Shuster method [18], which has been widely used for obtaining approximate solutions of the cyclotron radiation transfer equation. Following the standard procedure [10–14, 23], we obtain from (15) the pair of equations

$$\pm\frac{1}{2}\frac{dI^{(1),(2)}}{dy} = \tau_\beta\left[-I^{(1),(2)} + \frac{I^{(1)}+I^{(2)}}{2}\right] \tag{21}$$

for the average intensities

$$I^{(1)} = \int_0^1 I_{11}(z, y, \alpha)d\cos\alpha,$$

$$I^{(2)} = \int_{-1}^0 I_{11}(z, y, \alpha)d\cos\alpha,$$

which, in the adopted approximation, are related to the source function as follows:

$$S_1(y) = \frac{I^{(1)}(y)+I^{(2)}(y)}{2}.$$

Solving system (21) under the boundary conditions (18) and (19), we obtain the desired source function

$$S_1 = \frac{I^{(0)}}{2}\frac{2\tau_\beta y + 1}{\tau_\beta + 1}, \tag{22}$$

where

$$I^{(0)} = \int_0^1 I_\omega^{\rm inc}(\omega_B[1-\beta(0)\cos\alpha]^{-1}, \alpha)d\cos\alpha.$$

Up to a change of variables, this is identical to the source function in a motionless medium [13, 22], and differs qualitatively from the source functions describing cyclotron scattering in a strongly inhomogeneous magnetic field and monochromatic scattering in a moving gas. In those cases, $S_1 \simeq$ const over the entire region of interaction between the radiation and medium. On the contrary, Eq. (22) is a linear function of the effective optical depth τ_β. Note that the frequency range of the radiation scattered by a nonrelativistic flow with $\max\beta(z) \ll 1$ is much less than ω_B. Then, if

$$\left|\frac{\partial I_\omega^{\rm inc}}{\partial\omega}\right|\omega_B\max\beta(z) \ll I_\omega^{\rm inc}(\omega_B),$$

we can approximately set

$$I^{(0)} \simeq I_\omega^{\rm inc}(\omega_B).$$

Substituting (22) in (21) and solving this using (18) and (19), we obtain the intensity of the outgoing radiation at the upper boundary of the flow,

$$\begin{aligned} &I_{11}(z=H, y=0, \cos\alpha > 0) \\ &= I^{\rm inc}\exp\left(-\frac{1+\cos^2\alpha}{2\cos^2\alpha}\tau_\beta\right) \\ &+ \frac{I^{(0)}}{1+\tau_\beta}\frac{1+5\cos^2\alpha}{2(1+\cos^2\alpha)}\left[1-\exp\left(-\frac{1+\cos^2\alpha}{2\cos^2\alpha}\tau_\beta\right)\right] \\ &- \frac{I^{(0)}\tau_\beta}{1+\tau_\beta}\exp\left(-\frac{1+\cos^2\alpha}{2\cos^2\alpha}\tau_\beta\right), \end{aligned} \tag{23}$$

and the radiation that is reflected from the flow and escapes from the lower boundary:

$$\begin{aligned} &I_{11}(z=0, y=1, \cos\alpha < 0) \\ &= \frac{I^{(0)}}{1+\tau_\beta}\left[\tau_\beta + \frac{1-3\cos^2\alpha}{2(1+\cos^2\alpha)}\left(1-\exp\left(-\frac{1+\cos^2\alpha}{2\cos^2\alpha}\tau_\beta\right)\right)\right]. \end{aligned} \tag{24}$$

The intensity of cyclotron radiation leaving an optically thick plasma wind with $\tau_\beta \gg 1$ is equal to

$$I_{11}(z = H, y = 0, \cos\alpha > 0)$$
$$\simeq \frac{I^{(0)}}{\tau_\beta}\frac{1 + 5\cos^2\alpha}{2(1 + \cos^2\alpha)} \propto \tau_\beta^{-1}, \quad (25)$$
$$I_{11}(z = 0, y = 1, \cos\alpha < 0)$$
$$\simeq I^{(0)}\left(1 - \tau_\beta^{-1}\frac{1 + 5\cos^2\alpha}{2(1 + \cos^2\alpha)}\right).$$

Note that the intensities of the radiation leaving an optically thick, pure-scattering layer in which the intrinsic emission and absorption due to particle collisions are neglected are related as follows:

$$I_{11}(z = 0, y = 1, \cos\alpha < 0)$$
$$+ I_{11}(z = H, y = 0, \cos\alpha > 0) = I^{(0)}.$$

We can see from the solution obtained that, if (9) is satisfied, cyclotron scattering in a wind-type flow results in the formation of an absorption band in the outgoing radiation at frequencies (17) corresponding to $y \simeq 0$ at $\cos\alpha > 0$. The width of this band is much larger than the width of the cyclotron line in a motionless plasma, and is determined by the Doppler shift of the gyrofrequency due to the variation in the flow velocity $\Delta\omega_\beta \sim \omega_B(\beta(H) - \beta(0)) \gg \beta_{T_\parallel}\omega_B$. The residual intensity in the band depends on the effective optical depth (16), and is proportional to $\tau_\beta^{-1} \propto |dv/dz|$ in an optically thick flow. Accordingly, in the backscattered radiation, an emission band is formed with intensity similar to that of the incoming intensity at frequencies (20) for which $y \simeq 1$ at $\cos\alpha < 0$.

Formulas (23)–(25) are clearly analogous to the solution for cyclotron scattering in a motionless plasma in a quasi-homogeneous magnetic field [13, 23]. In particular, in both cases, an absorption feature forms in the outgoing radiation. The residual intensity in this feature is inversely proportional to the effective optical depth, and can be much less than the intensity of the incoming radiation. These two cases differ in the width of the spectral feature formed, which is about $\simeq \beta_{T_\parallel}\omega_B$ for cyclotron scattering in a motionless plasma and is much larger if the plasma is moving.

It is known that absorption features with widths much larger than the width of the resonance line in a motionless medium can be formed, e.g., by cyclotron scattering in a motionless plasma permeated by a strongly inhomogeneous magnetic field [13, 14] or by resonance scattering in a nonuniformly moving gas [9, 21, 22]. In these cases, however, which are qualitatively similar to each other, the intensity of the outgoing radiation cannot be less than half the intensity of the incoming radiation, and the intensity of the reflected radiation cannot be greater than half the incoming intensity. Therefore, the distinguishing feature of the process considered here is the formation of wide bands with residual intensity much lower than the intensity of the incoming radiation (in the limit of large optical depth). In the next section, we perform a qualitative analysis of the solution obtained, compare cyclotron scattering in a moving plasma with the two cases indicated above, and show that the characteristic features of the process under consideration are related to the kinematics of an elementary act of cyclotron scattering in a moving plasma.

3. DISCUSSION

We can explain the result obtained using the frequency–coordinate diagram shown in Fig. 1. Similar diagrams were used in [14, 21]. For simplicity, we assume that the flow velocity increases linearly with z, i.e.,

$$\beta(z) = \beta_0(1 + z/L_\beta), \quad (26)$$

approximate the frequency profile of the line to be rectangular

$$\phi(\xi) = \begin{cases} 1 & \text{at} \quad |\xi| \le \xi_{\max} \\ 0 & \text{at} \quad |\xi| > \xi_{\max} \end{cases} \quad (27)$$

and limit our analysis to a two-flux approximation, in which the radiation is assumed to propagate in only two directions $\cos\alpha = \pm 1/2$. The dash–dot lines $\omega = \omega_B[1 \pm \beta(z)/2]$ in Fig. 1 show the location of the local center of the cyclotron line. Here, a positive sign corresponds to upward radiation ($\cos\alpha = 1/2$), and a negative sign to downward radiation ($\cos\alpha = -1/2$). The solid lines $\omega = \omega_B[1 \pm (\beta(z)/2 + \beta_{T_\parallel}\xi_{\max}/\sqrt{2})]$ and dashed lines $\omega = \omega_B[1 \pm (\beta(z)/2 - \beta_{T_\parallel}\xi_{\max}/\sqrt{2})]$ in this figure correspond to $\xi = \xi_{\max}$ and $\xi = -\xi_{\max}$, respectively. Thus, radiation in a certain direction can be scattered only in the gyroresonance layer, the band between the solid and dashed lines. Note that, for $\cos\alpha = 1/2$, this band is located to the right of the solid vertical line, in the region where $\omega > \omega_B$. If $\cos\alpha = -1/2$, this band is located to the left of this line, in the region where $\omega < \omega_B$. We also note that the solid line $\xi = \xi_{\max}$ for the upward radiation corresponds to the "blue" wing of the line, $\omega' > \omega_B$, while the dashed line $\xi = -\xi_{\max}$ corresponds to its "red" wing, $\omega' < \omega_B$. On the contrary, $\xi = -\xi_{\max}$ at $\omega' > \omega_B$ and $\xi = \xi_{\max}$ at $\omega' < \omega_B$ for downward radiation.

For comparison, Figs. 2 and 3 show frequency–coordinate diagrams for cyclotron scattering in an inhomogeneous magnetic field $\omega_B = \omega_{B_0}(1 - z/L_B)$ (cf. [14]) and resonance monochromatic scattering in a two-level gas moving nonuniformly with velocity (26) (cf. [21]). Let us first discuss Fig. 2. In this case, the frequency redistribution due to scattering is determined by the Doppler condition (2) with $\omega_B = \omega_B(z)$. Therefore, in

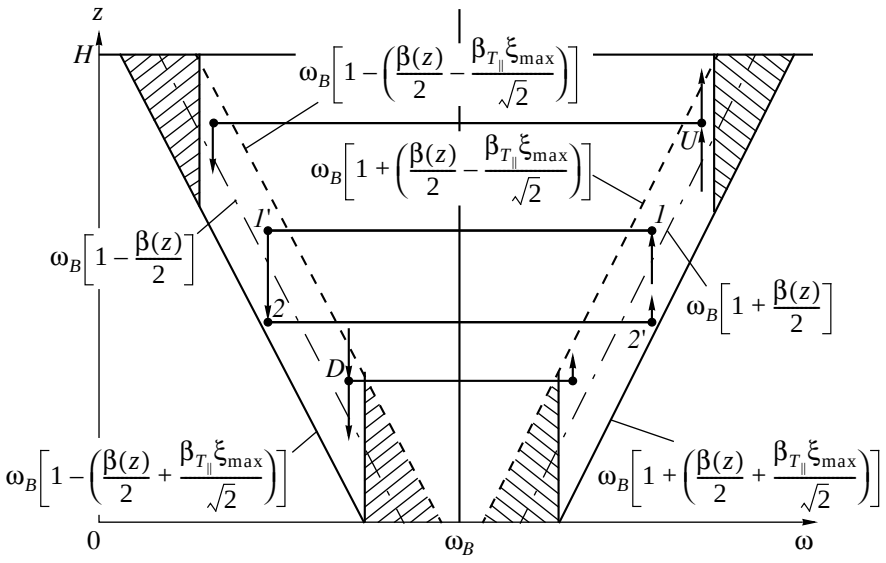

Fig. 1. Frequency–coordinate diagram for cyclotron scattering in a moving plasma in a rectangular approximation for the line profile and a two-flux approximation for the angular pattern of the radiation. The frequency-redistribution law is illustrated by the example of scattering of upward and downward radiation at the points *U* and *D*, respectively. The broken line 1, 1', 2, 2' shows the motion of the reference point in the course of two successive scattering events, both of which alter the direction of propagation of the radiation. Further in formation is given in the text.

contrast to our case, the locations of the local line center and the gyroresonance layer are identical for any $\cos\alpha$, and the lines $\xi = \pm\xi_{\max}$ for different values of $\cos\alpha$ are symmetric with respect to $\omega_B = \omega_B(z)$. As we can see in Fig. 3, in an isotropic medium with a Maxwellian velocity distribution for the scattering center, in a monochromatic-scattering approximation in the comoving frame, the relative positions of the line wings and the regions of interaction between the plasma and radiation are similar to those in Fig. 1. This is a consequence of the frequency-redistribution law

$$\omega' = \tilde{\omega}', \tag{28}$$

where we can set $\omega' \simeq \omega - \omega_0\beta\cos\alpha$ without significant loss of accuracy (ω_0 is the frequency of the resonance transition).

Let us consider the motion of a photon in the frequency–coordinate diagram during cyclotron scattering in a wind-type flow. If a photon propagates freely during the time between scattering events, its parameters z and ξ vary, while ω and α remain constant. The representative point in the diagram moves along the line $\omega = \text{const}$ in the direction determined by the sign of $\cos\alpha$. Photons of upward radiation moving toward increasing z travel from larger to smaller values of ξ. On the contrary, the z coordinates of downward photons decrease and their resonance velocities ξ increase. As a result, there is a frequency drift of radiation from the "blue" to the "red" wing of the cyclotron line. The frequency drift in Fig. 3 is the same, for any sign of $\cos\alpha$. In the inhomogeneous magnetic field in Fig. 2, photons shift from smaller to larger values of ξ for any α, and the direction of the frequency drift alternates compared to Fig. 1. In this case, upward photons drift from the "red" to the "blue" wing of the line, and downward photons from the "blue" to the "red" wing. A scattering event does not change z. The quantity ξ and the radia-

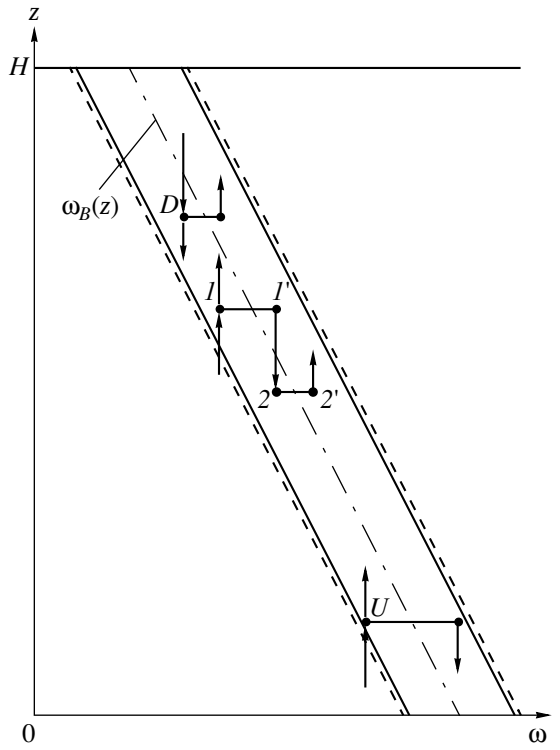

Fig. 2. Same as Fig. 1 for cyclotron scattering in a motionless plasma permeated by an inhomogeneous magnetic field.

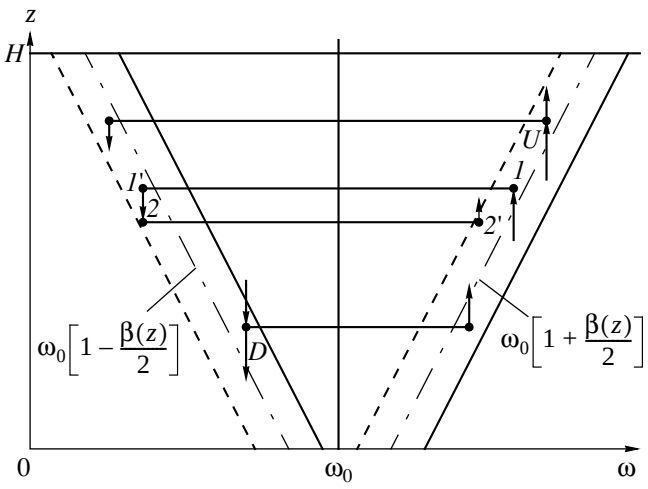

Fig. 3. Same as Fig. 1 for resonance monochromatic scattering in a nonuniformly moving gas.

tion frequency ω' in the comoving frame are conserved during cyclotron scattering and monochromatic scattering by atoms, respectively. This means that ω and α vary in a certain way. In the two-flux approximation, the location of the representative point in all three diagrams is unchanged if the direction of photon propagation is not changed after a scattering event. However, if the sign of $\cos\alpha$ changes, due to the corresponding frequency-redistribution laws and taking into account the conservation of *z*, radiation frequency ω must change. In Fig. 1, this variation in frequency corresponds to motion the representative point along the line *z* = const, to a location symmetric with respect to the initial one with respect to the $\omega = \omega_B$ axis:

$$\omega - \omega_B = \omega_B - \tilde{\omega}. \qquad (29)$$

Let us make note of the distinguishing features of cyclotron scattering in a moving plasma. First, the location of the symmetry axis is independent of *z*, so that (29) with ω_B = const precisely coincides with the frequency variation for the case of cyclotron scattering in a motionless plasma in a homogeneous magnetic field. Second, alternation of the sign of $\cos\alpha$ results in photon scattering from the "blue" to the "red" wing of the line, and vice versa. Relation (29) is also valid for scattering of cyclotron radiation in an inhomogeneous magnetic field (Fig. 2). However, the location of the symmetry axis $\omega = \omega_B(z)$ varies with *z*. Similar to Fig. 1, scattering with sign alternation leads to a change in the photon position relative to the local line center. Finally, in the case described by the diagram in Fig. 3, the photon position relative to the local line center is the same for all scattering events:

$$\omega - \omega_0(1 + \beta\cos\alpha) \simeq \tilde{\omega} - \omega_0(1 + \beta\cos\tilde{\alpha}). \qquad (30)$$

We show in all three figures examples of variations in the photon position for the case of upward radiation scattered at point *U* and downward radiation scattered at point *D*.

Let us now analyze variations in the photon frequency in the presence of multiple scattering events, assuming that such variations are determined at times when the wave vector of the photon has a certain direction. We consider upward radiation with initial frequency ω_1 subject to two successive scattering events. Let the sign of $\cos\alpha$ alternate, so that the photons ultimately move in the same direction: $\alpha_1 = \tilde{\alpha}_2$. If $\omega_2 = \tilde{\omega}_1$ is the photon frequency before the second scattering, it follows immediately from (29) that there is no frequency shift: $\omega_1 = \tilde{\omega}_2$. This is clearly illustrated by the broken line with vertexes 1, 1', 2, and 2', which is a graphic representation of this process in the diagram in Fig. 1. The similar lines in the two other diagrams illustrate the qualitative difference from the case considered. According to Fig. 2 and (29), in an inhomogeneous magnetic field, systematic variation of the photon frequency occurs when $\omega = \omega_B(z)$: $\tilde{\omega}_2 - \omega_1 = 2[\omega_B(z_2) - \omega_B(z_1)] \neq 0$. In this case, in accordance with the considered variation in the gyrofrequency, upward photons shift from the "red" to the "blue" wing of the line; i.e., the frequencies of these photons increase. At the same time, the frequencies of downward radiation change in the opposite sense. The same frequency shifts take place for radiation undergoing monochromatic scattering in a moving gas. This can be seen from the tracing in Fig. 3 and relations (28) and (30).

In the limiting case of large gradients (9), the flow effectively scatters cyclotron radiation only in the gyroresonance layer $|\xi| \leq \xi_{max}$, which it enters through its boundaries $\xi = \pm\xi_{max}$ and not through the spatial boundaries of the flow *z* = 0 or *z* = *H*. In this case, it seems quite natural that the source function depends only on ξ, or the equivalent variable *y*, but is independent of *z*. Photons in an optically thick flow with $\tau_\beta \gg 1$ can only escape from the gyroresonance layer without scattering if they are located in regions near its boundaries. If a photon first scatters deep in the gyroresonance layer, it then undergoes a large number of scattering events (of the order of the square of the optical depth), and most probably escapes from the boundary of the gyroresonance layer that is closer to the point of its first scattering. The number of incoming photons falls exponentially with decreasing *y*, so that most of these photons are reflected and escape from the boundary *y* = 1. Therefore, the source function, which is the average of the intensities of the upward and downward radiation at fixed *y*, increases with increasing *y* (see (22)). This, in turn, leads to a solution in the form (23) and (24). Similar considerations for scattering in a motionless plasma in a homogeneous magnetic field can explain the similar decrease in S_1 with increasing *z*.

In the cases described by Figs. 2 and 3, the source function is also weakly dependent on the boundary conditions at *z* = 0, *H*. However, here, all photons, inde-

pendent of the sign of $\cos\alpha$, enter the gyroresonance layer at the same y, and then drift in y in the same direction. Thus, under steady-state conditions, the number of such photons is the same for any y, so that the source function must be constant, $S_1(y) \simeq \text{const}$, in the gyroresonance layer in Fig. 2 or the region of resonance scattering in Fig. 3.

Let us now estimate the influence of sharp boundaries of the flow, $z = 0$ and $z = H$. It is clear that these boundaries affect the radiation components entering the gyroresonance layer or escaping from it through these boundaries rather than from the frequency boundaries $\xi = \pm\xi_{\max}$ of the gyroresonance layer. We can see from Fig. 1 that outward radiation from the interval

$$\begin{aligned}\omega_B[1 + (\beta(0)/2 - \beta_{T_\parallel}\xi_{\max}/\sqrt{2})] \lesssim \omega \\ \lesssim \omega_B[1 + (\beta(0)/2 + \beta_{T_\parallel}\xi_{\max}/\sqrt{2})],\end{aligned} \tag{31}$$

enters the gyroresonance layer through the boundary $z = 0$, while downward radiation at frequencies

$$\begin{aligned}\omega_B[1 - (\beta(H)/2 + \beta_{T_\parallel}\xi_{\max}/\sqrt{2})] \lesssim \omega \\ \lesssim \omega_B[1 - (\beta(H)/2 - \beta_{T_\parallel}\xi_{\max}/\sqrt{2})]\end{aligned} \tag{32}$$

enters it through the boundary $z = H$. Next, if upward radiation at frequencies

$$\begin{aligned}\omega_B[1 + (\beta(H)/2 - \beta_{T_\parallel}\xi_{\max}/\sqrt{2})] \lesssim \omega \\ \lesssim \omega_B[1 + (\beta(H)/2 + \beta_{T_\parallel}\xi_{\max}/\sqrt{2})]\end{aligned} \tag{33}$$

and downward radiation in the interval

$$\begin{aligned}\omega_B[1 - (\beta(0)/2 + \beta_{T_\parallel}\xi_{\max}/\sqrt{2})] \lesssim \omega \\ \lesssim \omega_B[1 - (\beta(0)/2 - \beta_{T_\parallel}\xi_{\max}/\sqrt{2})],\end{aligned} \tag{34}$$

enter the gyroresonance layer inside the flow, these radiation components will further escape this layer through the boundaries $z = H$ and $z = 0$, respectively. Since photons propagate through the gyroresonance layer and scatter there conserving their frequency in the laboratory frame ($\omega = \text{const}$), it is clear that the spatial boundaries of the flow do not affect upward radiation at frequencies

$$\begin{aligned}\omega_B[1 + (\beta(0)/2 + \beta_{T_\parallel}\xi_{\max}/\sqrt{2})] \lesssim \omega \\ \lesssim \omega_B[1 + (\beta(H)/2 - \beta_{T_\parallel}\xi_{\max}/\sqrt{2})]\end{aligned}$$

and downward radiation at frequencies

$$\begin{aligned}\omega_B[1 - (\beta(H)/2 - \beta_{T_\parallel}\xi_{\max}/\sqrt{2})] \lesssim \omega \\ \lesssim \omega_B[1 - (\beta(0)/2 + \beta_{T_\parallel}\xi_{\max}/\sqrt{2})].\end{aligned}$$

Note that, under the adopted approximations of a linear velocity profile (26) and rectangular line profile (27), the frequency ranges above can only exist for a sufficiently extended flow, in which

$$\frac{H}{L_\beta} \geq 2\sqrt{2}\xi_{\max}\frac{\beta_{T_\parallel}}{\beta_0}. \tag{35}$$

By analogy with the results of numerical calculations in the theory of moving stellar envelopes, we can assert that, if the strong inequality

$$H/L_\beta \gg 2\sqrt{2}\xi_{\max}\frac{\beta_{T_\parallel}}{\beta_0} \tag{36}$$

(cf. (9)) is satisfied, formulas (23) and (24) describe the outgoing radiation with sufficient accuracy in the case of a Gaussian line profile. The hatching with a different slope in Fig. 1 shows regions where the boundaries strongly affect radiation transfer in various directions. Using this figure, it is not difficult to see that the effective optical depth of the flow along the line $\omega = \text{const}$ in the intervals (31) and (32) increases monotonically from 0 to τ_β with increasing frequency ω. The same optical depth in the intervals (33) and (34) decreases monotonically from τ_β to 0. Therefore, the radiation intensity at frequencies at which the influence of the boundaries is strong varies from the level determined by (23) and (24) up to the intensity of the incoming radiation $I^{\text{inc}}(\omega, \alpha)$.

In conclusion, we should comment on the validity conditions for the solution obtained in the previous section. Equation (10), whose solution is given by (23) and (24), was obtained from (7) by omitting the term corresponding to spatial transfer of the radiation. Using the solution of (10) in the gyroresonance layer, which is not given here for the sake of brevity, we compare the two terms in the transfer operator:

$$\left(\frac{\partial I_{11}}{\partial z}\right)\left(\frac{1}{\sqrt{2}\beta_{T_\parallel}}\frac{\partial\beta}{\partial z}\frac{\partial I_{11}}{\partial\xi}\right)^{-1}$$

$$\sim \frac{e^{\xi^2}\sqrt{\pi/2}}{1+\tau_\beta}\frac{\beta_{T_\parallel}}{\beta}L_\beta(L_N^{-1} + L_\beta^{-1} + L_{L_\beta}^{-1}).$$

Here, we have taken into account that $\tau_\beta^{-1}|\partial\tau_\beta/\partial z| = L_N^{-1} + L_\beta^{-1} + L_{L_\beta}^{-1}$, where L_β, $L_{L_\beta} = L_\beta|\partial L_\beta/\partial z|^{-1}$, $L_N = N|\partial N/\partial z|^{-1}$ are the characteristic scales for β, L_β, and N, respectively. The resulting estimate shows that the ratio of the two terms in the transfer operator is much less than unity if

$$\beta_{T_\parallel}(L_N^{-1} + L_\beta^{-1} + L_{L_\beta}^{-1}) \ll \frac{\beta}{L_\beta}. \tag{37}$$

Taking (36) into account, we thus have the following validity condition for the solution (23) and (24):

$$\left|\frac{\partial\beta}{\partial z}\right| \gg \frac{\beta_{T_\parallel}}{\min(H, L_N, L_\beta, L_{L_\beta})}. \tag{38}$$

According to this criterion, the limiting case of large gradients holds if the variation in the flow velocity over the minimum scale for inhomogeneity is much greater than the thermal velocity of the electrons.

In this paper, we have considered a plasma flow in a homogeneous magnetic field. Using the results obtained here and in [13], we can easily derive the equation for cyclotron scattering in a plasma moving along the field lines of an inhomogeneous magnetic field:

$$\cos\alpha\frac{\partial I_{11}(z,\xi,\alpha)}{\partial z}-\frac{1}{\sqrt{2}\beta_{T_\parallel}}$$
$$\times\left(\cos\alpha\frac{\partial\beta}{\partial z}+\frac{1}{\omega_B}\frac{\partial\omega_B}{\partial z}\right)\frac{\partial I_{11}(z,\xi,\alpha)}{\partial\xi} \qquad (39)$$
$$=-\chi_{11}(z,\xi,\alpha)[I_{11}(z,\xi,\alpha)-S_1(z,\xi)].$$

Analysis of this equation is beyond the scope of this paper. We point out only the condition under which the effect of the plasma motion on the cyclotron radiation transfer dominates over the influence of the inhomogeneity of the magnetic field. This condition can be obtained by comparing the second term in (39), which can be estimated by the last formula in (8), and the third term, which can be estimated [13]

$$\frac{1}{\sqrt{2}\beta_{T_\parallel}\omega_B}\frac{\partial\omega_B}{\partial z}\frac{\partial I_{11}(z,\xi,\alpha)}{\partial\xi}\sim\frac{I_{11}}{\beta_{T_\parallel}L_B},$$

where $L_B=|\omega_B(d\omega_B/dz)|^{-1}$ is the characteristic scale for the magnetic field. Thus, the desired criterion has the form

$$L_\beta/L_B\ll\beta, \qquad (40)$$

which means that the Doppler frequency shift $\Delta\omega_\beta\sim\omega_B\Delta\beta$ due to the variation $\Delta\beta\sim|d\beta/dz|\beta_{T_\parallel}L_B=(\beta/L_\beta)\beta_{T_\parallel}L_B$ in the flow velocity over the scale $\beta_{T_\parallel}L_B$ of the gyroresonance layer in an inhomogeneous magnetic field must be much larger than the width of the cyclotron line $\beta_{T_\parallel}\omega_B$. In this case, plasma motion is certainly the dominant factor influencing cyclotron scattering, while the inhomogeneity of the magnetic field can be neglected.

The results obtained in this paper will be used to develop a theory for plasma flows driven by cyclotron radiation pressure in the vicinity of magnetic degenerate stars, and to calculate the influence of such flows on the observed spectra of these objects. These issues will be discussed in future publications.

ACKNOWLEDGMENTS

This work was supported by the Russian Foundation for Basic Research (project no. 93-3008).

REFERENCES

1. G. W. Clark, J. W. Woo, F. Nagase, *et al.*, Astrophys. J. **353**, 274 (1990).
2. M. Cropper, Space Sci. Rev. **54**, 195 (1990).
3. W. H. G. Lewin, J. van Paradijs, and R. E. Taam, Space Sci. Rev. **62**, 223 (1993).
4. V. V. Zheleznyakov and A. A. Litvinchuk, Astron. Zh. **64**, 306 (1987) [Sov. Astron. **31**, 159 (1987)].
5. G. S. Miller, R. I. Epstein, J. P. Nolta, and E. E. Fenimore, Phys. Rev. Lett. **66**, 1395 (1991).
6. V. V. Zheleznyakov and A. V. Serber, Pis'ma Astron. Zh. **17** (5), 419 (1991) [Sov. Astron. Lett. **17**, 179 (1991)].
7. V. V. Zheleznyakov and A. V. Serber, Space Sci. Rev. **68**, 275 (1994).
8. V. V. Sobolev, *Moving Stellar Envelopes* [in Russian] (Leningrad. Gos. Univ., Leningrad, 1947).
9. D. Mihalas, *Stellar Atmospheres* (Freeman, San Francisco, 1978; Mir, Moscow, 1982).
10. V. V. Zheleznyakov, Astrophys. Space Sci. **97**, 229 (1983).
11. V. V. Zheleznyakov and A. A. Litvinchuk, Astrophys. Space Sci. **105**, 73 (1984).
12. A. V. Serber, Astron. Zh. **67**, 582 (1990) [Sov. Astron. **34**, 291 (1990)].
13. V. V. Zheleznyakov and A. A. Litvinchuk, in *Proceedings of the Joint Varenna-Abastumani International School and Workshop on Plasma Astrophysics* (ESA, Noordwijk, 1986), ESA SP-251, p. 375.
14. A. A. Litvinchuk, Astron. Zh. **65**, 488 (1988) [Sov. Astron. **32**, 249 (1988)].
15. G. Schmidt, in *IAU Coll. 114: White Dwarfs* (Springer, Berlin, 1989), p. 305.
16. G. W. Clark, J. W. Woo, F. Nagase, *et al.*, Astrophys. J. **353**, 274 (1990).
17. T. Mihara, K. Makishima, T. Ohashi, *et al.*, Nature **346**, 250 (1990).
18. V. V. Sobolev, *Course of Theoretical Astrophysics* (Nauka, Moscow, 1985).
19. V. V. Zheleznyakov, Astrofizika **16**, 539 (1980).
20. A. V. Serber, *Cand. Sci. Dissertation (Phys.–Math.)*, Nizhniĭ Novgorod, 1998.
21. S. Chandrasekhar, Rev. Mod. Phys. **17**, 138 (1945).
22. L. B. Lucy, Astrophys. J. **163**, 95 (1971).
23. V. V. Zheleznyakov, *Radiation in Astrophysical Plasma* (Yanus-K, Moscow, 1997).

Translated by A. Serber

Astronomy Reports, Vol. 44, No. 12, 2000, pp. 825–829. Translated from Astronomicheskiĭ Zhurnal, Vol. 77, No. 12, 2000, pp. 934–939.

The Nitrate Content of Greenland Ice and Solar Activity

G. E. Kocharov[1], I. V. Kudryavtsev[1], M. G. Ogurtsov[1], E. Sonninen[2], and H. Jungner[2]

[1]*Ioffe Physicotechnical Institute, St. Petersburg, Russia;*
e-mail: Grant.Kocharov@pop.ioffe.rssi.ru

[2]*University of Helsinki, Helsinki, Finland*

Received December 3, 1999

Abstract—Past solar activity is studied based on analysis of data on the nitrate content of Greenland ice in the period from 1576–1991. Hundred-year (over the entire period) and quasi-five-year (in the middle of the 18th century) variations in the nitrate content are detected. These reflect the secular solar-activity cycle and cyclicity in the flare activity of the Sun. © *2000 MAIK "Nauka/Interperiodica".*

1. INTRODUCTION

Studies of solar activity on long time scales are not only important from the point of view of specific questions in solar–terrestrial physics (perturbations in the ionosphere and geomagnetic field, radiation conditions in near-Earth space), but also present astrophysical interest. The Sun is the most accessible source of information about the activity of stars in general and possible time evolution in this activity. New and interesting results have been obtained in this field in recent years: cyclicity has been detected in a number of solar-type stars, while others appear to be in a quiescent state similar to the Maunder minimum in the solar activity [1].

Understanding the nature of solar and stellar cyclicity requires data on long time intervals. However, the most extensive instrumental observations—measurements of the sunspot number—cover only slightly more than the last 250 years. One source of information about the behavior of the Sun over longer time intervals are "natural archives" of solar activity. One of these is polar ice, whose nitrate content carries quantitative information about solar activity in the past [2]. Nitrates, i.e. NO_3^-, are generated in the upper layers of the atmosphere under the action of ionizing cosmic radiation, as a result of a chain of reactions for which the raw material is NO (see, for example, [3]). Nitrogen oxide, in turn, forms via the dissociation of molecular nitrogen under the action of particle fluxes (Galactic cosmic rays, solar-flare protons) and short-wavelength solar radiation, as in the reaction

$$N_2O + O \longrightarrow 2NO. \quad (1)$$

Nitrogen oxide N_2O enters the atmosphere as the result of dentrification of soil and nitrogen fertilizers and burning of fuel. After its formation in the atmosphere, the NO_3^- ion becomes hydrated (the hydration rate depends appreciably on the temperature), binds to aerosols, precipitates, and is finally trapped in the polar ice. Consequently, a whole series of cosmic, climatic, and anthropogenic factors affect the formation of the final nitrate "imprint," including the intensity of Galactic cosmic rays and solar-flare protons. The solar-flare rate is itself one indicator of solar activity, and the modulation of the flux of Galactic cosmic rays by solar activity is also well known. Thus, to reconstruct the behavior of the Sun in the past, we must first isolate these two solar components from the overall nitrate signal.

The data used here were obtained by Dreschoff and Zeller [2]. Figure 1a presents a time series of the yearly-averaged nitrate content in the ice of central Greenland (73° N latitude, 48° W longitude) covering the period from 1576–1991. Dating of the ice samples was based on analysis of seasonal variations in the nitrate concentration and data on volcanic eruptions. Since each volcanic eruption leads to the ejection of a substantial quantity of sulfate into the atmosphere, the electrical conductivity of the corresponding ice layer increases. Therefore, joint analysis of measurements of the electrical conductivity and nitrate concentration of ice samples can provide the needed set of temporal markers. The final mean accuracy for the dating was two years. This paper is dedicated to a statistical analysis of the resulting time series aimed at deriving information about the behavior of the Sun in the past.

2. METHODS

We attacked the problem at hand via spectral analysis of the nitrate signal and its time dependence, as well as comparison of various independent data series. We determined the spectral composition of the nitrate series using wavelet transforms. In contrast to Fourier transforms, in which a studied signal is decomposed into an infinite number of sinusoidal harmonics, in wavelet analysis, the signal is decomposed into wavelets—self-similar functions localized in both frequency and time [4, 5]. Thanks to this property, wavelet-transform analyses are suitable for studies of non-stationary

1063-7729/00/4412-0825$20.00

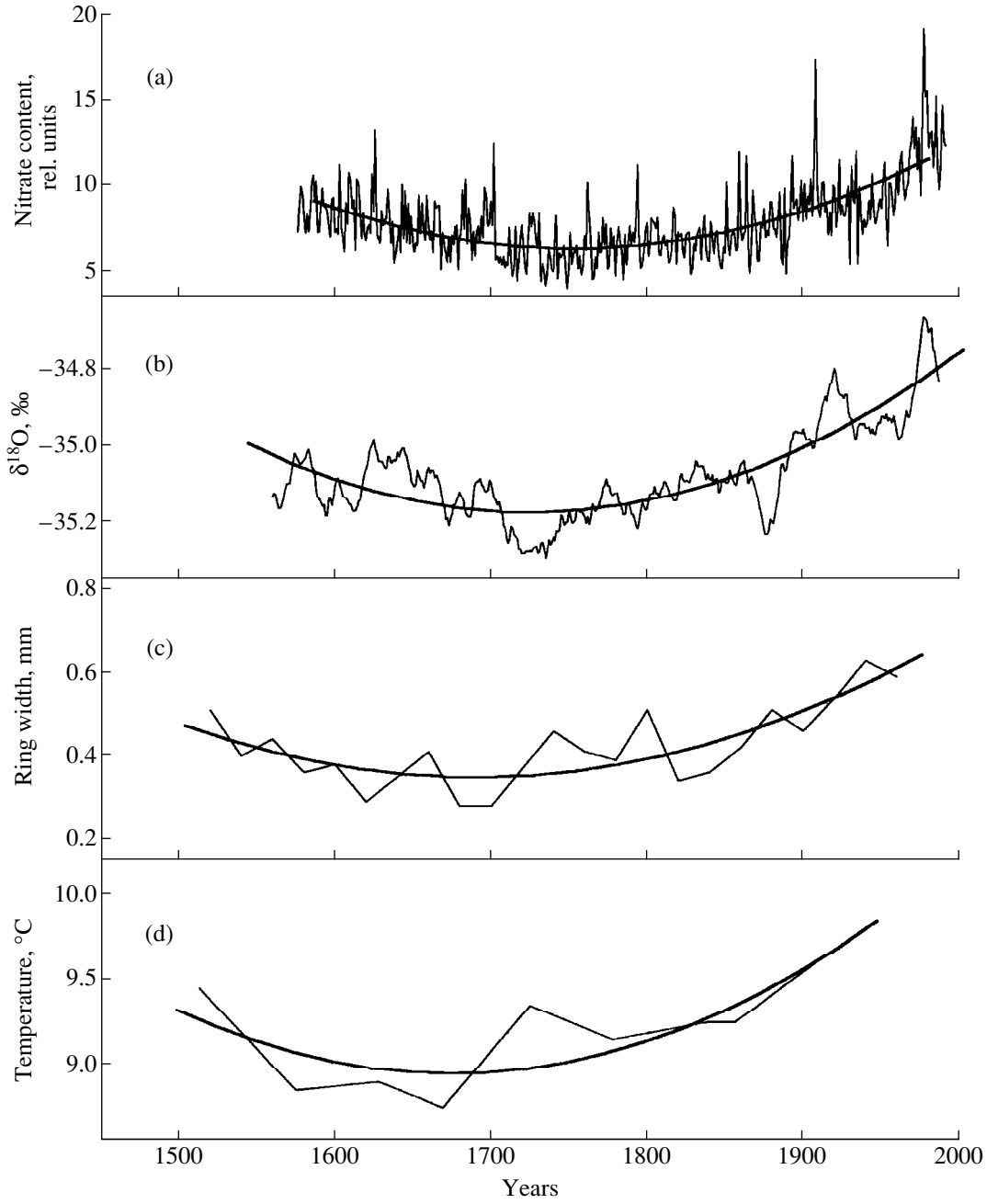

Fig. 1. (a) Nitrate content in Greenland ice, (b) ^{18}O content in Greenland ice, (c) ring widths for Californian trees, and (d) yearly-average temperatures in central England.

series. The coefficient $w(a, t)$ of the wavelet-transform function $f(t)$ is subject to analysis:

$$w(a,t) = a^{-1/2}\int_{-\infty}^{+\infty} f(t')\psi^*\left(\frac{t-t'}{a}\right)dt, \qquad (2)$$

where a is a scaling parameter, $\Psi(t)$ the analyzing wavelet, and t the current position of the analyzing wavelet. We used the complex wavelet of Morley

$$\psi_{\text{Morle}} = \exp(-x^2/2)\exp(-ik_0x) \qquad (3)$$

(with k_0 taken to be 6.0 [5]) and the real MHAT wavelet

$$\psi_{\text{MHAT}} = \exp(-x^2/2)(1-x^2). \qquad (4)$$

The wavelet transform yielded a set of coefficients $w(a, t)$ that can be presented in a three-dimensional dia-

gram in which the X axis plots the position of the analyzing wavelet t, the Y axis plots the time scale a, and the Z axis plots $w(a, t)$. We depicted this diagram (wavelet spectrum) using a grey-scale, where the intensity reflects the value of $w(a, t)$. When using the MHAT wavelet, the magnitude of $w(a, t)$ reflects the correlation of the wavelet and the studied signal. If the correlation is positive, $w(a, t) > 0$ and these regions in the spectrum are dark; if the correlation is negative, $w(a, t) < 0$ and the corresponding regions are light.

The MHAT wavelet is most convenient for detecting local temporal inhomogeneities in a signal. When using the complex Morley wavelet with $k_0 = 6.0$, the quantity $|w(a, t)|$ is proportional to the amplitude of variations in the studied signal with period $2a \times 1.03$ at time t [5]. Application of the Morley basis makes it possible to track the evolution of the signal spectrum in time.

Here, we used the normalized wavelet spectra

$$w^N(a, t) = w(a, t)a^{-1/2}. \quad (5)$$

This normalization is convenient because, for a sinusoidal signal with amplitude A_{mp}, the amplitude of the transform $w^N(a, t)$ proportional to A_{mp}. This means that, when using the real MHAT basis, the value $w^N(a, t)$ proportional to the deviation from zero of the current signal at time t on time scale a. When applying the complex Morley basis, the quantity $|w^N(a, t)|$ is proportional to the amplitude of the corresponding periodicity at time t. The real part of the wavelet transform (which coincides with the wavelet transform itself in the case of the MHAT basis) can also be used as a filter [5].

3. RESULTS

The limitations of the nitrate series prevent us from effectively applying the wavelet method to analyze variations with periods of more than 120–150 years, since the Morley basis has an appreciable region of influence. Therefore, we searched for periodicities in the nitrate signal with periods of less than 130 years.

Figure 2 presents the wavelet spectrum obtained using the Morley basis. We can see that, among the short-period ($T < 30$ yr) variations in the nitrate concentration, a 4–7-year mode dominates (most clearly expressed in the second half of the 19th century). In the low-frequency part of the spectrum ($30 < T < 130$ yrs), variations with a period of 80–100 yr outside the region of influence can clearly be seen. Let us consider these periodicities in more detail.

It was shown in [6, 7] that the (4–7)-year cyclicity is most probably associated with the flare activity of the Sun. It is now known that, as a rule, short-time scale peaks in the nitrate concentration are due to solar flares—powerful proton events [8]; with the exception of the last four solar-activity cycles, solar proton events occur most often at the phases of growth and decay in the sunspot number [9]. Therefore, a correlation between nitrate peaks and periods of growth and decay of the 11-year solar-activity cycle could generate variations in the nitrate concentration with periods that are close to half the 11-year period, i.e., about 5.5 yrs.

Evidence in favor of this hypothesis and the reality of a connection between the number of flares and periods of growth and decay of solar activity over more than the last 200 years was obtained in [7, 8]. To illustrate the phase relation between short-time scale variations in the nitrate concentration and solar activity, Fig. 3 presents the nitrate data together with data on the number of sunspot groups [10] in the middle and second half of the 19th century, when quasi-five-year variations were manifest most distinctly. The coincidence of many of the nitrate peaks with periods of growth and decay in the solar activity can clearly be seen in this figure. Note that additional theoretical study is necessary to establish a quantitative relation between the nitrate content in polar ices and solar flares.

Further, we considered the (80–100)-year periodicity. The known secular cycle of the solar activity established by Gleissberg [11] immediately arises as a possible origin for these variations. We first estimated the significance of this variation, for which we performed a classical spectral analysis. Figure 4 shows the spectrum of the nitrate signal obtained using a maximum-entropy method after the subtraction of a second-order polynomial trend (this trend, which has a bowl-like shape, describes the long-term behavior of the nitrate concentration; as we will show below, it is most likely not directly connected with solar activity). A peak corresponding to a period of 103.4 yrs is very prominent. Based on the statistics of the experiment, the significance of this peak (the probability that it does not correspond to a white-noise peak) is 0.99.

To elucidate the phase relation between the secular cycles in the nitrate content and in the solar activity, we compared the 100-year wavelet components for both signals obtained using the MHAT basis for 1700–1990. These components are presented in Fig. 5, which clear shows a rather stable negative correlation between the secular variations in the nitrate concentration and solar activity. The high significance of the 100-year nitrate periodicity and its negative correlation with the solar cycle established by Gleissberg [11] make it possible to use the nitrate "record" as an indicator of secular oscillations in the solar activity in the epoch prior to instrumental measurements.

In addition to these periodicities, we should consider the long-term trend in the nitrate series (Fig. 1a). As already noted, this trend has a bowl-like shape. The bottom of the bowl (minimum mean nitrate concentration) occurs in the first half of the 18th century. An appreciable rise is seen starting from the beginning of the 19th century. A somewhat weaker rise in the trend is observed before the start of the 18th century. In our opinion, the decrease in the trend before the middle of the 18th century has a climatic origin, and the rise at the beginning of the 19th century is a consequence of climatic variations and anthropogenic influences. Arguments in favor of this hypothesis include the following.

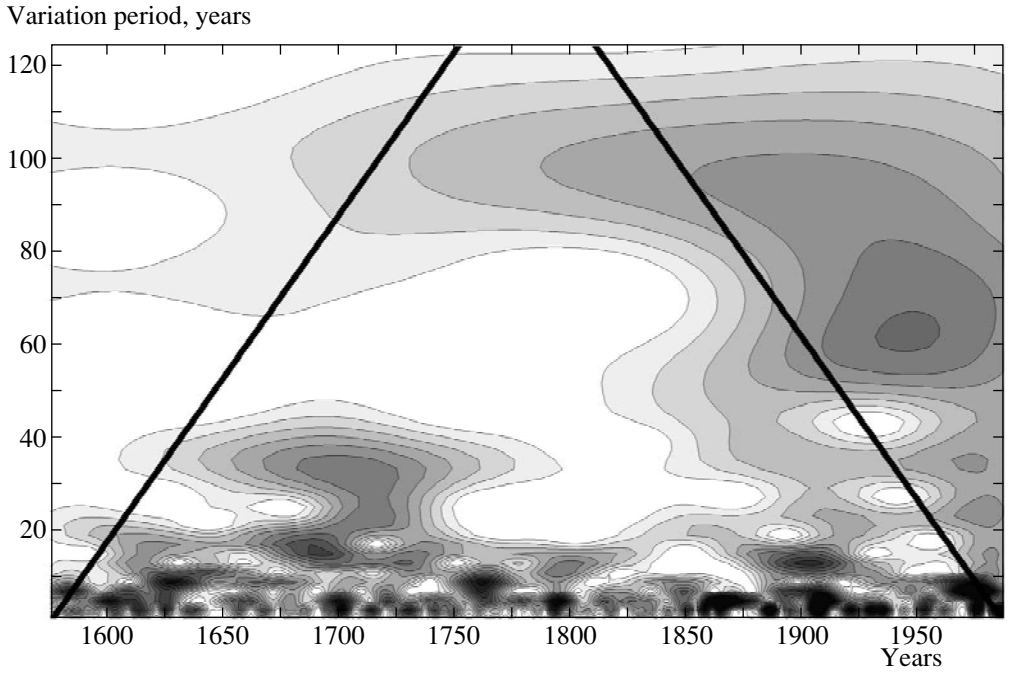

Fig. 2. Wavelet spectrum $w^N(a, t)$ for the nitrate concentration in Greenland ice (the solid lines indicate the boundary of the region of influence). Black areas are those where $w^N(a, t) > 12.0$ and white areas are those where $w^N(a, t) < 2.0$.

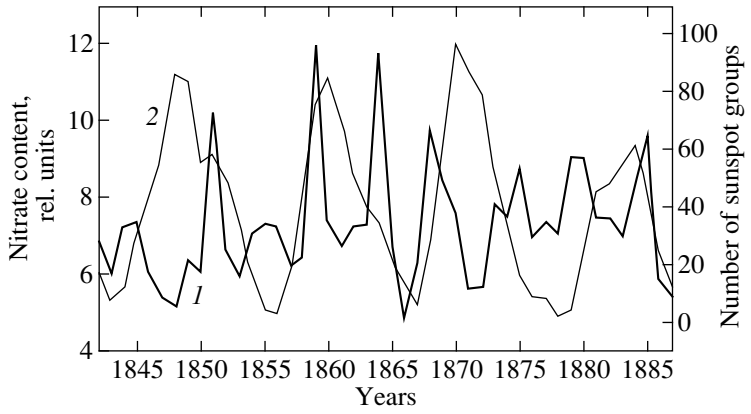

Fig. 3. Nitrate content in Greenland ice (curve *1*) and number of sunspot groups (curve *2*) in the middle and second half of the 19th century.

(1) The run of the long-term trend in the nitrate concentration bears some similarity to the behavior of other climatic trends. Figures 1b–1d present 100-yearly-averaged data on the content of the stable isotope of oxygen $\delta^{18}O$ in the Greenland ice [12], which reflects variations in the local temperature; data on the widths of rings of Californian pines, taken in [13] as a temperature indicator; and reconstructed temperatures in central England during the pre-instrumental epoch [14]. We can see that the long-term trends in these series, which reflect various climatic variations, have properties in common with the nitrate trend:

(a) a strong rise after the beginning of the 19th century and a weaker rise in the first part of the 17th century and

(b) minima in the second part of the 17th century and the first part of the 18th century (these minima are the result of a general cooling in the northern hemisphere—the so-called "little ice-age," from 1510–1730 [15]).

(2) The increasing addition into the atmosphere of nitrogen oxides as a result of anthropogenic activity [16, 17] leads to a growth in the rate of generation of the NO_3^- ion under the action of cosmic ionizing radiation [2]. This brings about an additional rise in the nitrate trend.

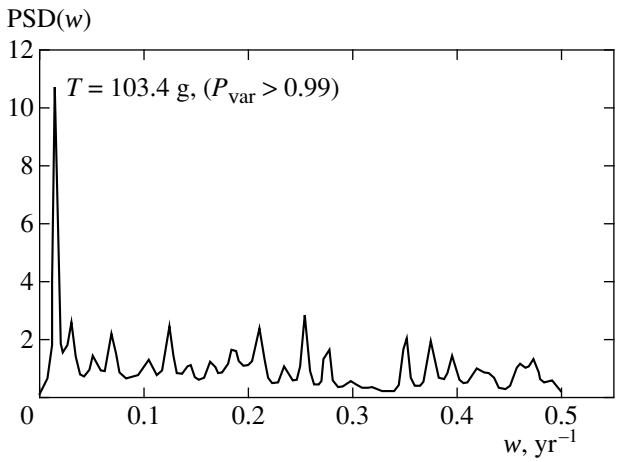

Fig. 4. Spectrum of filtered (via subtraction of a second-order trend) data on nitrate concentrations in Greenland ice obtained using a maximum entropy method (P_{var} is the significance of the peak).

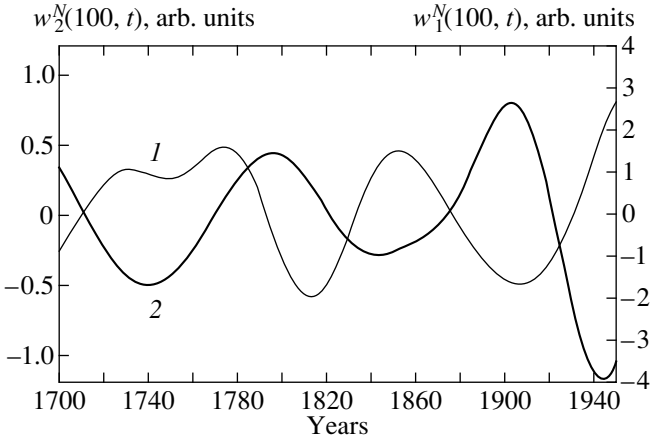

Fig. 5. 100-year wavelet components for the number of sunspot groups $w_1^N(100, t)$ (curve *1*) and nitrate concentrations in Greenland ice $w_2^N(100, t)$ (curve *2*).

Thus, the available results suggest that the long-term (period clearly exceeding the observing interval) nitrate trend is not related to solar activity, at least not directly, and is due first and foremost to climatic conditions.

4. CONCLUSION

Our statistical analysis of yearly-averaged data on the nitrate concentration in Greenland ice has demonstrated that these data contain valuable information about solar activity in the past. The nitrate series shows that there has periodically arisen a connection between the rate of solar flares and phases of growth and decay of solar activity over at least the last 200 years. The nitrate "record" also reflects the secular cycle of solar activity.

This demonstrates the fundamental possibility of using nitrate concentrations to reconstruct long-term ($T \sim 100$ yr) oscillations in the activity of the Sun, including global minima in activity. These properties make studies of polar-ice nitrate concentrations very promising from the point of view of the paleoastrophysics of the Sun. However, in further analyses of solar activity based on nitrate data, it will be important to take into account the influence of climatic variations on the formation of nitrates and their accumulation in polar ices.

ACKNOWLEDGMENTS

The authors consider it a pleasant obligation to thank G.A.M. Dreschoff for kindly presenting us with his unique data, A.A. Boyarchuk for his attention to this work, and Yu.A. Nagovitsyn for numerous pieces of useful advice. This work was supported by the Russian Foundation for Basic Research (project code 99-02-18398) and the Finnish Academy of Sciences.

REFERENCES

1. E. Nesme-Ribes, D. Baliunas, and D. Sokoloff, Sci. Am. **275**, 30 (1996).
2. G. A. Dreschoff and E. J. Zeller, in *TER-QUA Symposium Series*, Ed. by D. Wakeffield (Nebraska Academy Sciences, 1994), Vol. 2, p. 1.
3. G. A. Dreschoff, K. A. Boyarchuk, H. Jungner, *et al.*, in *Proceedings of the 26th International Cosmic Ray Conference 1999*, Vol. 4, p. 318.
4. N. M. Astaf'eva, Usp. Fiz. Nauk **166**, 1145 (1996) [Phys. Usp. **39**, 1085 (1996)].
5. Ch. Torrence and G. P. Compe, Bull. Am. Meteorol. Soc. **79**, 61 (1998).
6. G. E. Kocharov and M. G. Ogurtsov, Izv. Ross. Akad. Nauk, Ser. Fiz. **63** (8), 16 (1999).
7. G. E. Kocharov, M. G. Ogurtsov, and G. A. Dreschhoff, Sol. Phys. **188** (1), 187 (1999).
8. G. A. Dreschhoff and E. J. Zeller, in *Proceedings of the 24th International Cosmic Ray Conference 1995*, Vol. 4, p. 1196.
9. M. A. Shea and S. D. Smart, Adv. Space Res. **16**, 37 (1995).
10. D. V. Hoyt and K. H. Schatten, Sol. Phys. **179**, 189 (1998).
11. W. Gleissberg, Terr. Magn. Atmos. Electr. **49**, 243 (1944).
12. M. Stuiver, P. M. Grootes, and T. F. Braziunas, Quaternary Research **44**, 341 (1995).
13. V. C. LaMarche, Jr., Science **183**, 1043 (1974).
14. H. H. Lamb and J. M. Mitchell, Jr., Ann. (NY) Acad. Sci. **95**, 235 (1961).
15. R. S. Bradley and P. D. Jones, Holocene **3**, 367 (1993).
16. M. I. Budyko and Yu. A. Izraél', in *Anthropogenic Climate Changes* [in Russian] (Gidrometeoizdat, Leningrad, 1987).
17. P. A. Mayewski, W. B. Lyons, M. S. Spencer, *et al.*, Nature **346**, 554 (1990).

Translated by D. Gabuzda

Astronomy Reports, Vol. 44, No. 12, 2000, pp. 830–832. Translated from Astronomicheskiĭ Zhurnal, Vol. 77, No. 12, 2000, pp. 940–943.

Influence of a Sunspot Penumbra on the Oscillatory Regime of Neighboring Regions

N. I. Kobanov

Institute for Solar-Terrestrial Physics, P.O. Box 4026, Irkutsk, 664033 Russia

Received March 3, 1999

Abstract—The spectra of radial-velocity oscillations in the immediate vicinity of a sunspot beyond the observable boundary of the penumbra have been analyzed. The radial velocities were derived using a differential method. The oscillation spectra at two heights (lower photosphere and chromosphere) were compared with reference spectra for the middle penumbra and an unperturbed region obtained using the same method. The oscillatory regime characteristic of the sunspot penumbra extends more than 15″ beyond its observable boundary. It is proposed that deep photospheric layers in the region surrounding the penumbra have physical conditions similar to those observed inside its outer boundary. © *2000 MAIK "Nauka/Interperiodica".*

1. INTRODUCTION

The dynamical processes in sunspot penumbrae have been widely studied in recent years. One of the most remarkable phenomena in penumbrae are Evershed flows, currently believed to be horizontal flows directed radially from the sunspot umbra at the photospheric level and concentrated in dark filaments [1, 2]. The magnetic field in these filaments is approximately horizontal, and resembles a ribbed surface [2, 3]. The channels of photospheric Evershed flows have narrow cross sections and occupy a thin layer in height [1, 4]. The horizontal magnetic field and powerful Evershed flows are the main factors determining the character of wave motions in penumbrae.

One of the most controversial questions is the true radial extent of Evershed flows from the geometric center of a sunspot. Borner and Kneer [5], Rimmele [6, 7], Solanki *et al.* [8, 9], and Stanchfield *et al.* [10] have suggested that such flows go beyond the outer boundaries of the penumbra observed in white light. On the other hand, Westendorp *et al.* [11] note that Evershed flows disappear abruptly just beyond the observable boundary of penumbrae, and Lites [2], Schlichenmaier and Schmidt [4], and Wiehr and Degenhardt [12] maintain that these flows exist only inside this boundary. Hope for resolving this problem is offered by observations with very high spatial resolution (up to 0.5″). As a rule, the accuracy of radial-velocity measurements based on such observations does not exceed 100–150 m/s [4]. Such measurements often carry the imprints of individual features of observed fine-structure elements, making the overall pattern of the radial-velocity distribution in the sunspot penumbra extremely variegated. It is interesting that Rimmele [6, 7] and Schlichenmaier and Schmidt [4] obtained opposing results, although both papers were based on observations with high spatial resolution.

In our opinion, if we wish to reveal the most general features of the velocity field in a penumbra, high-resolution observations must be supplemented by measurements with moderate spatial resolution but better sensitivity (10–30 m/s). In some sense, this problem is similar to that of measuring solar magnetic fields.

2. THE METHOD

We consider the extent of Evershed flows from another point of view, by investigating the range of the influence of the penumbra on the oscillatory regime of the surrounding medium. It is known that the oscillation pattern in penumbrae in both the photosphere and chromosphere differs considerably from that in unperturbed regions. Clearly-expressed five-minute oscillations with amplitudes of up to 300–400 m/s in the photosphere and three-minute oscillations with amplitudes of 1–2 km/s in the chromosphere are characteristic of unperturbed regions, whereas periods of 10–12 and 7–8 min have been detected at both levels in penumbrae [6, 13, 14]. Even longer periods (35 min) have been observed in some sunspots [14], with amplitudes below 50 m/s in the lower photosphere and about 0.5 km/s in the chromosphere. Thus, both the spectra and amplitudes of oscillations in sunspot penumbrae are different from those in the unperturbed surrounding medium.

By observing radial-velocity oscillations in the vicinity of a penumbra and comparing their parameters with those for "standard" oscillatory spectra for penumbrae and the unperturbed solar atmosphere, it is possible to judge to which of these the physical conditions in the neighborhood of the penumbra are most similar. The differential method of [15] is very convenient for such analyses. This method makes it possible to separate out motions with a specified direction and spatial scale from a mixture of wave motions with various scales and directions. These parameters can be changed

1063-7729/00/4412-0830$20.00

in accordance with the dimension and configuration of the object studied. In addition, the real sensitivity of the measurements increases by more than an order of magnitude due to suppression of the internal noise in the spectrograph. All these properties are very valuable for measurements in penumbrae, where the velocity field is radially symmetric and oscillations are substantially suppressed by the horizontal magnetic field and "masked" by strong Evershed flows.

3. OBSERVATIONS AND RESULTS

Observations of the sort described above are most easily conducted for large sunspots with regular shapes located near the center of the solar disk. In July 1998, we observed the neighborhood of the penumbra of sunspot NOAA 8263. Figure 1 shows a schematic of the locations of the observed regions. Positions 1a, 2a, 3a, and 4a are separated from the apparent outer boundary of the penumbra by 10″, and positions 1b, 3b, and 4b by 20″. The observations for position 2b were corrupted for instrumental reasons and excluded from the analysis, so that this position is not presented in Fig. 1.

We detected the differential speeds of pairs of elements on the solar surface with sizes 1.5″ × 4″ separated by 6.5″ at each position. As reference spectra, we used (1) the spectrum of the radial-velocity oscillations in the middle of the NOAA 8263 penumbra, obtained by averaging three spectra corresponding to different points of the penumbra (Fig. 2a), and (2) the oscillation spectrum for an unperturbed region 200″ from the sunspot (Fig. 2d). The observations were carried out on the 80-cm telescope of the Sayany Observatory, equipped with a guiding system and a device for image rotation. The drift of the image due to the solar rotation was compensated by slow scanning in the same direction. The observations were conducted in the H_β line (for the chromosphere) and in the far wing of the Ni I 4857.2 Å line (for the lower photosphere).

Power spectra were computed via a standard fast Fourier transform preceded by smoothing at the ends of the time series. The spectra of the radial-velocity oscillations at the photospheric level at positions 1a, 2a, 3a, and 4a correspond well to the standard penumbra spectrum (Fig. 2a), both individually and as an average (Fig. 2b). There are clearly-expressed periods of 8 and 10–12 min in the spectra, while the power of the five-minute oscillations is decreased. The shape of the average spectrum for positions 1b, 3b, and 4b (Fig. 2c) is more similar to the spectrum for the unperturbed photosphere than that for the penumbra, although the individual spectrum for position 3b still contains a significant 8-min maximum (Fig. 3). For comparison, the individual spectrum for position 3a is also presented in Fig. 3.

The spectra for positions 1a, 2a, 3a, and 4a at the chromospheric level are in satisfactory agreement with the standard penumbra spectrum. Three-minute oscillations are suppressed, whereas (8–10)-min oscillations

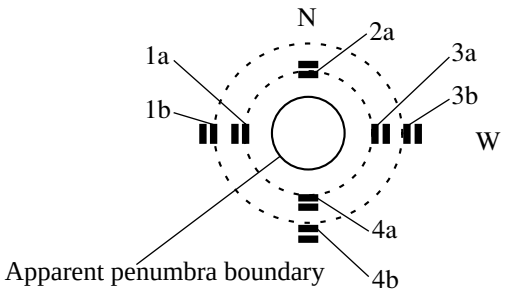

Fig. 1. Schematic of observations in the neighborhood of the penumbra of sunspot NOAA 8263.

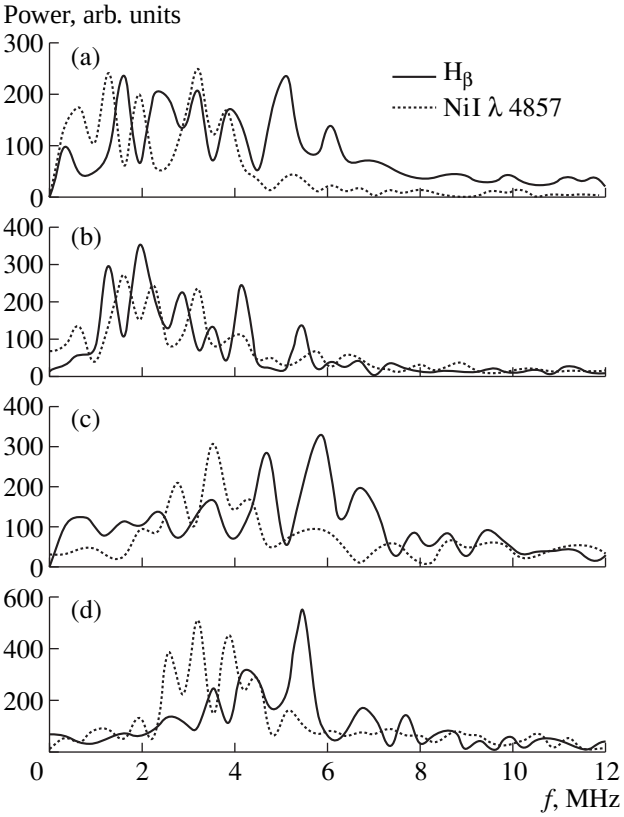

Fig. 2. Radial-velocity power spectra derived from differential observations (a) in the middle penumbra of sunspot NOAA 8263 (the standard penumbra spectrum), (b) in the near (10″) vicinity of the penumbra, (c) far (20″) from the penumbra, and (d) in an unperturbed region.

dominate. For increased clarity, the amplitudes of the photospheric power spectra have been multiplied by a factor of from three to five in most of the figures, so that the scales along the vertical axes are arbitrary.

The above results were confirmed by a correlation analysis, used to compare the spectral composition of the oscillations. Prior to calculating the correlations of the power spectra, they were smoothed using a moving average over three points. The power spectra for the differential radial velocity measured in the near vicinity of

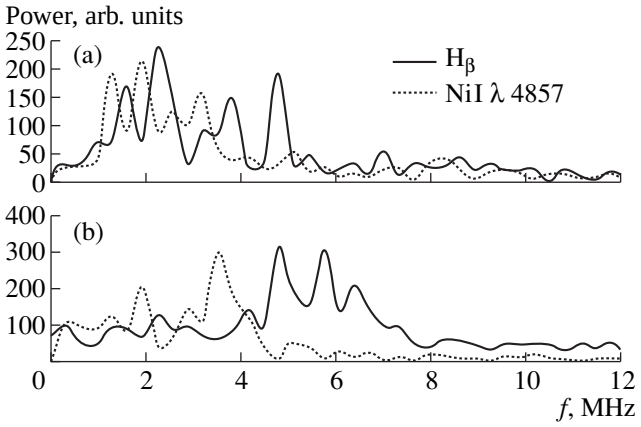

Fig. 3. Individual radial-velocity power spectra for positions (a) 3a and (b) 3b, with the same notation as in Fig. 1.

the penumbra (Fig. 2b) and the standard penumbra spectrum have correlation coefficients of 0.84 at the photospheric level and 0.7 at the chromospheric level. On the other hand, the corresponding correlation coefficients for the spectra in the near vicinity of the penumbra and in the unperturbed region are 0.4 and 0.03, respectively. The correlation coefficients for the distant region (Fig. 2c) and the standard penumbra spectrum are 0.46 and 0.49, and for the distant region and the unperturbed region are 0.9 and 0.7.

To obtain a more complete picture, we intend in future studies to make observations of variations of the profiles of the H_β and Ni I 4857.2 Å lines in the vicinity of the penumbra. Oscillations of these profiles with a period of about 8 min have been noted in previous studies as characteristic of the inner penumbra [16].

4. CONCLUSIONS

The oscillatory regime characterizing the sunspot penumbra can be observed to distances of about 15″ from the apparent outer boundary of the penumbra, in both the photosphere and chromosphere. This has been reported here for the first time.

Note that the penumbra neighborhood under investigation is virtually indistinguishable from the surrounding unperturbed photosphere in white light. The detected oscillations probably carry information about subphotospheric layers, for which only a small fraction of the optical emission reaches the surface. In this sense, the method used can be considered helioseismological. Evidently, conditions preventing the establishment of the oscillatory regime characteristic of the unperturbed photosphere exist in the deep photospheric layers of the region surrounding the sunspot. It can reasonably be supposed that these conditions are similar to those in the vicinity of the penumbra. In other words, the extent of the penumbra indicated by its influence on oscillations of the surrounding medium is a factor of 1.5–2 greater than the extent observed in white light.

ACKNOWLEDGMENTS

This work was partially supported by the Program of State Support of Leading Scientific Schools of the Russian Federation (grant no. 96-15-96733) and the "Astronomy" State Science and Technology Program.

REFERENCES

1. D. Degenhardt and E. Weihr, Astron. Astrophys. **287**, 620 (1994).
2. B. W. Lites, in *Dynamics and Fine Structure of Sunspots*, Trans. IAU A, 23 (1997).
3. A. M. Title, Z. Frank, R. A. Shine, *et al.*, Astrophys. J. **403**, 780 (1993).
4. R. Schlichenmaier and W. Schmidt, Astron. Astrophys. **349**, L37 (1999).
5. P. Borner and F. Kneer, Astron. Astrophys. **259**, 307 (1992).
6. T. R. Rimmele, Astrophys. J. **445**, 511 (1995).
7. T. R. Rimmele, Astron. Astrophys. **298**, 260 (1995).
8. S. K. Solanki, C. A. P. Montavon, and W. Livingston, Astron. Astrophys. **283**, 221 (1994).
9. S. K. Solanki, W. Finsterle, I. Ruedi, and W. Livingston, Astron. Astrophys. **347**, L27 (1999).
10. D. C. Stanchfield, II, J. H. Thomas, and B. W. Lites, Astrophys. J. **447**, 485 (1997).
11. C. Westendorp Plaza, J. C. del Toro Iniesta, B. Rulz Cobo, *et al.*, Nature **387**, 47 (1997).
12. E. Wiehr and D. Degenhardt, Astron. Astrophys. **259**, 313 (1992).
13. B. W. Lites, in *Sunspots: Theory and Observations*, Ed. by J. H. Tomas and N. O. Weiss (Kluwer, Dordrecht, 1992).
14. N. I. Kobanov, Astron. Zh. **77**, 233 (2000) [Astron. Rep. **44**, 202 (2000)].
15. N. I. Kobanov, Astron. Astrophys. **143**, 99 (1985).
16. N. I. Kobanov, JOSO Annual Report, 1998, p. 118.

Translated by Yu. Dumin

Astronomy Reports, Vol. 44, No. 12, 2000, pp. 833–840. Translated from Astronomicheskiĭ Zhurnal, Vol. 77, No. 12, 2000, pp. 944–952.

Effect of Coulomb Losses on the Spectra of Heavy Particles Accelerated in Prolonged Solar Events

M. F. Stovpyuk and V. M. Ostryakov

St. Petersburg State Technical University, ul. Politekhnicheskaya 29, St. Petersburg, 195251 Russia

Received December 1, 1999

Abstract—This paper examines the possibility of using the energy spectra of accelerated solar cosmic-ray ions and features formed by Coulomb losses to study the solar plasma (the power-law index S for the scattering turbulence, particle number density N, and temperature T of the background medium). For an individual solar flare, Coulomb losses can be manifest to different degrees in the spectra of different ions, providing a means to determine S. A comparison of theoretical spectra for H, He, C, O, and Fe ions with observed spectra for the prolonged solar flare of October 20, 1995 yields $S \approx 3$, $N \approx 5 \times 10^9$ cm^{-3}, and $T \approx 10^6$ K, assuming that the characteristic time scale over which these particles gain energy is about a second. © *2000 MAIK "Nauka/Interperiodica".*

1. INTRODUCTION

In recent observational data, one can distinguish prolonged and impulsive solar flares. As a rule, prolonged flares are associated with the regular acceleration of charged particles by shocks [1, 2] and/or electric fields in current sheets (see, for example, [3, 4]), while impulsive flares are associated with stochastic acceleration via interactions with magnetic inhomogeneities [5]. The flares themselves can be classified via a number of features (see, for example, [6, 7]). For instance, in prolonged flares, the fluxes of accelerated protons are more intense than those of electrons. In addition, in the vast majority (~96%) of cases, prolonged events are associated with coronal mass ejections (CMEs). Therefore, particle acceleration can occur in shocks created by the CMEs moving toward the boundary of the heliosphere [8].

Here, we consider the acceleration of heavy ions at the fronts of parallel shocks forming in prolonged solar flares. In the absence of energy losses, the spectra formed by these processes exhibit a classical power law (see, for example, [9, 10]). However, energy losses can bring about deviations from the classical spectrum [11]. For stochastic acceleration, Coulomb losses can lead to the formation of spectral dips in narrow energy intervals [12–14]. Similar local decreases in intensity due to deceleration by background plasma particles can also occur in shock-acceleration spectra. It is possible to characterize the plasma of solar flares by using these features to estimate the number density, temperature, and magnetic field of the plasma, as well as the ratio of the total turbulent energy density to the energy of the regular magnetic field [14].

It was shown earlier [15] that, during the acceleration of multiply-charged ions in fairly dense plasmas, changes in the ion charges can occur more rapidly than the acceleration, and the formation of the charge and energy spectra must be considered simultaneously. Later, this problem was studied numerically, and observational data for a prolonged flare were fit [16] (for Fe ions). In turn, this made it possible to estimate the number density and temperature in the acceleration region using the charge distributions as a function of energy (mean charge, variance, asymmetry). However, these computations yield no clear evidence in favor of any particular power-law index for the scattering turbulence. We show here that analysis of features in the energy spectra produced by Coulomb losses can provide such evidence.

Note that, when modeling the acceleration of various ions, we take into account changes in the charges only of Fe ions. The charges of other ions (He, C, and O) are assumed to be constant, since they are close to their maximum values in the energy interval of interest to us (~1 MeV per nucleon), where Coulomb losses are manifest for typical flare plasma temperatures ~10^6 K [17]. Such temperatures apparently correspond to the impulsive phase of a flare (when the particle acceleration occurs), although, as shown by soft X-ray data, this temperature can grow by a factor of several tens with time.

2. FORMULATION OF THE PROBLEM

In the presence of diffusive acceleration by a parallel shock, particles gain energy via repeated intersections with the shock front and collisions with magnetic inhomogeneities frozen in the plasma. The velocities of these inhomogeneities $u(x)$ are different on either side

1063-7729/00/4412-0833$20.00

of the front (we consider a plane geometry in which the front is situated at $x = 0$):

$$u(x) = \begin{cases} u_1 = u_0, & x < 0 \\ u_2 = u_0 \dfrac{(\kappa - 1)M_1^2 + 2}{(\kappa + 1)M_1^2}, & x > 0, \end{cases}$$

where $M_1 = u_1/V_s$ is the Mach number, V_s the sound speed, and κ the ratio of specific heats. Let us use a stationary diffusion equation for ions of charge q and atomic mass A accelerated in front of ($i = 1$) and behind ($i = 2$) the shock front

$$\frac{\partial}{\partial x} D_i \frac{\partial}{\partial x} f - u_i \frac{\partial f}{\partial x} - \frac{\partial}{\partial E}\left(\frac{dE}{dt} f\right) = 0, \quad i = 1, 2, \quad (1)$$

where $f \equiv f(x, E)$ is the ion distribution. Here, D_i is the spatial diffusion coefficient, which depends on the energy E, charge q, and power-law index S for scattering in Alfvén turbulence with spectral density $W(k) = W_0 k^{-S}$ (see, for example, [9, 18, 19]):

$$D_i = D_{0i}\left(\frac{q}{A}\right)^{S-2} \begin{cases} E^{(3-S)/2}, & S < 2 \\ E^{1/2}, & S > 2 \end{cases} \quad i = 1, 2. \quad (2)$$

The power-law dependence $W(k)$ that gives rise to (2) is characteristic of many types of turbulence and, in particular, of Alfvén turbulence, which is apparently easily excited in solar-flare regions and is more weakly damped than magneto-acoustic pulsations [9]. The lower boundary of the interval of wave numbers k considered is determined by the scale length of the perturbation region (the coherence length), which, for flare plasma, can be taken to be $L_c \sim 6 \times 10^6$ cm ($k_{\min} = 2\pi/L_c \sim 10^{-6}$ cm^{-1}), which corresponds to a maximum energy for the accelerated particles of ~10 GeV [12, 20]. The upper boundary $k_{\max}$ is determined by cyclotron damping of the Alfvén waves in the plasma; $k_{\max} \sim \omega_{Bp}/V_a$ (ω_{Bp} is the proton gyrofrequency and V_a the Alfvén speed) does not play a significant role, since the main contribution from turbulent energy (for a falling spectrum) is contained on larger scales. In addition, the assumed injection energy $E_0 = 40$ keV/nucleon corresponds to resonant wave numbers $k_{\rm res} < k_{\max}$, which can easily be found using the plasma parameters in the acceleration region obtained in Section 3.

The last term in Eq. (1) takes into account ion energy losses during the acceleration. For example, Coulomb losses in a two-component plasma of electrons and protons yield [21]

$$\frac{d(E/A)}{dt} = -\frac{2\sqrt{2}\pi e^4}{\sqrt{m_e k_{\rm B} T_e}} \frac{q^2 \Lambda N}{A} \times \left[F\left(x_e, \frac{m_e}{M}\right) + \sqrt{\frac{m_e T_e}{m_p T_p}} F\left(x_p, \frac{m_p}{M}\right)\right], \quad (3)$$

where m_e, T_e and m_p, T_p are the masses and temperatures of the electrons and protons, respectively, $M = Am_p$ is the mass of an ion moving in the plasma, N is the plasma number density, and Λ is the Coulomb logarithm (we assume $\Lambda = 20$). The functions $F(x, \xi)$ are expressed in terms of the probability integral $\Phi(x) = \frac{2}{\sqrt{\pi}}\int_0^x e^{-t^2} dt$ and its derivative $\Phi'(x) = \frac{2}{\sqrt{\pi}} e^{-x^2}$:

$$F(x, \xi) = \frac{1}{x}\Phi(x) - (1 + \xi)\Phi'(x),$$

with their arguments being $x_e = \dfrac{V}{V_{Te}} = \sqrt{\dfrac{m_e}{M}\dfrac{E}{k_{\rm B} T_e}}$ and $x_p = \dfrac{V}{V_{Tp}} = \sqrt{\dfrac{m_p}{M}\dfrac{E}{k_{\rm B} T_p}}$. Further, we assume that $T_e = T_p \equiv T$. Note that, in the energy interval considered (0.04–20 MeV/nucleon), deceleration by electrons makes the main contribution to Coulomb losses. The maximum of these losses corresponds to an ion energy $\dfrac{E_{\max, e}}{A} \approx \dfrac{9}{4}\dfrac{m_p}{m_e} k_{\rm B} T$, while the maximum provided by interactions with protons corresponds to $\dfrac{E_{\max, p}}{A} \approx \dfrac{9}{4} k_{\rm B} T$, which creates an injection barrier only for acceleration from thermal energies [11, 21]. It is important that, when we express the energy in MeV per nucleon, the maximum losses for all types of ions virtually coincide.

We denote the particle distribution at the shock front f_0, which corresponds to the injection energy E_0. We also assume that the solution is bounded at infinity:

$$f|_{x \to \pm\infty} \text{ is bounded}, \quad (4)$$

and that the following conditions relating the distributions and particle fluxes at the shock front are satisfied:

$$f|_{x \to -0} = f|_{x \to +0}, \quad (5)$$

$$D_1 \frac{\partial f}{\partial x}\bigg|_{x \to -0} - D_2 \frac{\partial f}{\partial x}\bigg|_{x \to +0} = -\frac{2(u_1 - u_2)}{3} E \frac{\partial f}{\partial E}\bigg|_{x = 0} + \frac{(u_1 - u_2)}{3} f + Q_0 \left(\frac{E}{E_0}\right)^{-\alpha_0}. \quad (6)$$

This latter equation contains a source of particles that has a power-law dependence on energy. Such a source, allowing for the possibility of pre-acceleration (for example, stochastic), enables us to fit the observed spectra with different power-law indices at high and

low energies [16]. Indeed, in the absence of Coulomb losses, the solution is given by

$$f(E) = \left(f_0 - \frac{\alpha}{\alpha - \alpha_0}\frac{3Q_0}{(2u_1 + u_2)}\right)\left(\frac{E}{E_0}\right)^{-\alpha} + \frac{\alpha}{\alpha - \alpha_0}\frac{3Q_0}{(2u_1 + u_2)}\left(\frac{E}{E_0}\right)^{-\alpha_0}, \quad (7)$$

where $\alpha = \frac{2r+1}{2(r-1)}$ and r is the shock compression factor. We can see that, for $\alpha_0 > \alpha$ and energies close to the injection energy, the final stationary spectrum is less steep than the classical spectrum, represented by the first term in (7). Note also that the velocities of the magnetic inhomogeneities on either side of the shock front in Eq. (6) can, in general, differ from the corresponding hydrodynamic plasma velocities, indicating that the pulsations are not frozen in the flow [22]. Therefore, the compression factor for the scattering centers can significantly exceed four, leading to harder particle spectra. However, for the fairly high Alfvénic Mach numbers $M_a = u_1/V_a \geq 10$ and plasma parameters $\beta = (V_s/V_a)^2 \geq 10$ assumed here, the "frozen-in" condition remains valid, and the power-law index for the accelerated particles depends only on the hydrodynamic compression.

The problem formulation presented above is applicable for ions with a constant charge (their charge remains unchanged upon acceleration), such as ions experiencing maximum ionization. However, Fe ions accelerated in regions with sufficiently dense plasma in the solar corona can change their charge due to collisional ionization by thermal protons and electrons, as was shown in [16]. In this case, the acceleration of the newly created ions obeys Eqs. (1) and (2), but with another charge. We take this into account using a set of n equations of the form (1) that include all possible charge transitions, with n being the number of charge states considered. Obviously, we must also rewrite the remaining equations (3)–(6) for each Fe ion individually (see [16] for details).

The ratio of the acceleration time to the characteristic Coulomb-loss time is important for our analysis. It is clear that the higher this ratio, the more appreciable the effect of losses on the spectra. For an energy E, the acceleration time is [10]

$$t_a(E) = \frac{3}{2(u_1 - u_2)}\int_{E_0}^{E}\left(\frac{D_1}{u_1} + \frac{D_2}{u_2}\right)\frac{dE}{E}, \quad (8)$$

while we adopt for the characteristic Coulomb-loss time

$$t_c(E) = E\left(-\frac{d(E/A)}{dt}\right)^{-1}. \quad (9)$$

Then, using (2) and (3), we can obtain

$$\frac{t_a(E)}{t_c(E)} = q^S A^{1-S} NG(E/A, T) \equiv \Omega NG(E/A, T), \quad (10)$$

where, as noted above, the function $G(E/A, T)$ is nearly the same for all ions [its definition is evident from (3), (8), and (9)]. Thus, the dependence of the Coulomb losses on S can have different strengths in ion spectra with different A and q. This means that, during a single event, the characteristic dips produced by Coulomb losses can be observed in the spectra of some elements but be absent in the spectra of others. We will present some examples in the next section.

3. COMPARISON WITH OBSERVATIONS

Let us consider the effect of Coulomb losses on the spectra of H, He, C, O, and Fe. The maximum Coulomb losses due to interactions with electrons with a typical flare plasma temperature $T \sim 10^6$ K are observed for an ion energy $\frac{E_{\max,e}}{A} \approx 0.5$ MeV/nucleon. At such energies, the mean charges of He, C, and O in solar cosmic rays essentially reach their maximum possible values [17, 23–25]; i.e., $\langle q_{He}\rangle \approx +2$, $\langle q_C\rangle \approx +6$, and $\langle q_O\rangle \approx +8$. Observational data for this energy interval [25, 26] indicate that $\langle q_{Fe}\rangle \approx +11$. It follows from (10) that $\Omega = q^{\frac{5}{3}}A^{-\frac{2}{3}}$ for $S = 5/3$ and $\Omega = q^3A^{-2}$ for $S = 3$.

The table presents Ω for the elements indicated above. We can see that, if the C^{+6} energy spectra shows features produced by Coulomb deceleration (Ω is high) when $S = 5/3$ (for a given plasma number density N), losses of approximately the same intensity should be displayed in the Fe^{+11} spectra, and should be even more distinct in the O^{+8} spectra. On the contrary, when $S = 3$, dips in the C^{+6} and O^{+8} spectra are not accompanied by corresponding features in the Fe^{+11} spectra, since, for the same plasma density, the energy losses for Fe^{+11} are lower by a factor of four to five.

Figure 1 presents numerical solutions obtained for the problem formulation above using a finite difference method with splitting in x and E. For each energy step from E_j to E_{j+1}, we first calculated the f_{j+1} in the absence of Coulomb deceleration via parallel computation of the coefficients for increasing and decreasing indices [16]. Further, we calculated the changes produced in a stationary spectrum in this small energy interval by losses over the relaxation time [see (8), where the energies E_j and E_{j+1} are substituted for E_0 and E, respectively]. In the second stage of the computation, we adopted for N some plasma number density averaged over regions "1" and "2," depending on the shock compression as $N = N_1(r + 1)/2$, with N_1 the plasma density ahead of the shock front. This simplification is associated with our chosen scheme for solving the equations in the presence of Coulomb losses. The

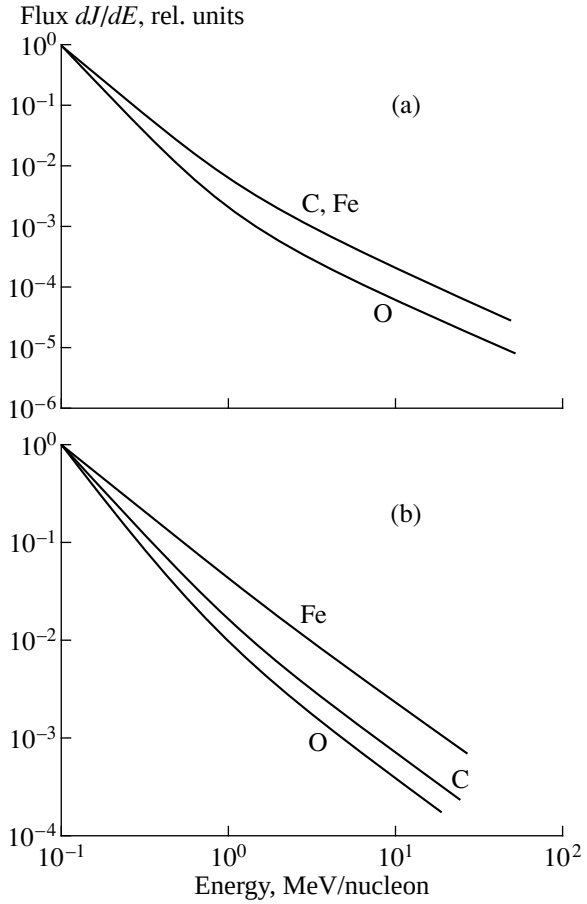

Fig. 1. Energy spectra of the C^{+6}, O^{+8}, and Fe^{+11} ions calculated for $T = 10^6$ K, $N_1 = 5 \times 10^9$ cm^{-3}, and $r = 3$ for two spectral indices for the scattering turbulence: (a) $S = 5/3$ and (b) $S = 3$, taking into account Coulomb losses. For an energy of 0.5 MeV/nucleon and $S = 5/3$, the time scales are $t_a(C^{+6}) = 1.1$ s, $t_a(C^{+6})/t_c(C^{+6}) = 0.43$; $t_a(O^{+8}) = 1.1$ s, $t_a(O^{+8})/t_c(O^{+8}) = 0.57$; $t_a(Fe^{+11}) = 1.5$ s, and $t_a(Fe^{+11})/t_c(Fe^{+11}) = 0.42$. For the same energy and $S = 3$, $t_a(C^{+6}) = 0.7$ s, $t_a(C^{+6})/t_c(C^{+6}) = 0.27$; $t_a(O^{+8}) = 0.7$ s, $t_a(O^{+8})/t_c(O^{+8}) = 0.35$; $t_a(Fe^{+11}) = 0.3$ s, $t_a(Fe^{+11})/t_c(Fe^{+11}) = 0.08$.

plots in Fig. 1 verify our expectations about the dependence of the energy spectra on S. For example, Fig. 1a shows that the C^{+6} and Fe^{+11} spectra virtually coincide for $S = 5/3$, in agreement with the estimates presented in the table.

Thus, the presence of characteristic features in the energy spectra of some elements and their absence in the spectra of others can provide a means to estimate the spectral index of the scattering turbulence of the flare plasma in which the spectra were formed. As an example, let us consider the data for the H, He, C, O, and Fe ions obtained by the *WIND* and *IMP-8* spacecraft [27] for the solar event of October 20, 1995. First, this event is classified as prolonged, with particle acceleration occurring at shock fronts (see Section 1). Second, this is virtually the only event in which the differential intensities of all the elements listed above were measured at energies $E \le 10$ MeV/nucleon, where Coulomb losses can be manifest. These data confirm the presence of a double power law for all the listed elements: $\gamma_1 \approx 2$ at low energies ($E < 0.2$ MeV/nucleon) and $\gamma_2 \approx 3$ at higher energies. This change in the power-law index could be due to the influence of pre-accelerated particles behind the shock front [see (6, 7)]. In addition, there are some features at energies of 0.4–1.5 MeV/nucleon in the C and O spectra. There are no such features in the spectra of the other elements, apparently indicating the insignificance of Coulomb losses for these other elements.

Earlier, the Fe spectrum for the same gradual event with the generation of solar cosmic rays was fit in [16], neglecting energy losses. The best fit was attained for $r = 1.6$ and $\alpha_0 = 4$. The spectra summed over all Fe ions were virtually independent of S, so that this index remained unknown. The estimates presented above for several elements suggest that S was close to three.

Figure 2 shows the observational data and numerical calculations with $S = 3$ for the ions indicated above. The calculations for He, C, and O were performed for the same r and α_0 as those for Fe. Figures 2b and 2c present the C and O spectra for both the maximum charge state and the lower charge states $\langle q_C \rangle = +5.6$ and $\langle q_O \rangle = +7.4$, selected in accordance with the observations of [24, 25]. For both elements, the differences between the spectra obtained for the selected mean charges do not exceed 4%. The typical acceleration time calculated using (8) is about a second for all elements (see the caption of Fig. 2), in agreement with X-ray and gamma-ray data for solar flares.

We took the plasma density and temperature to be $N_1 = 5 \times 10^9$ cm^{-3} and $T = 10^6$ K for the following reasons. If the plasma density were raised to twice this value or the plasma temperature increased to 1.3×10^6 K, the fraction of highly-charged Fe ions would significantly increase, since the ionization rate grows linearly with N_1. However, it follows from (3) that, the greater q, the stronger the Coulomb deceleration; this should give rise to dips in the Fe spectra that were not observed for this event. The plasma density cannot be smaller than 5×10^9 cm^{-3}, since features observed in the C and O spectra due to energy losses would not be expected in this case. The numerical calculations show that these features are not present in the Fe spectra near the maximum Coulomb losses (for the adopted N_1, T, and S). These losses are displayed at higher energies, where the average ion charge becomes significantly higher (see Fig. 2e).

In contrast to other ions, fitting the proton spectrum requires a somewhat larger r value, $r = 1.8$. The reason for this could be the following. When solar particles pass through the interplanetary medium, they can be additionally accelerated by interplanetary shocks. This

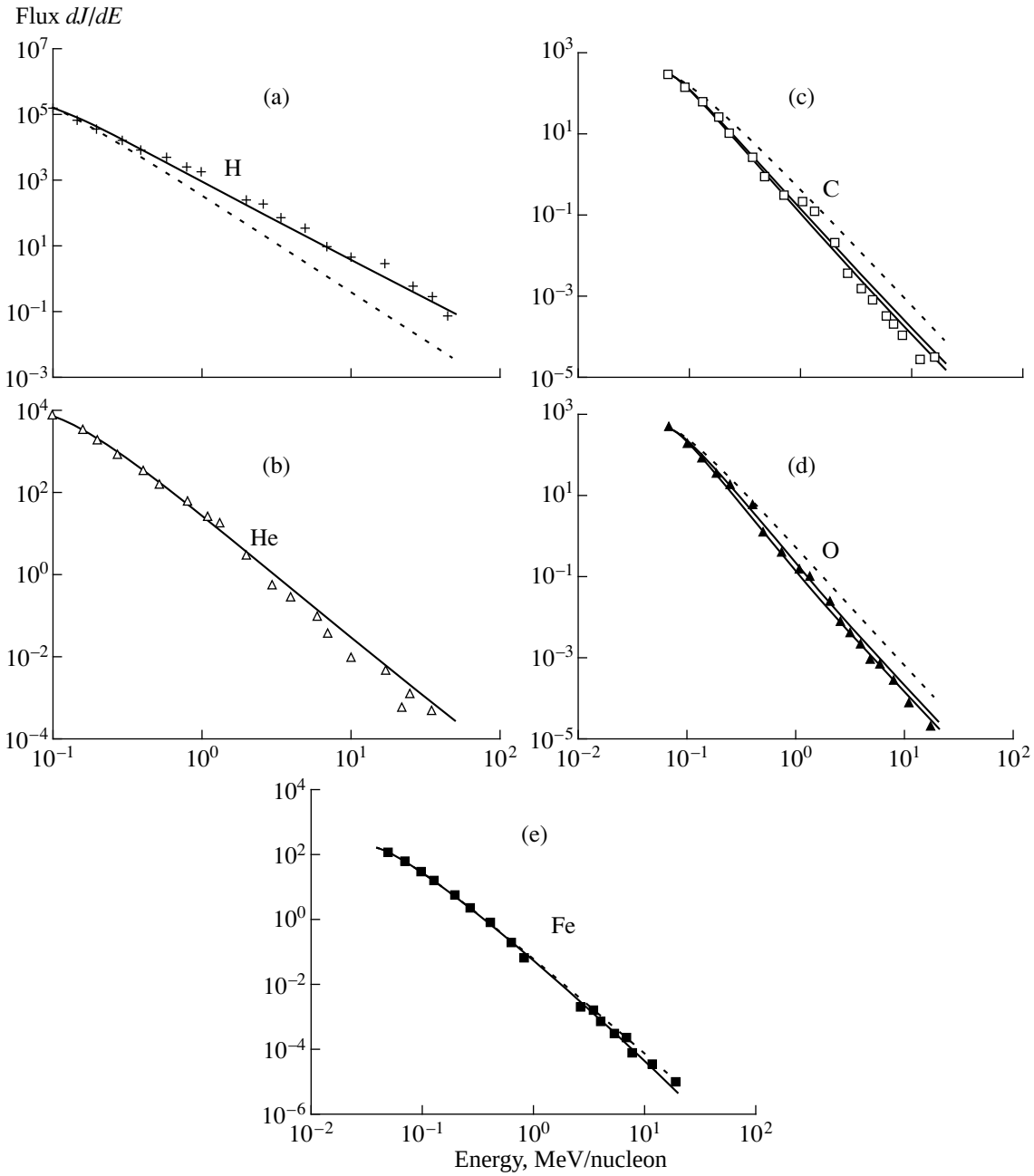

Fig. 2. The energy spectra of heavy ions in particles/(MeV/nucleon cm^2 s) calculated for $S = 3$, $T = 10^6$ K, $u_1 = 4 \times 10^7$ cm/s, $D_0 = 6.4 \times 10^{14}$ cm^2/s, and $N_1 = 5 \times 10^9$ cm^{-3} taking into account Coulomb losses. The shock compression is $r = 1.6$ for all elements except H^+ (see below) and $\alpha_0 = 4$ [see (6)]. The crosses, triangles, and squares show data measured by the *WIND* and *IMP-8* satellites for the prolonged solar event of October 20, 1995 [27]. (a) The spectrum for protons: $t_a(H^+) = 1.1$ s, $t_a(H^+)/t_c(H^+) = 0.11$ (here and below, the time scales are indicated for energy 0.5 MeV/nucleon); the solid and dashed curves correspond to $r = 1.8$ and $r = 1.6$, respectively (see text). (b) The spectrum for helium: $t_a(He^{+2}) = 0.58$ s, $t_a(He^{+2})/t_c(He^{+2}) = 0.06$. (c) The spectrum for carbon: $t_a(C^{+6}) = 0.80$ s, $t_a(C^{+6})/t_c(C^{+6}) = 0.25$; the lower solid curve corresponds to $\langle q_C \rangle = +6$, the upper solid curve to $\langle q_C \rangle = +5.6$, and the dashed curve to neglecting Coulomb losses. (d) The spectrum for oxygen: $t_a(O^{+8}) = 0.80$ s, $t_a(O^{+8})/t_c(O^{+8}) = 0.33$; the lower solid curve corresponds to $\langle q_O \rangle = +8$, the upper solid curve to $\langle q_O \rangle = +7.4$, and the dashed curve to neglecting Coulomb losses. (e) The energy spectrum summed over charges of the iron ions: $t_a(Fe^{+11}) = 0.47$ s, $t_a(Fe^{+11})/t_c(Fe^{+11}) = 0.11$, $t_a(Fe^{+16}) = 0.68$ s, $t_a(Fe^{+16})/t_c(Fe^{+16}) = 0.33$; the dashed curve corresponds to neglecting Coulomb losses.

The parameter Ω for various ions

Ions	Ω	
	$S = 5/3$	$S = 3$
$^{1}H^{+}$	1.0	1.0
$^{4}He^{+2}$	1.3	0.5
$^{12}C^{+6}$	3.8	1.5
$^{16}O^{+8}$	5.0	2.0
$^{56}Fe^{+11}$	3.7	0.4

acceleration will be more efficient for ions with greater q/A ratios [28], since S in the interplanetary space is close to 1.6, according to *Helios-2* data (see, for example, [12]). In fact, the observations of [27] provide evidence for the action of an interplanetary shock on solar particles emitted during the event under consideration, which could possibly explain the harder spectrum for protons with $q/A = 1$. This ratio is higher for protons by a factor of two to four than it is for other elements. Note also that Coulomb losses are not manifest in the proton spectra, in accordance with the estimates for $S = 3$ in the table. Thus, our calculations indicate that the spectral index for the scattering turbulence for the prolonged solar flare of October 20, 1995 [27] was, in all probability, close to three.

Note that the energy spectra of heavy ions at heliocentric distances of about 1 AU have been observationally studied, and found to correspond to the spectra at the source (near the shock front), which remained unchanged three days after the flare [27]. Therefore, we neglect the effects of propagation when comparing the observed spectra and the theoretically calculated stationary spectra. The inevitable limitations of this simplification for impulsive solar events are discussed in [14]. The effect of interplanetary propagation for prolonged events appears to be less significant, probably due to the fact that the bulk of the acceleration takes place at the maximum Mach number, when the shock is near the Sun.

4. DISCUSSION

A similar method for determining S for impulsive events was discussed in [12], where ion spectra were obtained analytically for various energies. However, the energy dependence of the Fe/O ratio (with average charges $\langle q_{Fe}\rangle = +14$ and $\langle q_O\rangle = +7.2$) was studied only for $S = 2$. In that case, the strength of dips in the ion spectra is determined solely by the ratio q^2/A in the expression (3). In [12], S was taken to be close to two based on *Helios-2* data for the slow solar wind (V_{SW} = 327 km/s) at a distance of 0.32 a.u. However, the spectral index detected in this region does not necessarily correspond to the index in the particle acceleration region. Indeed, for explosive, non-stationary processes, the spectral density of the turbulent energy evolves such that $W(k)$ becomes harder [29]. The time scale for this evolution can appreciably exceed the characteristic time for acceleration of solar cosmic rays. Since the acceleration takes place at the initial stage of the flare and turbulence evolution, we can assume that the acceleration has a larger S value in solar events than in interplanetary space. According to our estimates, $S \le 2$ cannot explain the observational data of [27], which indicates virtually no difference between Ω_C, Ω_O, and Ω_{Fe} [see (10) and the table].

An attempt to describe the stochastic and regular acceleration simultaneously using analytical methods and taking Coulomb losses into account was undertaken in [30]. There, particle acceleration by shocks was studied phenomenologically by adding the term $p^{-2}\partial(p^2\dot{p}f)/\partial p$ in the Fokker-Plank equation, where $\dot{p} = p/t_a(p)$ and $t_a(p)$ is determined by (8). However, this model does not yield power-law spectra for the limiting case of a single, regular acceleration event. We model diffusive shock acceleration using the conditions for matching the fluxes and densities at the shock front (see our formulation of the problem), which provides a more self-consistent theory.

We should also discuss the limitations of our approach, and, accordingly, possible difficulties in determining S. Namely, we use a homogeneous plasma model, with the density constant over the entire acceleration period. For example, according to our calculations, the acceleration of oxygen ions from 0.07 MeV/nucleon to 20 MeV/nucleon takes a time $t_a(O^{+8}) = 9.4$ s. Over this time, the shock can move a distance $\sim(4\text{–}20) \times 10^3$ km, which is much smaller than the characteristic length $\sim 10^7$ km for density changes in the quiescent solar corona. The situation might be quite different for perturbed regions, since the shock can sweep up surrounding material when moving in the solar atmosphere, and the plasma can become inhomogeneous near the shock front. This problem is much more difficult than the case of a homogeneous plasma, and requires special study. The only important thing for our calculations is that the ions of all elements be accelerated under the same conditions (for the same event) and go through the same layers of solar material.

It appears that the difference between T_e and T_p, as well as their time evolution during the flare, do not significantly degrade the applicability of our approach. Indeed, the ion deceleration is mainly due to electrons. Therefore, T_p can only affect the spectrum at much lower energies (see above). A change (increase) in T_e can shift the maximum of the Coulomb losses to higher energies, and, consequently, enlarge the corresponding dip in the spectrum. Since the particle acceleration time is much shorter than the time for evolution of the thermal plasma in solar flares, this effect is improbable.

In Eq. (1), we neglect the operator that is second-order in E, describing the energy diffusion or stochastic acceleration of the particles. This is valid only when $t_{reg} \ll t_{stoch}$. As shown in [31], this condition is approximately

satisfied when $1 < S < 2$: the rate of second-order Fermi acceleration ($t_{\rm stoch}^{-1}$) is lower than that of regular acceleration ($t_{\rm reg}^{-1}$) by at least a factor of five. Indeed, when $S < 2$, $t_{\rm reg}/t_{\rm stoch} \sim (V_a/u_1)^2$, and the plasma velocity u_1 near a strong shock is, as a rule, much higher than the Alfvén speed V_a [19]. A self-consistent description of the Alfvén turbulence and particle acceleration near the shock front confirms this conclusion [32]. When $S > 2$, we have $t_{\rm reg}/t_{\rm stoch} \sim (V_a/u_1)^2(V/u_1)^{S-2}$ [19]; that is, the efficiency of stochastic acceleration grows with the energy (V is the particle velocity). For example, our solutions are applicable ($t_{\rm reg}/t_{\rm stoch} \le 0.2$) for the case of maximum ion energy $E = 20$ MeV/nucleon and $u_1 \approx 4 \times 10^7$ cm/s measured in [27] if $V_a \le 2.5 \times 10^6$ cm/s.

For $N_1 \approx 5 \times 10^9$ cm^{-3}, this corresponds to regular magnetic fields $B \le 1$ G in the corona above the active region where the acceleration occurs. For stronger shocks with, for example, $r \approx 3.9$ and $u_1 \approx 2 \times 10^8$ cm/s, we can use the solutions obtained for $B \le 10$ G. Such magnetic fields are quite plausible for acceleration regions situated fairly high in the corona ($h \sim 10^{10}$ cm). Indeed, the numerous data collected in [33] show that there are magnetic fields ~1 to ~10 G in the sources of type-II radio outbursts (which are associated with shocks). Recent data on magnetic reconnection suggest, for example, a magnetic field B from 5 to 20–30 G for the event of February 21, 1992 [34]. We emphasize that our estimate $B \sim 1$–10 G corresponds to an acceleration region situated above a flare arch. A somewhat higher B, $B^2/8\pi \sim Nk_{\rm B}\Delta T$ is possible for the lower part of the arch (ΔT is the increase in the plasma temperature due to magnetic reconnection). For example, a temperature increase from 10^6 to 10^7 K at $N \approx 5 \times 10^9$ cm^{-3} requires $B \sim 13$ G.

We can now estimate the energy density of the scattering turbulence $W_T = \int_{k_{\rm min}}^{\infty} W_0 k^{-S} dk$ using the B values obtained. Expression (2) relates the spatial diffusion coefficient to W_0 and B [19], and yields $W_0 \ge \dfrac{eB^3E_0^{1/2}}{2\pi^2 m_p c D_0}$ for $S = 3$. Our calculations for $u_1 = 4 \times 10^7$ cm/s, $D_{01} = D_{02} \equiv D_0 = 1.6 \times 10^{14}$ cm^2/s, $E_0 = 40$ keV/nucleon, and $B = 1$ G give $W_T \approx 8 \times 10^{-3}B^2/8\pi \approx 5 \times 10^{-4}Nk_{\rm B}T$, which allows use of a quasi-linear approximation for the solar flare plasma [20] when deriving (2). The analogous estimate for $u_1 = 2 \times 10^8$ cm/s, $D_{01} = D_{02} = D_0 = 3 \times 10^{15}$ cm^2/s (t_a is constant), and $B = 10$ G yields a similar energy density $W_T \approx 5 \times 10^{-3}B^2/8\pi \approx 1.7 \times 10^{-4}Nk_{\rm B}T$. For the same $B = 10$ G and $N = 5 \times 10^9$ cm^{-3}, we obtain $k_{\rm max} \sim \omega_{Bp}/V_a = 5 \times 10^{-3}$ cm^{-1}, which corresponds to energies $E_{\rm min} < E_0$ ($E_{\rm min} = 2m_p(\pi\omega_{Bp}/k_{\rm max})^2$). The value of $k_{\rm min}$ was already indicated in Section 2. Thus, the plasma parameters obtained above provide reasonable estimates for the spectral bounds of turbulence that can accelerate particles from $E_0 = 40$ keV/nucleon to the maximum observed energies (tens of MeV per nucleon).

5. CONCLUSIONS

Our work shows that the presence of Coulomb features in the energy spectra of some accelerated ions and their absence in the spectra of other ions can provide evidence for some particular spectral index for the scattering turbulence, and can also yield estimates of the plasma density and temperature in the acceleration region. We can obtain more accurate estimates of the admissible plasma densities and temperatures providing agreement between numerical calculations and observations by taking into account charge transitions during the acceleration and Coulomb losses simultaneously (compare with the case of neglecting Coulomb losses).

For example, for the prolonged solar event of October 20, 1995, for which the energy spectra of H, He, C, O, and Fe ions were measured, our analysis yields $S = 3$, $T = 10^6$ K, $N = 5 \times 10^9$ cm^{-3}, and $B \sim 1$ G. For the time scales chosen for the acceleration of heavy ions (seconds), the scatter in these parameters is small. If the real time scales for the acceleration of solar cosmic rays in this event are longer (shorter) by a factor of a few, we must decrease (increase) the plasma number density accordingly.

ACKNOWLEDGMENTS

This work was supported by the Center for Basic Natural Sciences of the St. Petersburg State University of the Ministry of General and Professional Education of the Russian Federation (project no. 97-3.1-3), and by the Russian Foundation for Basic Research (project nos. 99-02-18398 and 00-02-17031).

REFERENCES

1. H. V. Cane, R. E. McGuire, and T. T. von Rosenvinge, Astrophys. J. **301**, 448 (1986).
2. M. A. Lee and J. M. Ryan, Astrophys. J. **303**, 829 (1986).
3. S. V. Bulanov and P. V. Sasorov, Astron. Zh. **52**, 763 (1975) [Sov. Astron. **19**, 464 (1975)].
4. Yu. E. Litvinenko and B. V. Somov, Sol. Phys. **158**, 317 (1995).
5. M. Temerin and I. Roth, Astrophys. J. Lett. **391**, L105 (1992).
6. G. E. Kocharov, Itogi Nauki Tekh., Ser. Astron. **32**, 43 (1987).
7. D. V. Reames, J. P. Meyer, and T. T. von Rosenvinge, Astrophys. J., Suppl. Ser. **90**, 649 (1994).
8. S. W. Kahler, N. R. Sheeley, R. A. Howard, *et al.*, J. Geophys. Res. **89**, 9683 (1984).
9. I. N. Toptygin, *Cosmic Rays in Interplanetary Magnetic Fields* (Nauka, Moscow, 1983; Reidel, Dordrecht, 1985).

10. E. G. Berezhko, V. K. Elshin, G. F. Krymskiĭ, and S. N. Petukhov, *Cosmic-Ray Generation by Shock Waves* [in Russian] (Nauka, Novosibirsk, 1988).
11. S. V. Bulanov and V. A. Dogel', Pis'ma Astron. Zh. **5**, 521 (1979) [Sov. Astron. Lett. **5**, 278 (1979)].
12. J. Steinacker, U. Jaekel, and R. Schlickeiser, Astrophys. J. **415**, 342 (1993).
13. Yu. E. Litvinenko, AIP Conf. Proc. **374**, 498 (1996).
14. V. M. Ostryakov, Yu. Yu. Kartavykh, and G. A. Koval'tsov, Pis'ma Astron. Zh. **26** (2), 152 (2000) (in press) [Astron. Lett. **26**, 122 (2000)].
15. I. G. Kurganov and V. M. Ostryakov, Pis'ma Astron. Zh. **17**, 177 (1991) [Sov. Astron. Lett. **17**, 77 (1991)].
16. V. M. Ostryakov and M. F. Stovpyuk, Pis'ma Astron. Zh. **25**, 935 (1999) [Astron. Lett. **25**, 819 (1999)].
17. A. M. Luhn and D. Hovestadt, Astrophys. J. **317**, 852 (1987).
18. K. Hasselmann and G. Wibberenz, Z. Geophys. **34**, 353 (1968).
19. R. Schlickeiser, Astrophys. J. **336**, 264 (1989).
20. J. Steinacker and J. A. Miller, Astrophys. J. **393**, 764 (1992).
21. A. A. Korchak, Sol. Phys. **66**, 149 (1980).
22. R. Schlickeiser, A. Campeanu, and I. Lerche, Astron. Astrophys. **276**, 614 (1993).
23. M. Arnaud and J. Raymond, Astrophys. J. **398**, 394 (1992).
24. G. M. Mason, J. E. Mazur, M. D. Looper, and R. A. Mewaldt, Astrophys. J. **452**, 901 (1995).
25. M. Oetliker, B. Klecker, D. Hovestadt, *et al.*, Astrophys. J. **477**, 495 (1997).
26. E. Möbius and M. Popecki, http://www.scl.caltech.edu/ACE/ACENews_curr.html (1998).
27. D. V. Reames, L. M. Barbier, T. T. von Rosenvinge, *et al.*, Astrophys. J. **483**, 515 (1997).
28. H. V. Cane, D. V. Reames, and T. T. von Rosenvinge, Astrophys. J. **373**, 675 (1991).
29. J. A. Miller, P. J. Cargill, A. G. Emslie, *et al.*, J. Geophys. Res. **102**, 14631 (1997).
30. R. Schlickeiser and J. Steinacker, Sol. Phys. **122**, 29 (1989).
31. R. Vainio and R. Schlickeiser, Astron. Astrophys. **331**, 793 (1998).
32. R. Vainio and R. Schlickeiser, Astron. Astrophys. **343**, 303 (1999).
33. A. Kruger, *Introduction to Solar Radio Astronomy and Radio Physics* (Reidel, Dordrecht, 1979; Mir, Moscow, 1984).
34. S. Tsuneta, Astrophys. J. **456**, 840 (1996).

Translated by V. Badin

Astronomy Reports, Vol. 44, No. 12, 2000, pp. 841–847. Translated from Astronomicheskiĭ Zhurnal, Vol. 77, No. 12, 2000, pp. 953–960.

Short-Period Variations in the Proper Motions of Sunspots from SOHO (MDI) Observations

L. V. Didkovskiĭ

Crimean Astrophysical Observatory, p/o Nauchnyĭ, Crimea, 334413 Ukraine

Received December 2, 1999

Abstract—Short-period (1–60 min) variations in the coordinates of the centers of gravity of isolated sunspots are analyzed. The sunspot coordinated were determined using two sets of observational data—magnetograms and intensities—obtained by SOHO (MDI) on December 6, 1998, from 01:00 to 21:57 UT with temporal resolution 60 s and spatial resolution 0.6″/pixel. A slow drift in the sunspot coordinates was removed using a low-frequency filter with a 61-min integration window. The guiding errors (RMS ~ 0.014″) were determined by analyzing correlated motions in pairs of sunspots, and were removed from the time series before determining the sunspot proper motions. Based on the calculated power spectra for the sunspot proper motions, two period intervals containing appreciable power were identified. One coincides with the well-known 5-min acoustic solar oscillations. The concentration of power in this interval is greater for the coordinate variations derived the magnetograms than those derived from the intensities; the harmonic amplitude for some peaks reaches ~±30 km. The other spectral interval corresponds to periods exceeding 30 min. Overall, the rms short-period variations in the sunspot proper motions are 9.9 ± 2.2 and 16.7 ± 7.6 km ($0.014'' \pm 0.003''$ and $0.024'' \pm 0.010''$) for the magnetogram and intensity data, respectively. © *2000 MAIK "Nauka/Interperiodica".*

1. INTRODUCTION

After the discovery of sunspot proper motions [1], they became an important basis and then instrument for studying the motions of material in subphotospheric layers, as well as interactions of this motion with magnetic fields. Initially, a slow meridional drift of sunspots was revealed [1–4], with an estimated velocity of several tens of cm/s. As instruments and methods for solar observations improved, it became possible to study more rapid displacements of sunspots against the background of their rotational motion. It was later established that the character of sunspot proper motions depends on the dynamics both of the sunspot (active region) itself and of the interaction of large-scale plasma motions with solar magnetic fields. In particular, proper motions depend on the structure of the active region, its location on the disk, the age of the sunspots, the phase of the solar activity cycle, and other manifestations of solar activity. After Gnevysheva [5] concluded that the similar trajectories of closely-spaced sunspots reflected their common drift, associated with large-scale vortex plasma flows under the photosphere, Stepanov and Klyakotko [6] attempted to estimate the velocity and spatial structure of these flows.

A series of studies of latitudinal variations in the rotational velocity [7–9], meridional motions of sunspots [10] and small photospheric magnetic structures [11], and proper motions in the network of bright points and magnetic fluxes [12, 13] have demonstrated differences in the motions of sunspots with respect to the motions of other observable structures. This testifies to a complex interrelation between these proper motions and processes occurring beneath the photosphere. Variations in sunspot proper motions with periods less than one day [14] can provide important information about the structure and dynamics of subphotospheric layers [15]. However investigation of relatively small and rapid variations in sunspot proper motions requires high-quality observations with very good spatial and temporal resolution, such as that provided by MDI [16] installed on the SOHO space telescope.

The aim of the present paper is to investigate rapid variations (with periods of several minutes) in the proper motions of sunspots derived from MDI measurements of the magnetic field and intensity.

2. OBSERVATIONAL DATA

The observational data are images of part of the solar disk near its center, 1024×500 pixels in size, with a spatial resolution of 0.605″/pixel. We analyzed images obtained on December 6, 1998 from measurements of the intensity and magnetic field with temporal resolution 60 s for two time intervals of duration ≈6 and 5 h (356 and 286 images, respectively). The observations were carried out in the Ni I 6768 Å line; the intensity measurements were conducted in the continuum near this line. Figure 1 shows the positions of the sunspots SP1, SP2, and SP3 at the starting times for each of the two intervals. To determine the contribution to variations in the sunspot coordinates from guiding errors, we considered the sunspots in pairs, assuming that the main contribution of guiding errors to sunspot motions

1063-7729/00/4412-0841$20.00 © 2000 MAIK "Nauka/Interperiodica"

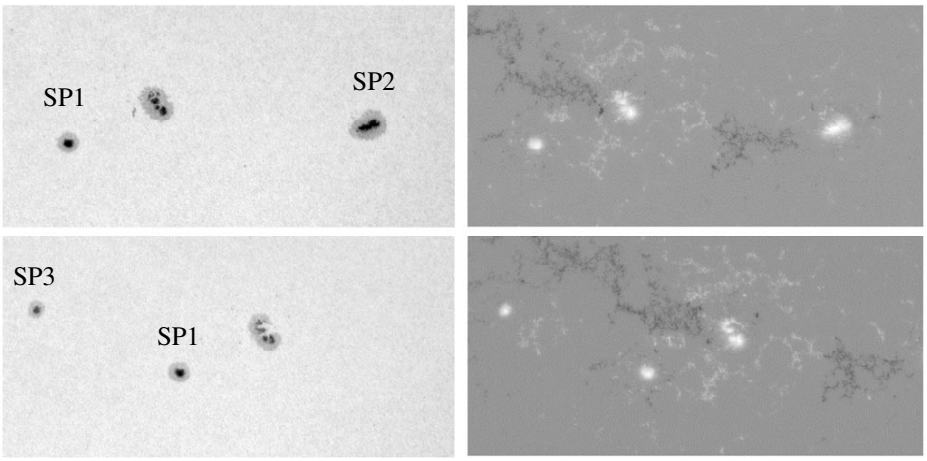

Fig. 1. Images of the intensity (left) and magnetic field (right) obtained by SOHO–MDI at the beginning of the two analyzed time intervals—01:00 UT (top) and 17:12 UT (bottom)—on December 6, 1998. Two pairs of sunspots used in the analysis—(SP1–SP2) and (SP3–SP1)—are marked.

should be manifest as simultaneous correlated changes in the coordinates of different sunspots.

3. PRELIMINARY ANALYSIS

Portions of the solar images where sunspots were shifted by the photospheric rotation were identified and set apart for further analysis. To decrease the influence of rapid signal fluctuations (inherent in the pixels around sunspots and their penumbrae) on the calculated values, the coordinates of the sunspot centers of gravity X_0 and Y_0 were determined using the most stable parts of the sunspots, in their umbrae. The intensity and magnetic field umbrae were bounded by the values S_I = 2000 and S_M = 500, respectively. These values can be changed to reflect the motion of the sunspot as a whole, including the penumbra, but this does not appreciably influence the results. We calculated the center-of-gravity coordinates X_0 and Y_0 for pixels $S_{kn}(t)$ whose signal $P_{kn}(t) = S_I - S_{kn}(t)$ (intensity) or $P_{kn}(t) = S_{kn}(t) - S_M$ (magnetic field) was positive:

$$X_0(t) = \frac{\sum_{k,n} P_{kn}k}{\sum_{k,n} P_{kn}}, \quad Y_0(t) = \frac{\sum_{k,n} P_{kn}n}{\sum_{k,n} P_{kn}}. \qquad (1)$$

Preliminary analysis of the time series $X_0(t)$, $Y_0(t)$, and $P_{kn}(t)$ showed that, in some cases, there was a correlation ($|R| > 0.5$) between variations in the coordinates and the average intensity or magnetic-field signal in a specified sunspot zone. These correlations are due to redistribution of the signal within the analyzed zone of the sunspot umbra, and can produce spurious signals in the coordinate variations, which are associated neither with guiding errors nor with proper motion of the sunspot. To elucidate the importance of these variations on the spectral composition of the proper motions, we used another model for the sunspot umbra in which the distribution of the signal was flat (which does not correspond to the actual observed signal distribution), with a constant level of S_M for pixels whose magnetogram signal exceeded S_M or whose intensity was less than S_I (i.e., in the sunspot umbra, where the $P_{kn}(t)$ were positive). The signals for other pixels, not satisfying the condition $P_{kn}(t) > 0$, were assumed to be zero. In this case, the center-of-gravity coordinates were calculated using the formulas

$$X'_0(t) = \frac{\sum_{k,n} S_M k}{\sum_{k,n} S_M}, \quad Y'_0(t) = \frac{\sum_{k,n} S_M n}{\sum_{k,n} S_M}. \qquad (2)$$

The variations of the sunspot coordinates were also calculated in a coordinate system fixed to the Sun, in which X_0 and Y_0 were transformed into longitude and latitude. As an example, Fig. 2 presents the time variations in the latitude of the center of SP1 in both magnetic field and intensity, along with the corresponding changes of the average signals used to calculate the coordinates. These average signals were calculated as

$$\sum_{k,n} P_{kn}/(kn). \qquad (3)$$

A preliminary analysis of the correlation coefficients for the coordinates of sunspots SP1 and SP2, SP3 and SP1 showed that (1) there is some correlation between the coordinate variations derived from the intensity and magnetic-field signals for the same sunspot ($0.15 < R < 0.87$); (2) the relations between variations of the coordinates and signals have a wider interval of correlation coefficients ($-0.69 < R < 0.71$); and

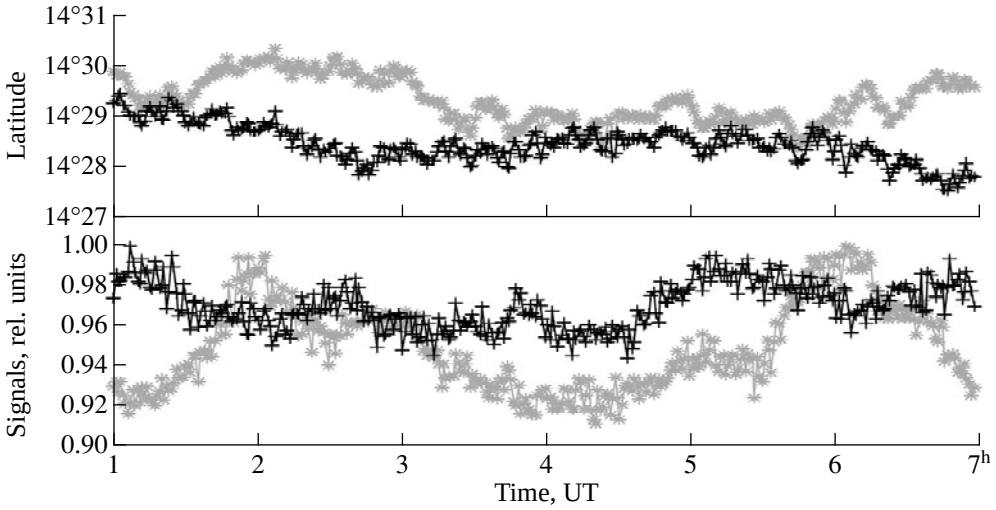

Fig. 2. Time variations in the latitude coordinates for the intensity (stars) and magnetograms (crosses) (top panel; 0.04° were added to the magnetogram coordinates for ease in comparing the correlated and uncorrelated variations) and changes of the average (over the sunspot umbra) signals (bottom panel).

(3) simultaneous, sometimes correlated, variations in the coordinates of different sunspots are observed ($-0.67 < R < 0.83$).

This last feature could have the following origins. First, there could be random correlated motions. Next, simultaneous, coherent motions of different sunspots could be the result of large-scale plasma flows. Finally, they could be due to guiding errors. From our point of view, the first two reasons could make only a small contribution, since the analysis was conducted for two quite long time intervals (6 and 5 h). In addition, the distance between the sunspots was rather large (for example, about 25° in longitude for SP1 and SP2) to expect an appreciable contribution from large-scale subphotospheric flows. Therefore, we believe that the main reason for the simultaneous, correlated variations in the coordinates of different sunspots within the analyzed time intervals is guiding errors.

4. GUIDING ERRORS

Guiding errors can affect the determination of sunspot proper motions, usually introducing correlated changes in the calculated sunspot coordinates. The present paper deals with short-period variations in the sunspot proper motions. After excluding low-frequency coordinate drifts from the time series (for example with a moving average), the residuals have fairly small rms deviations from the average values (about 0.05 pixel, i.e., 0.03″). Therefore, we can assume that the guiding errors are of the same order or less. Indeed, MDI has its own fine-guiding system, which reduces the jitter of images to a level of about 0.02″ for averaging over a minute [17]. The drift of the solar-image center for longer observing intervals can be as large as 1″. In his analysis of a time series of Doppler velocities with a duration of more than one hour, Duvall [18] found that the rms variations in the image motions were about 0.014″ [18].

Our method for determining the guiding errors is based on analysis of simultaneous and correlated variations in the X_0 and Y_0 coordinates for a chosen pair of well-separated, isolated sunspots using time series derived from the intensity and magnetic-field measurements. Low-frequency variations in the coordinates were filtered out via subtraction of a moving average with an integration window of 61 min.

Figure 3a shows the X_0 residuals for the intensity $C(I_1)$ and magnetic field $C(M_1)$ for SP1, as well as the average $A_1 = (C(I_1) + C(M_1))/2$; the same values are shown for SP2 in Fig. 3b. The average signals A, B', and $G = (A + B')/2$, where B' was calculated by fitting the A and B curves to each other, are presented in Fig. 3c. The procedure for fitting the average curves A and B is based on determining the $x_{\min}$ that minimizes the square of the norm $\|A - B'\|^2$, where $B' = x_{\min}B$:

$$x_{\min} = \frac{A^T B + B^T A}{2B^T B}. \quad (4)$$

As we can see in Fig. 3, the average curves A, B', and G are well correlated with each other ($R = 0.64$). In the case of the Y_0 residuals, $R = 0.75$.

The same procedure for another time interval and sunspots SP3 and SP1, which are closer to each other than SP1 and SP2, revealed a lower degree of correlation ($R = 0.54$ and 0.59 for X_0 and Y_0, respectively). This confirms our suggestion that the main contribution to the mutual correlation of the coordinates of sunspot pairs is produced by guiding errors G.

The rms guiding errors—0.015″ and 0.013″ for the first and second observation intervals—are approximately equal. The power spectra of the guiding errors

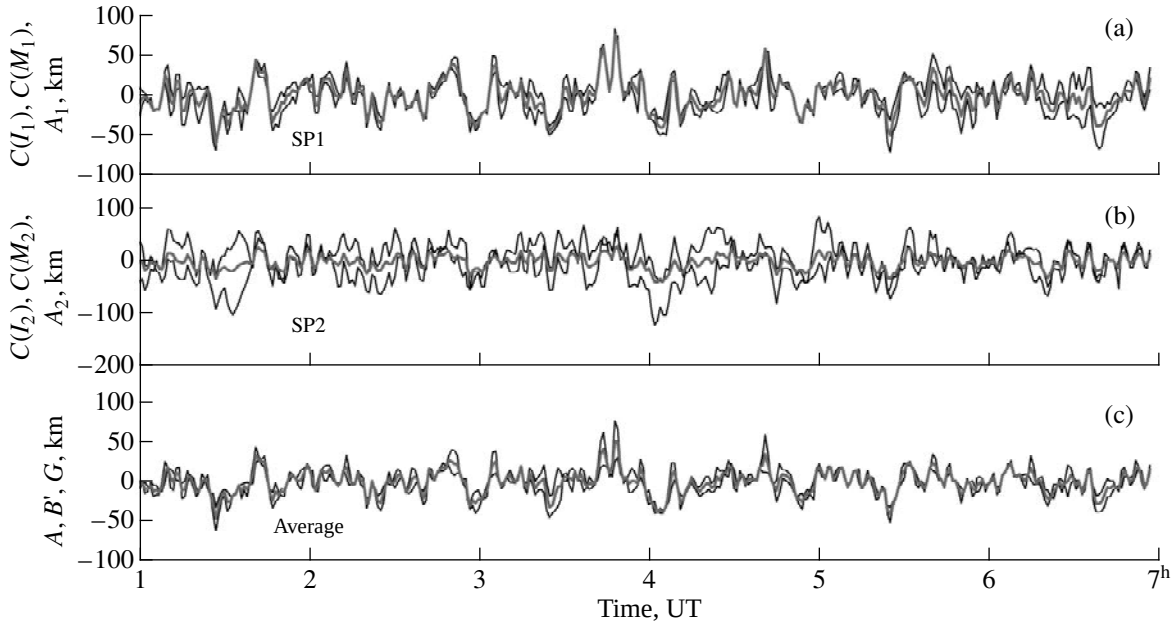

Fig. 3. X_0 residuals (after subtraction of moving average) for the magnetic field and intensity and their average over sunspots (a) SP1 and (b) SP2; (c) the average curves for SP1 and SP2 after minimizing the square of the norm along with their average curve G; i.e., the guiding error.

are characterized by the same (or very similar) fundamental frequencies for the coordinate variations for both sunspot models. This confirms our earlier suggestion that the correlation of the sunspot coordinate variations is associated primarily with image shifts, rather than with variations of the solar signals measured in the sunspot umbrae.

5. SUNSPOT PROPER MOTIONS

We determined the proper motions of sunspots SP1, SP2, and SP3 for each of the two sunspot models (1) and (2) by subtracting the guiding errors from the coordinate residuals (after subtracting the moving average). Figure 4 shows vector fields of the proper motions in polar coordinates for sunspots SP1 (upper diagrams) and SP2 (middle and lower diagrams). The left and right columns correspond to the variations derived using the intensity and magnetic-field images, respectively. The middle and lower diagrams refer to SP2 sunspot models (1) and (2), respectively.

Some of the calculated power spectra for the X_0 and Y_0 variations in the coordinates of the sunspot proper motions are shown in Fig. 5. The thin and thick curves refer to variations in the intensity and magnetic field, respectively. Figure 5 shows that the amplitudes of the coordinate variations at frequencies 0.2–1.5 MHz calculated using the intensity images are usually larger than those calculated using the magnetic-field images. In contrast, the power peaks derived from the magnetic field in the well-known 5-min band (i.e., near 3.3 MHz) exceed those derived from the intensity, and have a harmonic amplitude reaching ±30 km. The frequencies of the main peaks for the intensity and magnetic field are in good agreement with each other.

6. DISCUSSION

We have used intensity and magnetic-field images obtained by the SOHO space observatory to analyze the proper motions of sunspots in two time intervals with a total duration of about 11 h. A slow drift of the coordinates of the center of gravity of the sunspots was filtered out by subtracting a moving average with a 61-min integration window, and more rapid variations in the proper motions were determined after removing guiding errors.

These guiding errors were defined by considering simultaneous, correlated variations in the coordinates of different sunspots. A special analysis demonstrated that these variations are due primarily to shifts of the images. The correlation coefficients for variations in the coordinates of well-separated, isolated sunspots in two time intervals with a total duration of about 11 h were 0.54–0.75. The contribution of variations of the solar signals to the coordinate variations was studied by comparing the coordinates calculated for two sunspot models; namely, with the real distribution of the signals inside the analyzed part of the sunspot (umbra) and with a fixed (flat) distribution. Use of the sunspot umbrae, which is the most stable part of an active region in time, yielded similar guiding errors (in terms of the character of the motion and the power of the oscillations) for both sunspot models. The derived rms

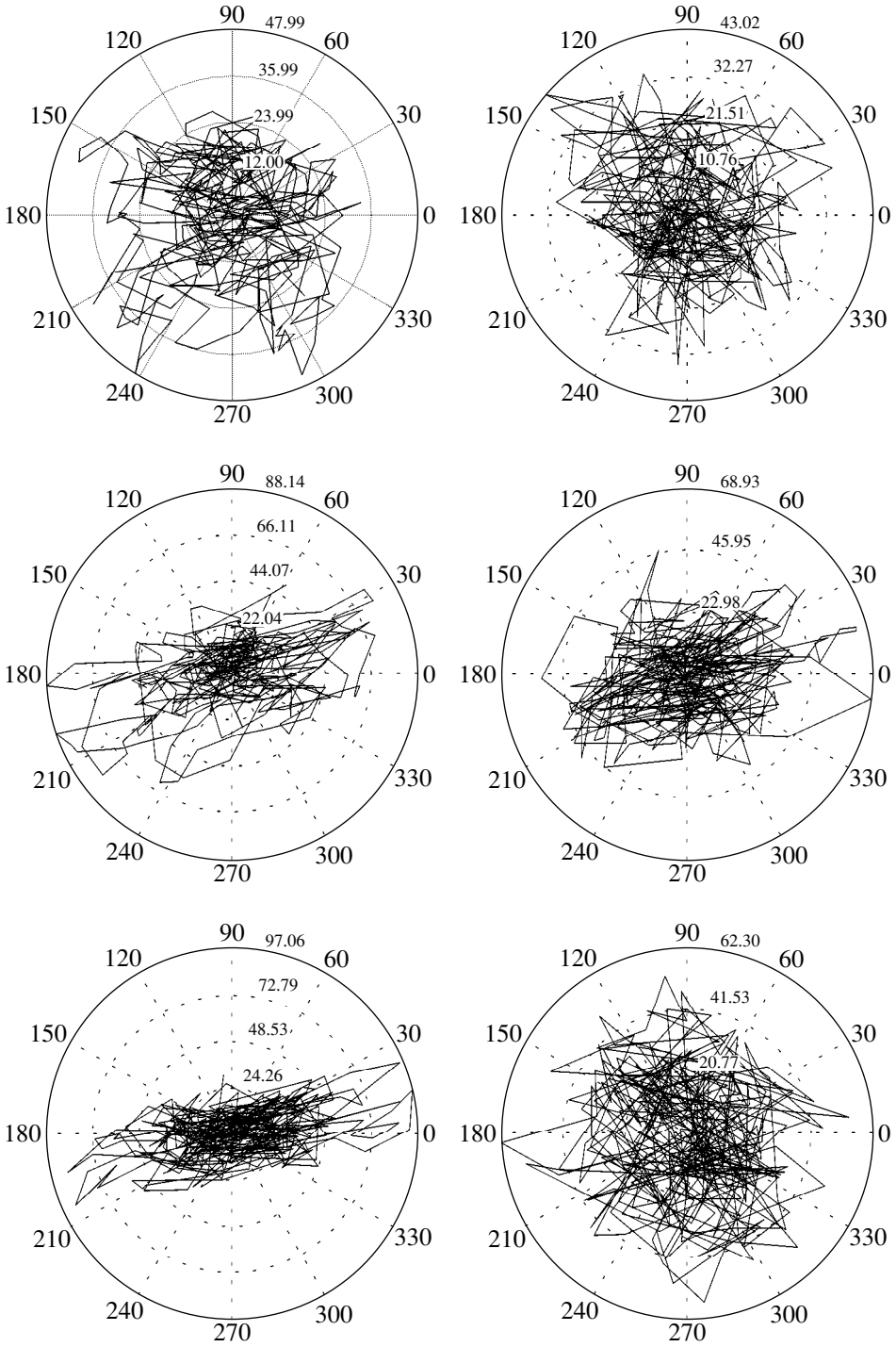

Fig. 4. Proper motions of sunspot SP1 (upper diagrams) and sunspot SP2 described by model (1) (middle diagrams) and model (2) (lower diagrams). The left and right columns correspond to intensity and magnetic field. The radial scales are given in kilometers, and the angular scales in degrees.

guiding errors (about 0.014″) nearly coincide with those calculated with another method [19], using the radial-velocity images for another observing date. The distribution of the image-displacement vectors (i.e., the guiding errors) has no preferred direction, and is symmetric in the image plane, as distinct from the sunspot proper-motion vectors (Fig. 4). The guiding-error power spectra indicate a considerably lower concentration of

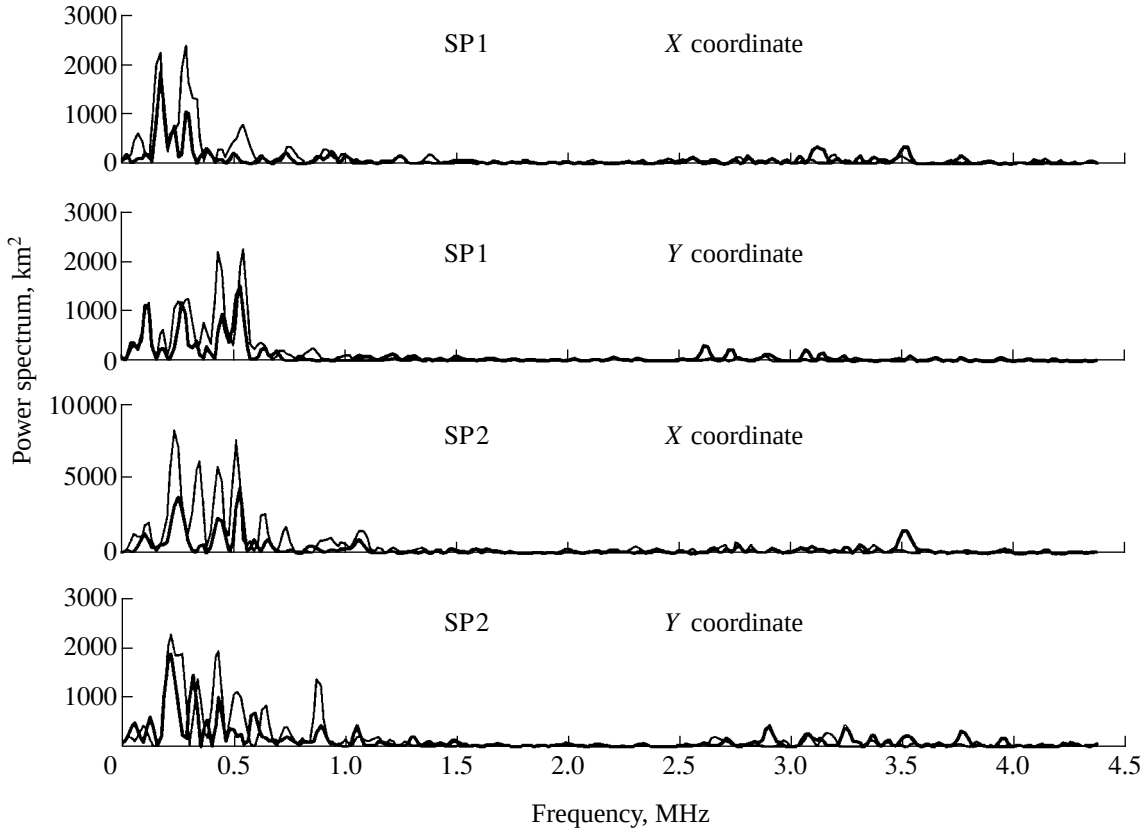

Fig. 5. Power spectra of the proper motions for SP1 and SP2 derived from the intensity (thin curves) and magnetic field (thick curves) for the vertical (*Y*) and horizontal (*X*) motions.

power in the 5-min oscillations than at longer periods, apparently due to the structure of the SOHO/MDI guiding system.

The sunspot proper motions derived from the intensity and magnetic field are different. This is true not only of the preferred directions of the sunspot motions, which are more clearly concentrated along the sunspot symmetry axis in the case of the intensity coordinates, but also of the amplitudes of the motions. This could be associated with the different levels in the photosphere where the continuum and Ni I line are formed. The amplitudes of the variations in the proper motions derived from the intensity are approximately a factor of 1.7 larger than those derived from the magnetic field.

The power spectra of sunspot proper motions measured using the magnetograms show a concentration of power near the 5-min oscillations, whereas there is considerably less power at this period for the intensity proper motions. On the other hand, the intensity and magnetic-field power peaks at longer periods (15–60 min) are in good agreement. Note that the low-frequency filter used decreases the amplitudes of peaks at long periods. The character of the power distribution in the proper-motion spectra indicates a sharp increase in the power at frequencies below 0.6 MHz (i.e., with periods over 28 min).

The rms amplitudes of the proper-motion variations for periods from several minutes to several hours are 9.9 ± 2.2 and 16.7 ± 7.6 km for the magnetic-field and intensity images, respectively. The presence of short-period variations in the sunspot motions, especially in the 5-min band, could be associated with the conversion of energy of absorbed acoustic oscillations and waves to energy of sunspot proper motion.

REFERENCES

1. R. S. Carrington, *Observation of Spots on the Sun* (1863), p. 222.
2. H. F. Newall, Mon. Not. R. Astron. Soc. **85**, 553 (1925).
3. F. J. Stratton, Mon. Not. R. Astron. Soc. **69**, 659 (1909).
4. H. H. Turner, Mon. Not. R. Astron. Soc. **68**, 98 (1907).
5. R. S. Gnevysheva, Astron. Zh. **18**, 26 (1941).
6. V. E. Stepanov and M. A. Klyakotko, Izv. Krym. Astrofiz. Obs. **16**, 80 (1956).
7. P. H. Scherrer, J. M. Wilcox, and L. Svalgaard, Astrophys. J. **241**, 811 (1980).

8. H. W. Newton and M. L. Nunn, Mon. Not. R. Astron. Soc. **111**, 413 (1951).
9. R. Muller and Th. Roudier, Sol. Phys. **152**, 131 (1994).
10. G. Lustig and H. Wohl, Astron. Astrophys. **249**, 528 (1991).
11. R. W. Komm, R. F. Howard, and J. W. Harvey, Sol. Phys. **147**, 207 (1993).
12. R. Muller, Th. Roudier, J. Vigneau, and H. Auffret, Astron. Astrophys. **283**, 232 (1994).
13. V. Bumba, M. Klvana, and B. Kalman, Astron. Astrophys., Suppl. Ser. **118**, 35 (1996).
14. B. Anwar, L. W. Acton, H. S. Hudson, *et al.*, Sol. Phys. **147**, 287 (1993).
15. F. Mazzuconi, C. Coveri, and G. Godoli, Sol. Phys. **125**, 269 (1990).
16. P. H. Scherrer, R. S. Bogart, R. I. Bush, *et al.*, Sol. Phys. **162**, 129 (1995).
17. P. H. Scherrer, private communication, 1999.
18. T. L. Duvall, private communication, 1999.

Translated by Yu. Dumin